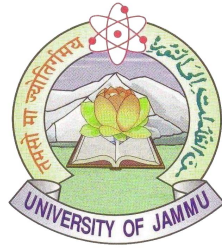


Particle Ratios and Transverse Momentum Spectra at RHIC Energies



A
THESIS

SUBMITTED TO THE UNIVERSITY OF JAMMU
FOR
THE AWARD OF THE DEGREE OF

DOCTOR OF PHILOSOPHY
IN
PHYSICS

by
Shikshit Gupta

Post Graduate Department of Physics & Electronics
University of Jammu, Jammu Tawi
J&K 180006 (INDIA)
(April 2015)

Dedicated
to
my Mentor
Dr. M. P. Singh
for his great sacrifices
and
LOVE

DECLARATION

I, **Shikshit Gupta**, declare that the work reported in this thesis entitled “Particle Ratios and Transverse Momentum Spectra at RHIC Energies” has entirely been done by me under the supervision of Prof. Anju Bhasin and Prof. Sanjeev Singh Sambyal in the Department of Physics and Electronics, University of Jammu, Jammu. No part of this work has been submitted in part or full for the award of the degree in any other University.

Dated: **10th April, 2015**



Shikshit Gupta

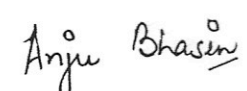
POST GRADUATE DEPARTMENT OF PHYSICS & ELECTRONICS
UNIVERSITY OF JAMMU, JAMMU TAWI - 180006

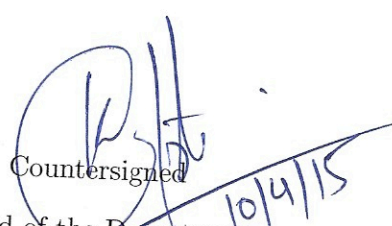
CERTIFICATE

It is certified that **Mr. Shikshit Gupta**, worked under our supervision and the work is worthy of consideration for the award of Ph.D Degree in Physics. It is further certified that:

1. the thesis embodies the work of the candidate himself;
2. the candidate worked under our supervision for the period required under statutes;
3. the candidate has put in the required attendance during that period in the Department;
4. the conduct of the candidate remained satisfactory during that period;
5. the candidate has fulfilled the statutory conditions as laid down in Section 18 of statutes governing degree of Doctor of Philosophy issued vide notification no. 4 dated 04-03-2013.


(Prof. Sanjeev Singh Sambyal)
Supervisor


(Prof. Anju Bhasin)
Supervisor


Countersigned
Head of the Department
Head of the Deptt
Physics & Electronics
University of Jammu
10/4/15

List of Publications/Preprints

- [1] **Effect of event selection on jetlike correlation measurement in d+Au collisions at $\sqrt{s_{NN}} = 200$ GeV.**
L. Adamczyk, **Shikshit Gupta**, ... et al., (for the STAR Collaboration).
Phys. Lett. B **743**, 333-339 (2015).
- [2] **Charged-to-neutral correlation at forward rapidity in Au+Au collisions at $\sqrt{s_{NN}} = 200$ GeV.**
L. Adamczyk, **Shikshit Gupta**, ... et al., (for the STAR Collaboration).
Phys. Rev. C **91**, 034905 (2015).
- [3] **$\Lambda\Lambda$ Correlation Function in Au+Au collisions at $\sqrt{s_{NN}} = 200$ GeV.**
L. Adamczyk, **Shikshit Gupta**, ... et al., (for the STAR Collaboration).
Phys. Rev. Lett. **114**, 022301 (2015).
- [4] **Measurement of longitudinal spin asymmetries for weak boson production in polarized proton-proton collisions at RHIC.**
L. Adamczyk, **Shikshit Gupta**, ... et al., (for the STAR Collaboration).
Phys. Rev. Lett. **113**, 072301 (2014).
- [5] **Observation of D^0 Meson Nuclear Modifications in Au+Au Collisions at $\sqrt{s_{NN}} = 200$ GeV.**
L. Adamczyk, **Shikshit Gupta**, ... et al., (for the STAR Collaboration).
Phys. Rev. Lett. **113**, 142301 (2014).
- [6] **Beam-energy dependence of charge separation along the magnetic field in Au+Au collisions at RHIC.**
L. Adamczyk, **Shikshit Gupta**, ... et al., (for the STAR Collaboration).
Phys. Rev. Lett. **113**, 052302 (2014).

- [7] **Dielectron azimuthal anisotropy at mid-rapidity in Au+Au collisions at $\sqrt{s_{NN}} = 200$ GeV.**
L. Adamczyk, **Shikshit Gupta**, ... et al., (for the STAR Collaboration).
Phys. Rev. C **90**, 064904 (2014).
- [8] **Beam energy dependence of moments of the net-charge multiplicity distributions in Au+Au collisions at RHIC.**
L. Adamczyk, **Shikshit Gupta**, ... et al., (for the STAR Collaboration).
Phys. Rev. Lett. **113**, 092301 (2014).
- [9] **Beam-Energy Dependence of the Directed Flow of Protons, Antiprotons, and Pions in Au+Au Collisions.**
L. Adamczyk, **Shikshit Gupta**, ... et al., (for the STAR Collaboration).
Phys. Rev. Lett. **112**, 162301 (2014).
- [10] **Dielectron Mass Spectra from Au+Au Collisions at $\sqrt{s_{NN}} = 200$ GeV.**
L. Adamczyk, **Shikshit Gupta**, ... et al., (for the STAR Collaboration).
Phys. Rev. Lett. **113**, 022301 (2014).
- [11] **Suppression of Υ production in d+Au and Au+Au collisions at $\sqrt{s_{NN}} = 200$ GeV.**
L. Adamczyk **Shikshit Gupta**, ... et al., (for the STAR Collaboration).
Phys. Lett. B **735**, 127-137 (2014).
- [12] **J/ψ polarization in p+p collisions at $\sqrt{s_{NN}} = 200$ GeV in STAR.**
L. Adamczyk, **Shikshit Gupta**, ... et al., (for the STAR Collaboration).
Phys. Lett. B **739**, 180-188 (2014).
- [13] **J/ψ production at low p_T in Au+Au and Cu+Cu collisions at $\sqrt{s_{NN}} = 200$ GeV with the STAR detector.**

- L. Adamczyk, **Shikshit Gupta**, ... et al., (for the STAR Collaboration).
Phys. Rev. C **90**, 024906 (2014).
- [14] **Energy Dependence of Moments of Net-proton Multiplicity Distributions at RHIC.**
L. Adamczyk, **Shikshit Gupta**, ... et al., (for the STAR Collaboration).
Phys. Rev. Lett. **112**, 032302 (2014).
- [15] **Identified particle production in $p + p$ collisions in $\sqrt{s} = 62.4$ GeV at STAR.**
Shikshit Gupta (for the STAR Collaboration).
Quark Matter Proceeding, Darmstadt, Germany (2014)
- [16] **Neutral pion cross section and spin asymmetries at intermediate pseudorapidity in polarized proton collisions at $\sqrt{s} = 200$ GeV.**
L. Adamczyk, **Shikshit Gupta**, ... et al., (for the STAR Collaboration).
Phys. Rev. D **89**, 012001 (2014).
- [17] **Measurement of charge multiplicity asymmetry correlations in high-energy nucleus-nucleus collisions at $\sqrt{s_{NN}} = 200$ GeV.**
L. Adamczyk, **Shikshit Gupta**, ... et al., (for the STAR Collaboration).
Phys. Rev. C **89**, 044908 (2014).
- [18] **Jet-Hadron Correlations in $\sqrt{s_{NN}} = 200$ GeV p+p and Central Au+Au Collisions.**
L. Adamczyk, **Shikshit Gupta**, ... et al., (for the STAR Collaboration).
Phys. Rev. Lett. **112**, 122301 (2014).
- [19] **Fluctuations of charge separation perpendicular to the event plane and local parity violation in $\sqrt{s_{NN}} = 200$ GeV Au+Au collisions at**

the BNL Relativistic Heavy Ion Collider.

L. Adamczyk, **Shikshit Gupta**, ... et al., (for the STAR Collaboration).
Phys. Rev. C **88**, 064911 (2013).

- [20] **Freeze-out dynamics via charged kaon femtoscopy in $\sqrt{s_{NN}} = 200$ GeV central Au+Au collisions.**

L. Adamczyk, **Shikshit Gupta**, ... et al., (for the STAR Collaboration).
Phys. Rev. C **88**, 034906 (2013).

- [21] **System-size dependence of transverse momentum correlations at $\sqrt{s_{NN}} = 62.4$ and 200 GeV at the BNL Relativistic Heavy Ion Collider.**

L. Adamczyk, **Shikshit Gupta**, ... et al., (for the STAR Collaboration).
Phys. Rev. C **87**, 064902 (2013).

- [22] **Elliptic flow of identified hadrons in Au+Au collisions at $\sqrt{s_{NN}} = 7.7$ -62.4 GeV.**

L. Adamczyk, **Shikshit Gupta**, ... et al., (for the STAR Collaboration).
Phys. Rev. C **88**, 014902 (2013).

- [23] **Observation of an Energy-Dependent Difference in Elliptic Flow between Particles and Antiparticles in Relativistic Heavy Ion Collisions.**

L. Adamczyk, **Shikshit Gupta**, ... et al., (for the STAR Collaboration).
Phys. Rev. Lett. **110**, 142301 (2013).

- [24] **Third Harmonic Flow of Charged Particles in Au+Au Collisions at $\sqrt{s_{NN}} = 200$ GeV.**

L. Adamczyk, **Shikshit Gupta**, ... et al., (for the STAR Collaboration).
Phys. Rev. C **88**, 014904 (2013).

- [25] **Measurement of J/ψ Azimuthal Anisotropy in Au+Au Collisions at**

$\sqrt{s_{NN}} = 200$ GeV.

L. Adamczyk, **Shikshit Gupta**, ... et al., (for the STAR Collaboration).
Phys. Rev. Lett. **111**, 052301 (2013).

[26] **Experimental studies of di-jets in Au + Au collisions using angular correlations with respect to back-to-back leading hadrons.**

L. Adamczyk, **Shikshit Gupta**, ... et al., (for the STAR Collaboration).
Phys. Rev. C **87**, 044903 (2013).

[27] **J/ ψ production at high transverse momenta in p+p and Au+Au collisions at $\sqrt{s_{NN}} = 200$ GeV.**

L. Adamczyk, **Shikshit Gupta**, ... et al., (for the STAR Collaboration).
Phys. Lett. B **722**, 55-62 (2013).

[28] **Identified charged particle spectra in $p + p$ collisions in $\sqrt{s} = 62.4$ GeV at RHIC.**

Shikshit Gupta (for the STAR Collaboration).
Proceedings of the DAE Symposium on Nucl. Phys. Vol. 58, 780 (2013).

[29] **Inclusive charged hadron elliptic flow in Au + Au collisions at $\sqrt{s_{NN}} = 7.7 - 39$ GeV.**

L. Adamczyk, **Shikshit Gupta**, ... et al., (for the STAR Collaboration).
Phys. Rev. C **86**, 054908 (2012).

[30] **Single Spin Asymmetry A_N in Polarized Proton-Proton Elastic Scattering at $\sqrt{s} = 200$ GeV.**

L. Adamczyk, **Shikshit Gupta**, ... et al., (for the STAR Collaboration).
Phys. Lett. B **719**, 62-69 (2013).

[31] **Transverse Single-Spin Asymmetry and Cross-Section for π^0 and η**

Mesons at Large Feynman- x in Polarized p+p Collisions at $\sqrt{s} = 200$ GeV.

L. Adamczyk, **Shikshit Gupta**, ... et al., (for the STAR Collaboration).
Phys. Rev. D **86**, 051101 (2012).

[32] **Longitudinal and transverse spin asymmetries for inclusive jet production at mid-rapidity in polarized p+p collisions at $\sqrt{s} = 200$ GeV.**

L. Adamczyk, **Shikshit Gupta**, ... et al., (for the STAR Collaboration).
Phys. Rev. D **86**, 032006 (2012).

[33] **Measurements of D^0 and D Production in p+p Collisions at $\sqrt{s} = 200$ GeV.**

L. Adamczyk, **Shikshit Gupta**, ... et al., (for the STAR Collaboration).
Phys. Rev. D **86**, 072013 (2012).

[34] **Di-electron spectrum at mid-rapidity in p+p collisions at $\sqrt{s} = 200$ GeV.**

L. Adamczyk, **Shikshit Gupta**, ... et al., (for the STAR Collaboration).
Phys. Rev. C **86**, 024906 (2012).

[35] **Directed Flow of Identified Particles in Au + Au Collisions at $\sqrt{s_{NN}} = 200$ GeV at RHIC .**

L. Adamczyk, **Shikshit Gupta**, ... et al., (for the STAR Collaboration).
Phys. Rev. Lett. **108**, 202301 (2012).

[36] **Measurement of the $W \rightarrow e\nu$ and $Z/\gamma \rightarrow e^+e^-$ Production Cross Sections at Mid-rapidity in Proton-Proton Collisions at $\sqrt{s} = 500$ GeV.**

L. Adamczyk, **Shikshit Gupta**, ... et al., (for the STAR Collaboration).
Phys. Rev. D **85**, 092010 (2012).

- [37] **Energy and system-size dependence of two- and four-particle v_2 measurements in heavy-ion collisions at RHIC and their implications on flow fluctuations and nonflow.**

G. Agakishiev (Dubna, JINR), **Shikshit Gupta**, ... et al., (for the STAR Collaboration).

Phys. Rev. C **86**, 014904 (2012).

- [38] **System size and energy dependence of near-side di-hadron correlations.**

G. Agakishiev (Dubna, JINR), **Shikshit Gupta**, ... et al., (for the STAR Collaboration).

Phys. Rev. C **85**, 014903 (2012).

- [39] **Identified hadron compositions in p+p and Au+Au collisions at high transverse momenta at $\sqrt{s_{NN}} = 200$ GeV.**

G. Agakishiev (Dubna, JINR), **Shikshit Gupta**, ... et al., (for the STAR Collaboration).

Phys. Rev. Lett. **108**, 072302 (2012).

- [40] **Directed and elliptic flow of charged particles in Cu+Cu collisions at $\sqrt{s_{NN}} = 22.4$ GeV.**

G. Agakishiev (Dubna, JINR) **Shikshit Gupta**, ... et al., (for the STAR Collaboration).

Phys. Rev. C **85**, 014901 (2012).

- [41] **Anomalous centrality evolution of two-particle angular correlations from Au-Au collisions at $\sqrt{s_{NN}} = 62$ and 200 GeV.**

G. Agakishiev (Dubna, JINR) **Shikshit Gupta**, ... et al., (for the STAR Collaboration).

Phys. Rev. C **86**, 064902 (2012).

- [42] **ρ^0 Photoproduction in AuAu Collisions at $\sqrt{s_{NN}} = 62.4$ GeV with STAR.**

G. Agakishiev (Dubna, JINR) **Shikshit Gupta**, ... et al., (for the STAR Collaboration).

Phys. Rev. C **85**, 014910 (2012).

- [43] **Strangeness Enhancement in Cu+Cu and Au+Au Collisions at $\sqrt{s_{NN}} = 200$ GeV.**

G. Agakishiev (Dubna, JINR), **Shikshit Gupta**, ... et al., (for the STAR Collaboration).

Phys. Rev. Lett. **108**, 072301 (2012).

- [44] **Charged Particle Ratios for $p+p$ Collisions in $\sqrt{s}= 62.4$ GeV at RHIC.**

Shikshit Gupta (for the STAR Collaboration).

Quark Matter Proceeding, Annecy, France (2011).

- [45] **Evolution of the differential transverse momentum correlation function with centrality in Au+Au collisions at $\sqrt{s_{NN}} = 200$ GeV.**

H. Agakishiev (Dubna, JINR), **Shikshit Gupta**, ... et al., (for the STAR Collaboration).

Phys. Lett. B **704**, 467-473 (2011).

ACKNOWLEDGEMENTS

At the onset, I owe a debt of gratitude to my esteemed supervisors Prof. Anju Bhasin and Prof. Sanjeev Singh Sambyal, for keeping faith over my limited abilities and providing me the unique opportunity to learn a lot about this field of High Energy Physics. I am greatly indebted to them, not only for their guidance and support but also for giving me total freedom both academically and socially during this period. I owe lot to my supervisor Prof. Anju Bhasin (former HOD and P.I., ALICE U, O & U Project) for her supervision, constant encouragement and support to me in all respects. I am also grateful to her for providing me the much needed fellowship throughout the period of my Ph.D work. I would also like to express my sincere gratitude to my supervisor Prof. Sanjeev Singh Sambyal, for the amiable and decent manner in which he tendered his cooperation.

My regardful thanks are due to Prof. Vivek Gupta, Head, Department of Physics & Electronics, University of Jammu, for providing me the necessary infrastructure, help, support and other facilities required for carrying out my research work.

I would like to take this opportunity to express my sincere and heartfelt thanks to Dr. Bedangadas Mohanty, Associate Professor, National Institute of Science Education and Research, Bhubaneswar, for his timely help in the completion of my analysis work. Had he not allowed me to work in his group, this thesis work would never be possible. I also express my sincere gratitude to Dr. Lokesh Kumar, Assistant Professor, Panjab University, Chandigarh, for his valuable guidance, timely help and for assisting me in the analysis work from the beginning and helped me see it through to its completion.

With deep regards I would also like to express my gratitude to Er. Anik Gupta, Scientist 'G', Jammu University, for his kind support, encouragement, good wishes and for always willing to extended every possible help I asked for. I am also thankful

to other members of HEP Group, Prof. P. V. K. S. Baba, Er. Sanjay Mahajan, Dr. Saroj K. Nayak and Dr. Ramni Gupta for their help and good wishes.

It gives me great pleasure to thank all the people associated with the STAR experiment, especially, Dr. Yuri Fisyak, Dr. Gene Van Buren, Mr. Jason Webb, Dr. Xianglei, Mr. Kefeng Xin, and Dr. Jerome Lauret for their help in simulation and embedding studies. I am also thankful to the STAR team leaders, Dr. Nu Xu, former Spokesperson and Dr. Zhangbu Xu, present Spokesperson for providing me a great opportunity to work at Brookhaven Lab, USA and helping me in excelling in this field of science. I owe a thanks to all the physics working group members and conveners from Light Flavor Spectra for their useful inputs and healthy discussions regarding my analysis. I am also grateful to STAR Collaborators from the different institutes in India for providing me an opportunity to work with them.

My sincere thanks are also due to the Indian PMD group leaders and theoretician, Dr. Y. P. Viyogi, Dr. Subhasis Chattopadhyay, Dr. Tapan Kumar Nayak, Prof. Pradip Sahoo and Prof. Sourendu Gupta for their useful suggestions regarding my research work.

I wish to thank all the members of the RCF at BNL, VECC grid, NERSC center at LBNL and HEP grid, Jammu University for providing the computing resources and help.

I also offer my sincere gratitude to Dr. Renu Bala, CSIR SRA (Pool Officer), Jammu University and Dr. Sunil Manohar Dogra (Post Doctoral Fellow, Sao Paulo Institute, Brazil) for their help and encouragement during my research period. My special thanks go to my senior Dr. Ranbir Singh, Scientific Officer, NISER, Bhubaneswar, for introducing me to this field of experimental HEP and for his immense support and encouragement during my research period. Special thanks are reserved for Mr. Inayat Rasool Bhat for teaching me several concepts of physics and

for many fruitful physics discussions.

I would also like to thank my seniors Dr. Satish Sharma, Dr. Chaman Lal, and Dr. Ramesh Sachdeva for their help, good wishes and kind support towards me.

I am also grateful to Dr. Md. Nasim, Dr. Subhash Singha, Mr. Rihan Haque, Mr. Srikantha, Dr. Mriganka, Dr. Nihar Sahoo and Dr. S.K. Prasad, for helping me in my analysis.

I sincerely thank all the members of technical and non-technical staff of HEP Group, especially Mr. Vivek Chalotra for his help and support. With sincere regards, I would also like to thank, Mr. Tarsem, Mr. Ravinder Sharma, Mr. Ravi, Mr. Surinder, Mr. Sat Paul for their affection, kind support, service they rendered to me and remaining always willing to help me whenever I approached them. I am also grateful to all other technical and non-technical employees in the department for their help and good wishes especially Mr. Gaja Singh for providing food and bedding during night stays in the department.

Many thanks to my colleagues from other institutes of India and abroad, Sabita, Bhanu, Arindam, Prakhar, Vipul, Kishora, Debadeepti, Prabhat, Gregory, Geraldo and Prashanth Shanmugathan for their help and good wishes

I would like to express my loving regards and thanks to all HEP labmates – Mukesh (Muki), for his help and support. Rohni (Gillu) for her cooperation, help and for always standing by me. I would also like to appreciate: Jagjeet, Ankita, Sonia, Monika, Mandeep, Sakshi, Ajay and Sandeep for sharing such a good time with me and also for their keen affection, support, good wishes and help for me. Thanks are also due to Sahil, Iftar, Rakesh, Bhanu and Lakshmi for their good wishes and regards. I also reserve a words of thanks for our new research colleagues viz. Abhinav and Mona.

I gratefully acknowledge the Department of Science & Technology and Department of Atomic Energy, Govt. of India for providing me the financial assistance during my

research period.

In true spirits, words could never convey my deep sense of gratitude towards my “Teacher” Dr. M.P. Singh, for his love and sacrificing nature to one and all. I owe all the achievements of my life to him. I am also thankful to all the members of the SHAOLIN Family for their love , encouragement and never lasting support for me. It’s a great honor and true pleasure to be part of this family.

With profound love and deep regards I would like to express my sincere gratitude for my parents for their patience, unconditional support, love, care and blessings. I am also thankful to my brothers Rahul & Arun and our new family member Ruchi bhabi for their best wishes and encouragement. Let me express my heart felt thanks to all the dedicated people for their contribution in the field of Science & Physics and also to all the great people of the world who ever contributed for the sake of humanity, for making our lives better than before despite facing lots of hardships themselves.

Thank God for everything, for I have whatsoever nothing to make this happen to me.

Shikshit

Shikshit Gupta

Contents

1	Introduction to high energy physics	1
1.1	Heavy-ion physics	1
1.2	Quantum Chromodynamics (QCD)	4
1.3	QGP and the QCD phase diagram	10
1.4	Ultra-relativistic heavy ion collisions	16
1.4.1	Space-time evolution	16
1.4.2	Predicted signatures of QGP	19
1.5	Organization of the thesis	19
2	Elementary collisions, particle spectra and ratios	23
2.1	Introduction	23
2.2	Proton-proton collisions	23
2.3	Modelling of $p + p$ collisions	26
2.3.1	Classification of $p + p$ interaction	26
2.3.2	Monte Carlo event generators	32
2.3.2.1	PYTHIA	35
2.3.2.2	PHOJET	36
2.3.2.3	HIJING	38
2.4	Phenomenological Models	38
2.4.1	Thermal model	40

2.4.2	Non-extensive thermodynamic model	40
2.4.3	Collective behavior in $p + p$ collisions	41
2.5	Particle yields and ratios	42
2.5.1	Significance of particle spectra and ratios	43
2.5.1.1	Some Experimental Results	46
3	Experimental Facility	51
3.1	Introduction	51
3.2	RHIC Complex	51
3.3	STAR experiment	57
3.3.1	Trigger detectors	60
3.3.2	Time Projection Chamber	62
3.3.2.1	Physics Objectives:	63
3.3.2.2	Design & geometry:	63
3.3.2.3	Basic Mechanism :	67
3.3.2.4	Performance of TPC :	68
3.3.3	Time Of Flight	72
3.3.4	Barrel Electromagnetic Calorimeter	75
3.3.5	Endcap Electromagnetic Calorimeter	76
3.3.6	STAR's DAQ	77
3.3.7	Recent Upgrade	79
3.4	Event Reconstruction in the TPC	81
3.4.1	Cluster/Hit Reconstruction	82
3.4.2	Coordinate transformation and distortion corrections	83
3.4.3	Track Reconstruction	85
3.4.3.1	Helix Parameterization	86
3.4.4	Vertex reconstruction	88

3.5	Particle Identification by dE/dx	91
4	Analysis Techniques	95
4.1	Introduction	95
4.2	Strategy of data analysis	96
4.3	Data-set information	98
4.4	Event selection	98
4.5	Track selection	99
4.6	Extraction of raw particle yields for various particles	101
4.7	Systematic uncertainties	108
5	Corrections to the particle spectra	115
5.1	Introduction	115
5.2	Simulation and embedding	115
5.3	Corrections	119
5.3.1	Trigger and Vertex efficiency	119
5.3.2	Tracking efficiency	123
5.3.3	Energy loss correction	124
5.3.4	Pion background correction	126
5.3.5	Proton background correction	128
6	Transverse momentum spectra and particle ratios	131
6.1	Introduction	131
6.2	Transverse Momentum Spectra	132
6.2.1	Comparison with the models	134
6.2.2	Comparison with the PHENIX experiment	135
6.3	Particle ratios and comparison with models	138
6.4	Particle ratios and comparison with PHENIX	141

6.5	Particle yield per unit rapidity	142
6.6	Mean transverse momentum $\langle p_T \rangle$	147
7	Summary and Conclusions	149
7.1	Summary	149
7.2	Conclusions	150
	APPENDICES	153
A	Relativistic Kinematics	153
A.1	Mandelstam Variables	153
A.2	Rapidity	154
B	Lund string fragmentation model	156
B.1	Meson production	156
B.2	Baryon production	157
B.3	Multiparton interactions	158
C	Fitting Spectra	160
C.1	Bose-Einstein function	161
C.2	Exponential in p_T	161
C.3	Exponential in m_T	162
C.4	Boltzmann function	162
C.5	Power law	162
C.6	Tsallis (Levy) function	163
D	Tables	164

List of Figures

1.1	<i>The info-graphic of a given Standard Model</i>	2
1.2	<i>The allowed interactions as per the Standard Model</i>	4
1.3	<i>Polarization of a dielectric medium around a positive electric charge, and the effective value of the charge as a function of distance and of momentum transfer.</i>	5
1.4	<i>The effective value of color charge as a function of probing distance and of momentum transfer.</i>	7
1.5	<i>The quark-quark potential calculated from lQCD. In the plot $r_0 = 0.5$ fm and $V(r_0) = 0$ [6].</i>	9
1.6	<i>Stages in the formation of a quark-gluon plasma and subsequent hadron emission: (a) two heavy nuclei collide at high energies (b) interact via the gluon field; (c) the very high energy-density produced causes the quarks and gluons to deconfine and form a plasma that can radiate photons and lepton pairs; (d) finally as the plasma cools, hadrons condense and are emitted [9].</i>	11
1.7	<i>Schematic of QCD phase diagram. The solid lines show the phase boundaries for the indicated phases. The solid circle depicts the critical point where sharp distinction between the hadronic gas and QGP phases cease to exist. Possible trajectories for systems created in the QGP phase at different accelerator facilities are also shown.</i>	14

1.8	<i>Schematic view of two colliding nuclei in the geometrical model. . . .</i>	15
1.9	<i>Top panel : Overview of the space-time evolution in ultra-relativistic nuclear collision. Bottom panel : Schematic of various stages of heavy ion collision as a function of time and longitudinal coordinate (the collision axis)</i>	17
2.1	<i>An incoming parton might branch ($q \rightarrow qg$) before the collision in an initial state shower. Similarly a parton branching after the collision is referred to as a final-state shower. After the collision, the color string span between the outgoing quarks and gluons. These fragments into colorless hadrons, which can be unstable and further decay [18]. . . .</i>	25
2.2	<i>Graphical Representation of the most common event types in $p + p$ collisions. The left side pictures are the graphical representations of the processes and right side pictures depicts their azimuthal distributions as a function of pseudorapidity in the final state of scattering.</i>	28
2.3	<i>Graphical Representation of the Non-Diffractive (ND) process in $p + p$ collisions. The left side represents the graphical picture of the process and right side depict the azimuthal distribution as a function of pseudorapidity in the final state of scattering.</i>	30
2.4	<i>Schematic view of the non-diffractive $p + p$ interaction.</i>	31
2.5	<i>Thermal model fit to the particle productions made by the STAR experiment [31].</i>	39
2.6	<i>(Color online) Transverse momentum spectra of positive hadrons from $p + p$ collisions at $\sqrt{s} = 900$ GeV. The error shown is a systematic plus statistical added in quadrature. The solid curves represent the Lévy function used to extract the meaningful parameters [51].</i>	47

2.7	(Color online) Transverse momentum spectra of π^\pm from Au + Au collisions at $\sqrt{s_{NN}} = 62.4$ GeV. The π^-/π^+ ratio is also shown in the right panel. The errors shown are statistical, and the shaded bands reflect the systematic errors [52].	48
2.8	(Color online) Upper panels: Centrality and p_T dependance of R_{CP} for $\pi^+ + \pi^-$ and $p + \bar{p}$ for Au + Au at $\sqrt{s_{NN}} = 62.4$ GeV. Lower panels: R_{AA} for $\pi^+ + \pi^-$ at 62.4 GeV (0-10%) and 200 GeV (0-20%) compared to three model predictions. The errors shown are statistical, and the shaded bands reflect the systematic errors [52].	48
2.9	(a) K^+/π^+ and K^-/π^- ratios as a function of the collision energy in $p + p$ and central heavy ion collisions. (b) K^+/K^- ratio as a function of the collision energy in the central heavy ion collisions. The curves going through the heavy ion K^-/π^- and K^+/K^- data are phenomenological fits. The curves going through the heavy ion K^+/π^+ data are the product of the fit curves [55].	49
3.1	The Relativistic Heavy Ion Collider Complex.	52
3.2	RHIC integrated luminosity for heavy ion and proton-proton collision.	53
3.3	Perspective view of the STAR detector, with a cutaway for viewing inner detector systems [61].	58
3.4	(Color online) A schematic view of a nucleus-nucleus collisions and STAR trigger systems.	61
3.5	Cutaway view of the TPC along with some other sub-detectors.	62
3.6	Time Projection Chamber.	64
3.7	Arrangement of Read-out Chamber in Time Projection Chamber.	66
3.8	A sector of the TPC anode plane indicating the inner and outer sub-sectors and their respective padrows.	66

3.9	<i>Ionization Energy Loss method.</i>	71
3.10	<i>Schematics of the TOF system: Barrel TOF trays and upVPD's upon the beam pipe on the east and west sides .</i>	74
3.11	<i>Particle identification using TOF.</i>	75
3.12	<i>Schematic of STAR's BEMC. The BEMC towers are annotated and their projectivity to the interaction diamond is illustrated by the tilting of towers. Shown in green are energy deposited by tracks coming from the vertex .</i>	77
3.13	<i>(Left) Side view of the BEMC module showing the 20 lead layers and 21 layers of scintillators. Also shown are the two layers of Shower Maximum Detector (BSMD) sitting at a depth of $\sim 5X_0$ from the front face at $\eta=0$. (Right) A schematic illustration of an electromagnetic shower at the BSMD wire layers which provide a two-dimensional image of the shower.</i>	78
3.14	<i>Partial schematic view of the STAR system including the MTD and the HFT [77].</i>	80
3.15	<i>a) Projection of a helix onto the transverse (x-y) plane. b) Projection onto the bend (s-z) plane [85].</i>	87
3.16	<i>a) Side-wise view and, b) End-wise view of the p+p event. The red star symbol represents the vertex position determined by the software [86].</i>	89
3.17	<i>a) Vertex distribution along longitudinal and, b) transverse direction in p + p event [86].</i>	90
3.18	<i>Identification of the particles by Ionization Energy Loss.</i>	92
4.1	<i>Reference multiplicity of charged particles.</i>	97
4.2	<i>Quality assurance plots displaying the event information.</i>	100
4.3	<i>Transverse momentum distribution of charged particles in p+p collisions.</i>	101

4.4	<i>Quality assurance plots displaying the track information.</i>	102
4.5	<i>Identification of the particles by Ionization Energy Loss.</i>	103
4.6	<i>Multi-gaussian fit for the Z_{π^+} distribution for a specific p_T bin.</i>	105
4.7	<i>Multi-gaussian fits for Z_{π^+} for 6-different p_T bins.</i>	106
4.8	<i>Multi-gaussian fits for Z_{π^-} for 6-different p_T bins.</i>	107
4.9	<i>Multi-gaussian fits for Z_{K^+} for 6-different p_T bins.</i>	109
4.10	<i>Multi-gaussian fits for Z_{K^-} for 6-different p_T bins.</i>	110
4.11	<i>Multi-gaussian fits for Z_p for 6-different p_T bins.</i>	112
4.12	<i>Multi-gaussian fits for $Z_{\bar{p}}$ for 6-different p_T bins.</i>	113
5.1	<i>Comparison of DCA and Nhits distributions for different eta and p_T bins of embedding and real data.</i>	120
5.2	<i>Flowchart showing different corrections done in this analysis.</i>	121
5.3	<i>Vertex Efficiency as a function of number of primary tracks.</i>	123
5.4	<i>Efficiency \times Acceptance for π^\pm, K^\pm, p and \bar{p}.</i>	125
5.5	<i>Energy loss effect for π^\pm as a function of p_T in $p + p$ event.</i>	126
5.6	<i>Energy loss effect for K^\pm, p and \bar{p} as a function of p_T in $p + p$ events.</i>	127
5.7	<i>Pion background fraction from weak decays (K_s^0 & Λ), μ^\pm contamination and total background as a function of p_T in $p + p$ events.</i>	128
5.8	<i>Global DCA distributions of the protons and antiprotons alongwith the background contamination in the $p + p$ events for two different p_T bins.</i>	129
6.1	<i>Identified transverse momentum spectra for π^\pm, K^\pm, p and \bar{p} (positive particles: filled symbols in left panel and negative particles: open symbols in right panel) measured at mid-rapidity ($y < 0.1$) for $\sqrt{s} = 62.4$ GeV in $p + p$ collisions. Errors are both statistical and systematic added in quadrature. The size of the error bars are smaller than the symbol size.</i>	132

6.2	<i>Identified transverse momentum spectra for π^\pm (positive particles: are shown in the left panel and negative particles: are shown in the right panel) measured at mid-rapidity ($y < 0.1$) for $\sqrt{s} = 62.4$ GeV in $p+p$ collisions. Statistical errors are shown with bars whereas the systematic errors are shown with the shaded band.</i>	133
6.3	<i>Identified transverse momentum spectra for K^\pm (positive particles: are shown in the left panel and negative particles: are shown in the right panel) measured at mid-rapidity ($y < 0.1$) at $\sqrt{s} = 62.4$ GeV in $p+p$ collisions. Statistical errors are shown with bars whereas the systematic errors are shown with the shaded band.</i>	134
6.4	<i>Identified transverse momentum spectra for p and \bar{p} (positive particles: are shown in the left panel and negative particles: are shown in the right panel) measured at mid-rapidity ($y < 0.1$) for $\sqrt{s} = 62.4$ GeV in $p + p$ collisions. Statistical errors are shown with bars whereas the systematic errors are shown with the shaded band.</i>	135
6.5	<i>Identified transverse momentum spectra for π^\pm (positive particles: are shown in the left panel and negative particles: are shown in the right panel) measured at mid-rapidity ($y < 0.1$) for $\sqrt{s} = 62.4$ GeV in $p+p$ collisions. Statistical errors are shown with bars whereas the systematic errors are shown with the shaded band.</i>	136
6.6	<i>Identified transverse momentum spectra for K^\pm, p and \bar{p} (positive particles: are shown in the left panel and negative particles: are shown in the right panel) measured at mid-rapidity ($y < 0.1$) for $\sqrt{s} = 62.4$ GeV in $p + p$ collisions. Statistical errors are shown with bars whereas the systematic errors are shown with the shaded band.</i>	137

6.7	Mid-rapidity π^-/π^+ ratio in $p+p$ collision as a function of p_T . Statistical errors are shown with the bars whereas the systematic uncertainties are shown with the vertical boxes.	138
6.8	Mid-rapidity K^-/K^+ and \bar{p}/p ratios in $p+p$ collision as a function of p_T . Statistical errors are shown with the bars whereas the systematic uncertainties are shown with the vertical boxes. K^-/K^+ ratio is shown in the left panel and \bar{p}/p ratio is shown in the right panel.	139
6.9	Mid-rapidity K^+/π^+ and K^-/π^- ratios in $p+p$ collision as a function of p_T . Statistical errors are shown with the bars whereas the systematic uncertainties are shown with the vertical boxes. K^+/π^+ ratio is shown in the left panel and K^-/π^- ratio is shown in the right panel.	140
6.10	Mid-rapidity p/π^+ and \bar{p}/π^- ratios in $p+p$ collision as a function of p_T . Statistical errors are shown with the bars whereas the systematic uncertainties are shown with the vertical boxes. p/π^+ ratio is shown in the left panel and \bar{p}/π^- ratio is shown in the right panel.	140
6.11	Mid-rapidity π^-/π^+ ratio in $p+p$ collision as a function of p_T . Statistical errors are shown with the bars whereas the systematic uncertainties are shown with the vertical boxes.	141
6.12	Mid-rapidity K^-/K^+ and \bar{p}/p ratios in $p+p$ collision as a function of p_T . Statistical errors are shown with the bars whereas the systematic uncertainties are shown with the vertical boxes. K^-/K^+ ratio is shown in the left panel and \bar{p}/p ratio is shown in the right panel.	142
6.13	Mid-rapidity K^+/π^+ and K^-/π^- ratios in $p+p$ collision as a function of p_T . Statistical errors are shown with the bars whereas the systematic uncertainties are shown with the vertical boxes. K^+/π^+ ratio is shown in the left panel and K^-/π^- ratio is shown in the right panel.	143

6.14	Mid-rapidity p/π^+ and \bar{p}/π^- ratios in $p + p$ collision as a function of p_T . Statistical errors are shown with the bars whereas the systematic uncertainties are shown with the vertical boxes. p/π^+ ratio is shown in the left panel and \bar{p}/π^- ratio is shown in the right panel.	143
6.15	Identified transverse momentum spectra for π^\pm , K^\pm , p and \bar{p} (positive particles: filled symbols in left panel and negative particles: open symbols in right panel) measured at mid-rapidity ($ y < 0.1$) $\sqrt{s} = 62.4$ GeV in $p+p$ collisions. Errors are both statistical and systematic added in quadrature. The size of the errors are smaller than the symbol size. Different fits functions used to obtain the dN/dy and the $\langle p_T \rangle$ are also shown.	144
6.16	The dN/dy measurements from the STAR experiment at $\sqrt{s} = 62.4$ GeV in $p+p$ collisions. The results are also shown for dN/dy calculated in the model calculations.	145
6.17	The dN/dy measurements from the STAR experiment at $\sqrt{s} = 62.4$ GeV in $p + p$ collisions. The results are also shown for dN/dy measurements in the PHENIX experiment.	146
6.18	The $\langle p_T \rangle$ measurements from the STAR experiment at $\sqrt{s} = 62.4$ GeV in $p + p$ collisions. The results are also shown for $\langle p_T \rangle$ calculated in the model calculations.	148
6.19	The $\langle p_T \rangle$ measurements from the STAR experiment at $\sqrt{s} = 62.4$ GeV in $p + p$ collisions. The results are also shown for $\langle p_T \rangle$ obtained in the PHENIX experiment.	148
B.1	Quark and antiquark space-time trajectories in the Lund string fragmentation model. The two vertices (V_0 and V_1), where new quark-antiquark pairs are produced are also shown.	157

List of Tables

3.1	<i>The Summary of RHIC runs [58].</i>	55
3.2	<i>The List of some RHIC design parameters.</i>	57
3.3	<i>Basic Parameters and its associated hardware for the STAR TPC . .</i>	73
3.4	<i>Distortion Corrections in STAR TPC [68].</i>	85
4.1	<i>The event quality cuts.</i>	99
4.2	<i>The track quality cuts</i>	102
D.1	<i>Invariant yields of π^\pm at mid-rapidity ($y < 0.1$) in $p + p$ collisions at $\sqrt{s} = 62.4$ GeV. The errors given are both statistical and systematic.</i>	164
D.2	<i>Invariant yields of K^\pm at mid-rapidity ($y < 0.1$) in $p + p$ collisions at $\sqrt{s} = 62.4$ GeV. The errors given are both statistical and systematic.</i>	165
D.3	<i>Invariant yields of p and \bar{p} at mid-rapidity ($y < 0.1$) in $p + p$ collisions at $\sqrt{s} = 62.4$ GeV. The errors given are both statistical and systematic.</i>	166
D.4	<i>Antiparticle to particle ratio of π^-/π^+ at mid-rapidity ($y < 0.1$) in $p + p$ collisions at $\sqrt{s} = 62.4$ GeV. The errors given are both statistical and systematic.</i>	167
D.5	<i>Antiparticle to particle ratio of K^-/K^+ at mid-rapidity ($y < 0.1$) in $p + p$ collisions at $\sqrt{s} = 62.4$ GeV. The errors given are both statistical and systematic.</i>	168

D.6	<i>Antiparticle to particle ratio of \bar{p}/p at mid-rapidity ($y < 0.1$) in $p+p$ collisions at $\sqrt{s} = 62.4$ GeV. The errors given are both statistical and systematic.</i>	169
D.7	<i>Unlike particle ratio of K^+/π^+ at mid-rapidity ($y < 0.1$) in $p+p$ collisions at $\sqrt{s} = 62.4$ GeV. The errors given are both statistical and systematic.</i>	170
D.8	<i>Unlike particle ratio of K^-/π^- at mid-rapidity ($y < 0.1$) in $p+p$ collisions at $\sqrt{s} = 62.4$ GeV. The errors given are both statistical and systematic.</i>	171
D.9	<i>Unlike particle ratio of p/π^+ at mid-rapidity ($y < 0.1$) in $p+p$ collisions at $\sqrt{s} = 62.4$ GeV. The errors given are both statistical and systematic.</i>	171
D.10	<i>Unlike particle ratio of p/π^- at mid-rapidity ($y < 0.1$) in $p+p$ collisions at $\sqrt{s} = 62.4$ GeV. The errors given are both statistical and systematic.</i>	172
D.11	<i>Particle yield per unit rapidity (dN/dy) and average transverse momentum ($\langle p_T \rangle$) for π^\pm, K^\pm, p and \bar{p} at mid-rapidity ($y < 0.1$) in $p+p$ collisions at $\sqrt{s} = 62.4$ GeV. The errors given are both statistical and systematic added in quadrature.</i>	172

ABSTRACT

Title of Thesis : Particle Ratios and Transverse Momentum Spectra at RHIC Energies

The first low energy nuclear collision experiment performed by Rutherford was able to resolve the charged nucleus inside the neutral atom. High energy collisions were able to resolve the existence of nucleons and eventually quarks bound within these nucleons. The current goal of relativistic heavy ion collisions is to produce a new state of matter where quarks decouple from nucleons and behave as quasi-free particles. This is called “Quark Gluon Plasma” (QGP). The evolution of the QGP may allow us to better understand the evolution of universe itself. The theory, which at present is believed to give the best description of the strong forces is QCD (Quantum ChromoDynamics). In QCD, the fundamental interactions are believed to be between quarks and gluons, and nucleons are seen as bound states of three quarks held together by gluon exchange. The concept of QCD was first given by David Politzer, Frank Wilczek and David Gross in 1970, for which they were awarded the 2004 Nobel Prize in Physics.

The ultra-relativistic heavy-ion collisions provide an indispensable laboratory for investigating the behavior of nuclear matter under extreme conditions of temperature and/or pressure as those existing a few moments after the “Big Bang”. In these collisions very hot and dense nuclear matter is produced having an estimated temperature of about trillion degrees (10^{12}), and density several times higher than that of normal nuclear matter. Under these conditions, a phase transition is believed to occur leading to the “deconfinement” of partons, a state where quarks and gluons are no longer bound in individual hadrons but instead can freely move inside the whole interaction region. Such a state is also referred to as the QGP. RHIC (Relativistic Heavy Ion Collider) is the first machine in the world capable of colliding heavy-ions

as well as nucleons and its complex is composed of long chain of particle accelerators and detectors. Its main purpose is to study the fundamental properties of the matter from elementary particles to the evolution of universe. Besides, RHIC we have various other experiments world wide viz. SPS, LHC at CERN Geneva; FAIR at GSI, Germany etc. serving in their own specified objectives pertaining to the field of high energy physics. Even though the LHC begins its first data taking in 2009, lots of physics is yet to be explored from RHIC not only with $p + p$ collisions but also with the heavy ion collisions.

Many QGP signatures have been proposed which include rare probes (e.g. direct photon, dilepton production, jet modification) as well as bulk probes (e.g. enhanced strangeness and anti baryon production, strong collective flow). While rare probes are most robust, they are relatively difficult to measure. On the other hand, signals of QGP that are related to the bulk of the collision are most probably disguised or diluted by other processes like final state interaction. Simultaneous observations and systematic studies of multiple QGP signals in the bulk matter would, however, serve as strong evidence for QGP formation. These bulk properties include strangeness and baryon production rates and collective radial flow. Furthermore, these bulk observables can be studied via transverse momentum (p_T) spectra of identified particles in heavy ion collisions in comparison to nucleon-nucleon and nucleon-nucleus reference systems. The observable used to study the enhancement in the strangeness is the *Particle Ratio* of the strange to the non-strange particle. Thus, study of particle ratios are significant in many ways, as it provides us useful information regarding the chemical freeze-out temperature and many important phenomena occurring during the evolution of the system of two particles colliding with high energies. Proton-proton collisions are the simplest case of nucleus-nucleus collisions and provide an essential baseline to determine what's new in heavy-ion collisions. While colliding nuclei, the

bulk properties of the nuclear matter can be studied under extreme conditions i.e. nucleus-nucleus (AA) collisions probe the material science of nuclear matter, the $p+p$ collisions more directly probe the hadronization. Thus, by measuring the size of $p+p$ collisions, we get the information about what the collisions looked like when hadrons were created—this gives us insight into the mysterious process of hadronization. The structure of the inclusive p_T spectra from relativistic nuclear collisions is affected by several aspects of collision dynamics and by the final state hadronization process. Its only through the comparison of $p+p$ collisions with the $d+Au$ and $Au+Au$ transverse momentum spectra at RHIC which suggest that a form of color-deconfined matter has been created in $Au+Au$ collisions. Particle-production mechanism which could determine spectrum structure include soft parton scattering followed by longitudinal or string fragmentation and hard parton scattering followed by transverse scattering.

This thesis work pertains to Solenoidal Tracker At RHIC (STAR) Collaboration housed at Brookhaven National Laboratory (BNL), USA as a part of the Relativistic Heavy Ion Collider (RHIC) facility. Three other experiments which are also operating there as a part of the heavy ion programme are; Pioneering High Energy Nuclear Interaction eXperiment (PHENIX), Broad RAnge Hadron Magnetic Spectrometer (BRAHMS) and PHOBOS. STAR and PHENIX are large, multipurpose detectors and at the moment only these two experiments are in operational mode for the data taking where as the other two have ceased working since 2007. The STAR detector is a “Hadronic Signal” detector. It is a large acceptance cylindrical detector system with a complete azimuthal coverage over the central rapidity region. It consists of several sub-detectors and the entire system is located within 0.5 Tesla solenoidal magnet which provides uniform magnetic field for the charged particle momentum analysis. It uses Time Projection Chamber (TPC) as its primary tracking device which performs the role of 3-D camera capturing the images of the emitted sub-atomic particles. The

STAR detector along with its various sub-detectors will be discussed in detail in the chapter 3 of this thesis.

The research work embodied in this thesis is based on the data analysis of the $p+p$ collisions at $\sqrt{s} = 62.4$ GeV collected by STAR experiment in the 2006 experimental run of the RHIC. The main physics observables studied in this thesis are the identified particle spectra, their ratios, mean p_T and the particle yield per unit rapidity of the charged hadrons.

One of the major topic studied in this thesis is the p_T spectra of the charged particles. Such measurements are essential to study the collective properties of the strongly interacting matter and also to study the physics of the critical point as the shape of the p_T spectra carries the combined effect of – the temperature in the collision and the expansion of the system. We have also presented the results of various like and unlike particle ratios. This observable plays a significant role in the understanding of the process of hadronization and also about the evolution of the system formed during the high energy collisions. The particle ratios are also studied in order to understand the freeze-out dynamics in the ultra-relativistic collisions. The particle yield per unit rapidity (dN/dy) and the mean p_T are also obtained from the identified spectra of the particles. The strange behavior of the mean p_T as a function of charged particle multiplicity is an important tool in understanding the mechanism of the phase transition from the QGP to the hadronic phase.

This thesis is divided into seven chapters and the brief contents of the chapters are :

Chapter 1 : In this chapter an introduction to the particle physics is given with some historical background. Some of the key concepts of this dynamical field are taken into consideration like, the QCD , QGP and its phase diagram. A brief introduction about the ultrarelativistic heavy ion collisions is also discussed.

Chapter 2 : The overview of literature for the transverse momentum spectra of the charged particles, their ratios along with the experimental and theoretical implications are taken into consideration in this chapter. The basic mechanism of the $p + p$ collisions is also discussed in detail. The Monte Carlo models viz. PYTHIA, PHOJET and HIJING are also discussed briefly along with their physics mechanisms.

Chapter 3 : The experimental set up of the RHIC and especially, the STAR detector is given in detail in this chapter. All the sub detectors in the STAR are discussed in relation to their experimental functions and utilities. The detector set up is nicely explained with the proper illustrations wherever necessary.

Chapter 4 : In this chapter, the analysis techniques employed to carryout the particle production study in $p + p$ collisions as undertaken in this thesis work are given. The unique picture of how the event as well as the track reconstruction is done in the real experimental scenario has also been presented nicely in this chapter. The information about the data set used in this thesis is also presented with some basic quality assurance plots. The particle identification technique used in the STAR's Time Projection Chamber is also discussed and the raw particle yield is extracted with the additional use of the z variable which will be extensively taken with various illustrations for different charged particles in different p_T windows in this chapter.

Chapter 5 : This chapter is dedicated to the different types of corrections done to the uncorrected particle spectra to obtain the final yields. The detailed procedure of each correction is given along with their corresponding results. Since, the study of the corrections in the spectra analysis requires the use of the simulation as well the embedding techniques to achieve its goals, so, the software techniques in relation to the given detector set up are also discussed. The results from the simulation study are also compared with the real data measurements.

Chapter 6 : The results for the corrected spectra for π^\pm , K^\pm , p and \bar{p} for the $p + p$

collisions at center of mass energy 62.4 GeV are presented in this chapter. The same measurements are done with the simulation models discussed in the chapter 2. From the transverse momentum spectra distributions, the mean p_T and the particle yield per unit rapidity are also obtained. The p_T spectra, mean p_T and the dN/dy results obtained from the real data are compared with the similar measurements done in the model study. Furthermore, all the results obtained in this thesis work are also compared with the similar study done by PHENIX experiment. The like as well as unlike particle ratios for the different particles in the real data are also obtained and compared with the results with the model calculations as well as with the PHENIX experiment.

Chapter 7 : The results presented, compared with the model calculations and PHENIX experiment are summarized in this chapter. The physics conclusion for the work done in this thesis is also made in the light of the various published results as well as the theoretical predictions for the spectra analysis. The observations made in this study are found to be consistent with the results obtained by the PHENIX experiment in the field of high energy physics.

Chapter 1

Introduction to high energy physics

1.1 Heavy-ion physics

Heavy-ion physics is devoted to the study of matter under the extreme conditions which are created in collisions of heavy-ions at large energies. Experiments in Heavy Ion Physics are carried out using accelerator and collider facilities available at laboratories throughout the world notably the Relativistic Heavy Ion Collider (RHIC) at Brookhaven National Laboratory (BNL), USA, the Super Proton Synchrotron (SPS) and the Large Hadron Collider (LHC), CERN, Switzerland. This Chapter gives an overview of some basic concepts of Heavy Ion Physics.

The search for the fundamental building blocks of all matter in the universe has always been a central issue in physics. As our understanding of physical laws improves, our view changes on what constitutes the elementary particles – particles that cannot be made as composites of others. These days, the accepted view is that all matter is made of quarks and leptons. The only additions to the list are photons, W^\pm and Z^0 bosons, gluons, and gravitons, particles mediating electromagnetic, weak, strong, and gravitational interactions, respectively. These assumptions are based on the predictions of the Standard Model of particle physics (with the exclusion of gravity

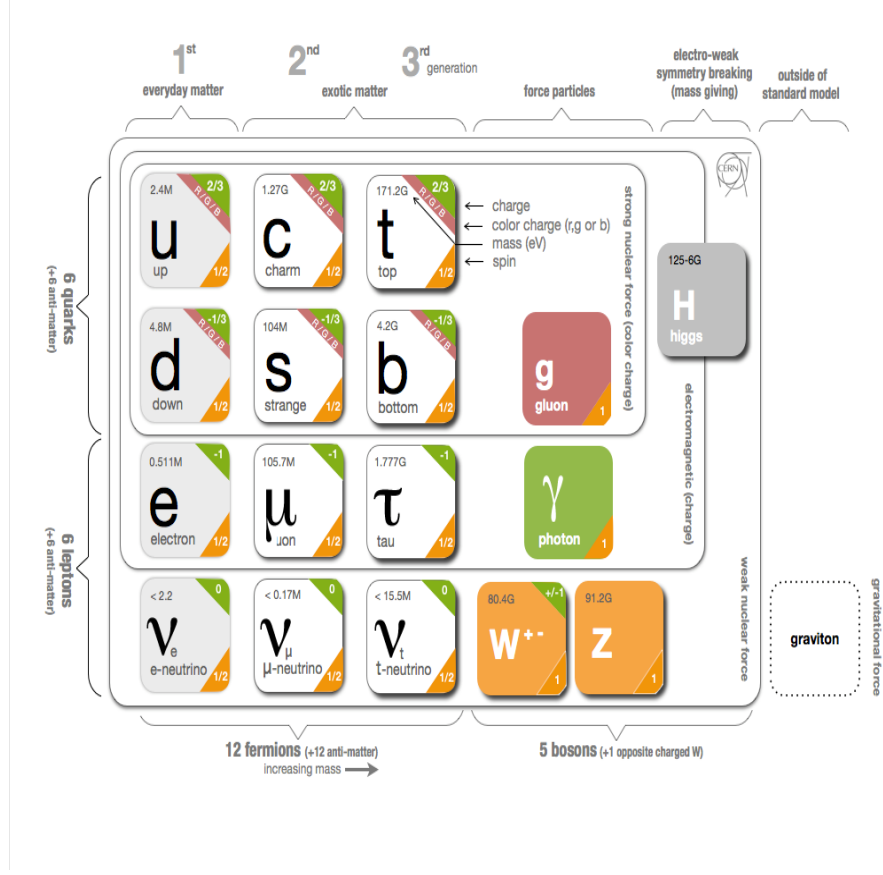


Figure 1.1: *The info-graphic of a given Standard Model*

and its mediator particle “graviton”) which introduces the basic particles, forces, and the rules of their combinations and interactions [1].

Three of the fundamental forces result from the exchange of force-carrier particles, which belong to a broader group called “bosons”. Particles of matter transfer discrete amounts of energy ($\geq \frac{\hbar}{\Delta t}$ as per Heisenberg’s energy-time uncertainty relation) by exchanging bosons with each other. Each fundamental force has its own corresponding boson – the strong force is carried by the “gluon”, the electromagnetic force is carried by the “photon”, and the “W and Z bosons” are responsible for the mediating weak force. Although not yet found, the “graviton” should be the corresponding force-carrying particle of gravity. The Standard Model includes the electromagnetic, strong and weak forces and all their carrier particles, and explains well how these forces act

on all of the matter particles. However, the most familiar force in our everyday lives, gravity, is not part of the Standard Model, as fitting gravity comfortably into this framework has proved to be a difficult challenge. With the quantum theory describing the micro world, and the general theory of relativity describing the gravitation, it is difficult to fit them into a single framework because of the non-linear nature of the general relativity. No one has managed to make the two mathematically compatible in the context of the Standard Model. But luckily for particle physics, when it comes to the minuscule scale of particles, the effect of gravity is so weak as to be negligible. Only when matter is in bulk, at the scale of the normally visible objects or of the planets for example, that the effect of gravity dominate. So the Standard Model still works well besides its reluctant exclusion of one of the fundamental forces [2]. Figure 1.1 summarizes the particles of the Standard Model, whereas Fig. 1.2 gives a graphical overview of the interactions of these particles. All particles in the Standard Model have antiparticles with the same mass but with opposite electrical charge and color charge. Antiparticles are denoted with a bar, so that an anti-up quark is labelled as \bar{u} . Leptons have only been observed as free particles whereas quarks are not. In the present Universe the only quarks observed are the u and d quarks which are found in the neutrons (udd) and protons (uud). In general, composite particles built from quarks are called *hadrons*. Hadrons containing two quarks are called *mesons* while those composed of three quarks are known as *baryons*. Thus, the neutron and the proton are baryons. The conservation of certain quantum numbers (electrical charge, spin, isospin etc.) determines the possible hadronic states. Examples of mesons are the pions (π^\pm) and kaons (K^\pm) [3].

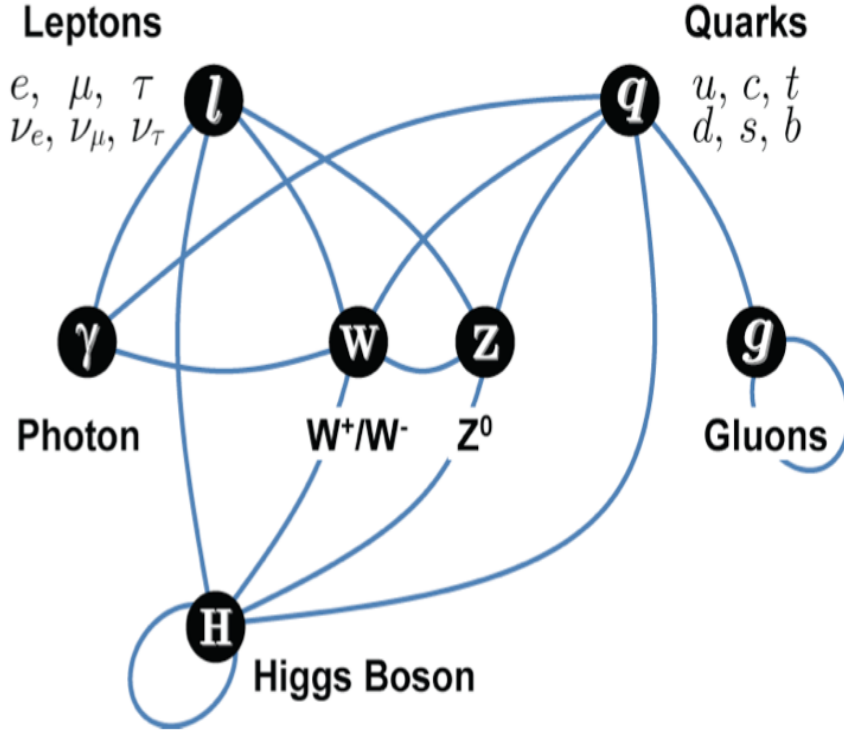


Figure 1.2: *The allowed interactions as per the Standard Model*

1.2 Quantum Chromodynamics (QCD)

The dynamic theory of quarks and gluons that describes color interactions is known as Quantum Chromodynamics (QCD), and is a gauge theory of the non-Abelian color symmetry group $SU(3)$. This theory is very similar to Quantum Electrodynamics (QED), which describes the electromagnetic interactions of charges with photons. As it is well known that, QED is an abelian gauge theory with symmetry group $U(1)$, whereas being a gauge theory of color symmetry, QCD also contains massless gauge bosons (namely gluons) that have properties similar to photons. There are however, essential differences between the two theories, which arise because of the different nature of the two symmetry groups. The fundamental difference between QED and QCD is that, the photon, which is the carrier of the force between the charged particles, is itself charge neutral, and as a result, the photon does not interact

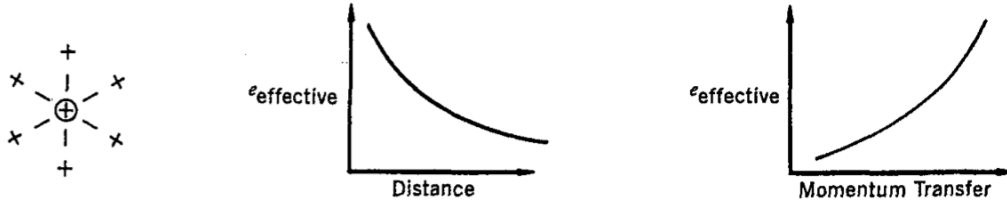


Figure 1.3: Polarization of a dielectric medium around a positive electric charge, and the effective value of the charge as a function of distance and of momentum transfer.

with itself. In contrast, the gluon, which is the mediator of the color interactions, apart from having color charge is also self-interacting. Another consequence of the non-Abelian nature of the color symmetry is related to how color-neutral states are formed. Consider, e.g., a red-colored quark, we can obtain a color-neutral system by combining the red quark with an anti-red antiquark. This is quite similar to how electric charges add. However, because three quarks with distinct colors can also yield a color-neutral baryon, there must therefore be an alternative way of obtaining a color-neutral combination from three colored quarks, which is obviously different from the way electric charges add together.

The difference between color charge and electric charge has important physical consequences. For example, a classical test particle carrying positive charge polarizes a dielectric medium by creating pairs of oppositely charged particles (dipoles). Due to the nature of the Coulomb interaction, the negatively charged parts of the dipoles are attracted towards the test particle, while the positively-charged parts are repelled (see Fig. 1.3).

As a consequence, the charge of the test particle is shielded and the effective charge seen at large distance is smaller than the true charge carried by the test particle (electric field in a dielectric medium is reduced relative to that in vacuum by the value of the dielectric constant of the medium). In fact, the effective charge depends on the distance (or scale) at which we probe it at ever smaller distances, and

only asymptotically (at largest momentum transfers) that we obtain the true point charge of the test particle. Since the distance probed is inversely proportional to the momentum transfer, it is stated conventionally that the effective electric charge, or the strength of the electromagnetic interaction, increases with momentum transfer, and which seems purely a consequence of the screening of electric charge in a dielectric medium. Because of the presence of quantum fluctuations, a similar effect arises for charged particles in vacuum, the impact of which is that the fine structure constant $\alpha=e^2/\hbar c$ increases, though only slightly, with momentum transfer. This has been confirmed in high-energy e^+e^- scattering, where α is found to be $1/127.9$, or $\sim 7\%$ larger than at low energy.

In contrast, a test particle carrying color charge polarizes the medium in two ways. First, just as in the case of QED, it can create pairs of particles with opposite color charge. But it can create three particles of distinct color, while still maintaining overall color neutrality. Consequently, for the color force, the effect of color charge on a polarized medium is more complex. A detailed analysis of QCD reveals that the color charge of a test particle is, in fact, anti-screened. In other words, far away from the test particle, the magnitude of the effective color charge is larger than that carried by the test particle. In fact, as we probe deeper, the magnitude of this charge decreases. Thus, the qualitative dependence of the color charge on probing distance, or on the probing momentum transfer, is exactly opposite of that for electromagnetic interactions (see Fig. 1.4).

This implies that the strength of the strong interaction decreases with increasing momentum transfer, and vanishes asymptotically. Conventionally, this is referred to as *asymptotic freedom*, and refers to the fact that, at infinite energies, quarks behave as essentially free particles, because the effective strength of the coupling for interactions vanish in this limit (Asymptotic freedom of QCD was discovered

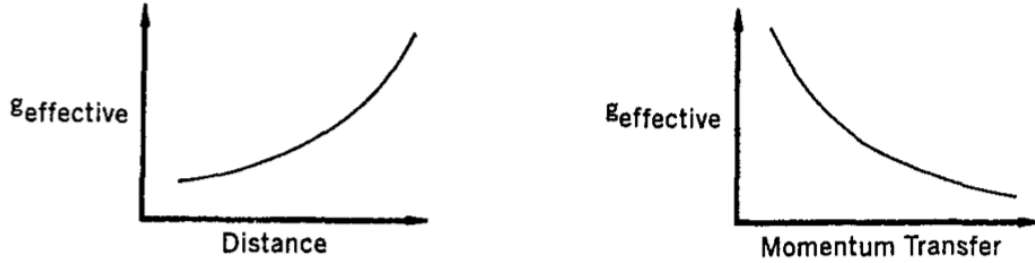


Figure 1.4: *The effective value of color charge as a function of probing distance and of momentum transfer.*

independently by David Politzer and Frank Wilczek & Gerard Hooft). This principle has the additional implication that, in very high energy collisions, hadrons consist of quarks that act as essentially free and independent particles. This limit of QCD for high-energy hadrons is known as the parton model, which agrees with many aspects of high-energy scattering [4].

The original parton model claimed that baryons, such as protons, neutrons, and Δ baryons, consist of 3 fractionally charged quarks while mesons, such as π 's and ρ 's, consist of a quark-antiquark pair. This naive model required modification with the observation of the doubly charged Δ^{++} , as its decay properties suggest that it is made up of three identical spin 1/2 quarks, thus violating the Pauli exclusion principle. A new quantum number called color was introduced to fully anti-symmetrize the Δ^{++} wave function. This three component color charge is treated similarly to the electric charge in Quantum Electrodynamics (QED) except the propagators of the field are color charged gluons while the photon of QED has no electric charge. Quantum Chromodynamics (QCD), the theory of colored interactions, attempts to incorporate all the experimental properties of quarks and gluons even though these particles have never been observed as free particles [5].

In QCD, the color charge is carried by quarks and gluons and particles carrying it interact strongly. This means that gluons mediate the strong force between quarks

and they interact strongly themselves. This is not the case for e.g., photons that mediate the electromagnetic force without self-interactions. QCD is a non-Abelian gauge theory, which means that the strong interaction shows almost no resemblance to e.g., the electromagnetic interactions, which is believed to follow the Abelian QED theory. To illustrate this, the quark-quark potential calculated from QCD is shown in Fig. 1.5. It is seen that the ‘quark-quark potential rises with distance, indicating that it will require an infinite amount of energy to separate two quarks. This is the theoretical explanation of the phenomenon of *quark confinement* in hadrons. Figure 1.5 also reveals another important property of the strong interaction, namely that the qq-potential drops as the distance between the quarks becomes small, a concept known as *asymptotic freedom*. Confinement and asymptotic freedom are key concepts in the dynamics of heavy-ion collisions. To further illustrate these concepts let us consider two scenarios, firstly: What happens if a quark is pulled (e.g., in scattering experiments) away from the other quarks in a hadron? According to QCD, the potential between the quark and the hadron will increase until there is enough energy to produce a new quark-antiquark pair, a phenomenon known as pair production. The new particles will then recombine to form hadronic states. In this way, instead of isolating a single quark, the quark-antiquark pairs will be created to form new particles. The second scenario is: What if it was possible (e.g., in heavy ion collisions) to create a high enough density of quarks in a nucleus (or a region of a compatible volume) for them to experience asymptotic freedom? The discoveries at RHIC supports the conjecture that this leads to the formation of a state of matter observed briefly and immediately after the Big Bang ($t \leq 10^{-6}$ s). This state of matter is called a Quark Gluon Plasma (QGP), since it consists of ‘quasi free’ quarks and gluons. The formation and study of the QGP is one of the primary challenges in *Heavy Ion Physics*.

Theoretically speaking, the concept of quark confinement and its disappearance

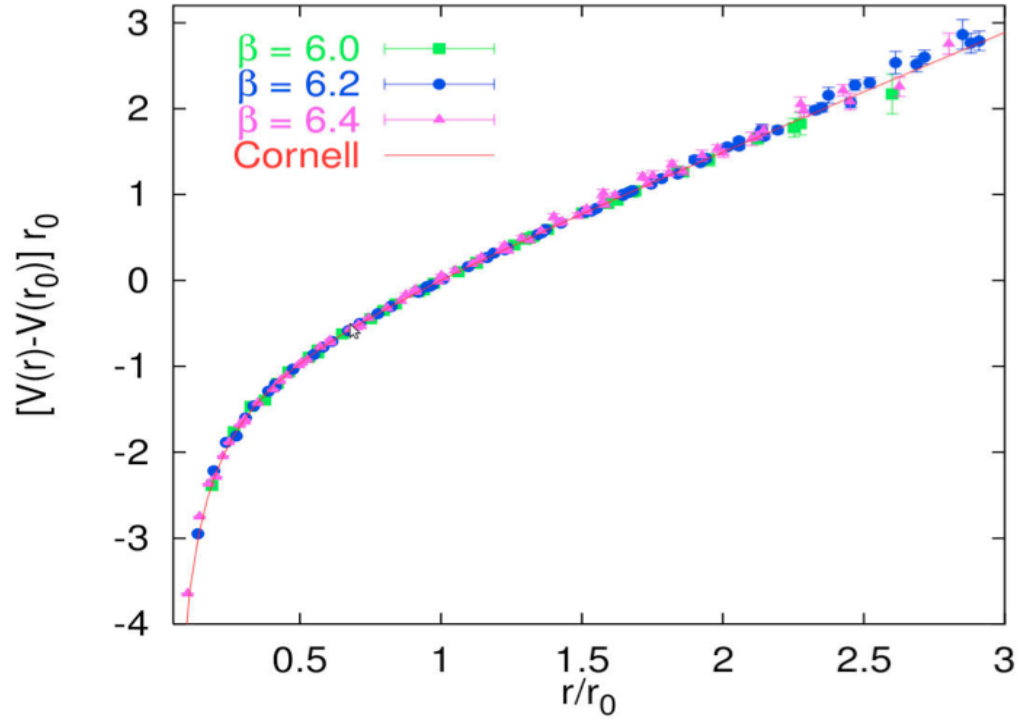


Figure 1.5: The quark-quark potential calculated from $lQCD$. In the plot $r_0 = 0.5$ fm and $V(r_0) = 0$ [6].

in the QGP phase is a feature of the so called chiral symmetry restoration. The chiral condensate, defined as the vacuum expectation value of the quark condensate, $\langle\psi\bar{\psi}\rangle$ is non-zero in hadronic matter whereas it vanishes in the QGP phase, $\langle\psi\bar{\psi}\rangle \sim 0$. While a measurement of this quantity would bring immediate enlightenment on the formation of QGP, it is not possible to measure directly and therefore other experimental routes must be taken to study QGP formation.

For practical purposes there are two different QCD approaches: Lattice QCD (lQCD) where the calculations are done treating spacetime as discrete and perturbative QCD (pQCD) working from the Lagrangians of QCD in the high Q (momentum transfer) limit. The plot in Fig. 1.5 represents the former approach [7].

1.3 QGP and the QCD phase diagram

In ordinary matter, quarks are confined within hadrons. However, as the energy density is increased, a phase transition can occur to a state in which individual hadrons lose their identities, and quarks and gluons become free to move across a volume that is large compared to a hadron. Approximate lattice gauge theory calculations suggest that, it should occur at an energy density of the order $1 \text{ GeV}/fm^3$, i.e. about 6 times the energy density at the center of a heavy nucleus, and the resulting new state of matter is called Quark Gluon Plasma (QGP) [8]. So, we take the QGP to be a (locally) thermally equilibrated state of matter in which quarks and gluons are deconfined from hadrons, so that color degrees of freedom become manifest over nuclear, rather than merely nucleonic volumes [10]. This state is believed to have existed in the first few microseconds after the ‘Big Bang’ and it may exist today at the center of neutron stars. More prosaically, a quark-gluon plasma may be created briefly in collisions between heavy ions, if the collision energy is large enough. The steps involved in the formation of such a plasma, and its subsequent expansion and

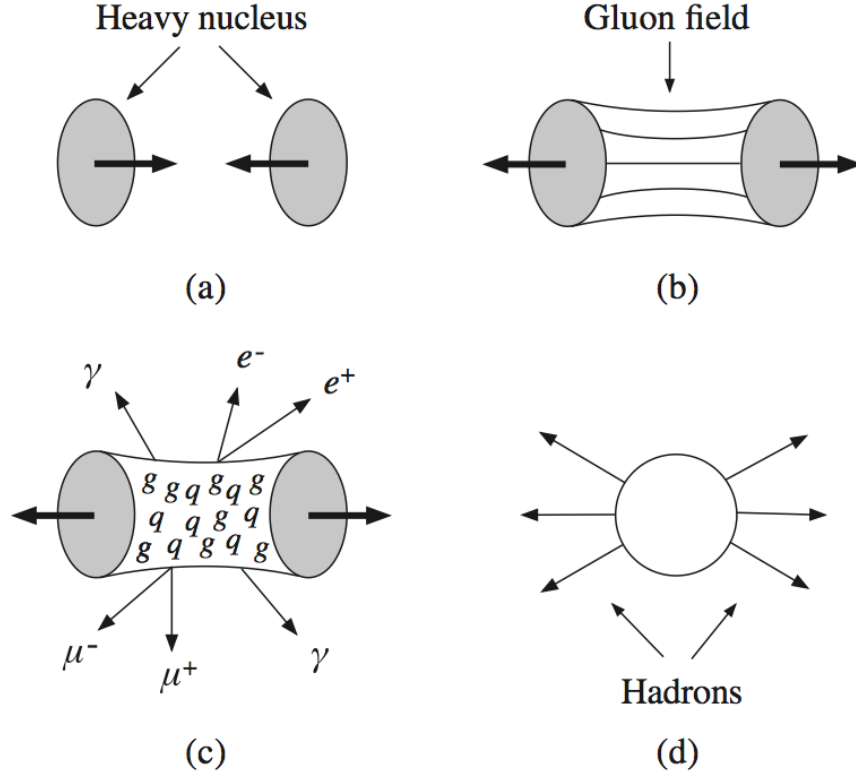


Figure 1.6: *Stages in the formation of a quark-gluon plasma and subsequent hadron emission: (a) two heavy nuclei collide at high energies (b) interact via the gluon field; (c) the very high energy-density produced causes the quarks and gluons to deconfine and form a plasma that can radiate photons and lepton pairs; (d) finally as the plasma cools, hadrons condense and are emitted [9].*

cooling to yield many hadrons, are illustrated schematically in Fig. 1.6.

The program of relativistic heavy-ion collisions whose primary goal is to study the phase diagram of QCD began with the fixed target experiments at SPS, CERN and AGS, BNL. Results of the experiments at CERN, SPS provided very exciting “evidence” in favor of QGP. However impressive the body of evidence is, the consensus in the field is that, while the evidence in the field is suggestive, the properties are not explored. Such a state of matter for which the analysis of all the four experiments at RHIC point to the existence, in the evolution of a system immediately following a $Au+Au$ collisions, of a near thermal, strongly interacting medium whose energy density and temperature clearly exceed the critical values predicted by QCD calculations for

a transition from ordinary hadronic states to the *Quark Gluon Plasma*. Prior to the RHIC data, it was often stated, that QGP should behave like ideal gas of quarks and gluons (i.e. like a weakly coupled plasma state). The RHIC data now confirms that the observed medium behaves more like an ideal fluid [10], in analogy to a strongly coupled plasma state. This state is referred to as *strongly coupled quark gluon plasma* (sQGP). Now, it is also possible to probe this deconfined state of matter using the LHC experiment at CERN.

Now, a key question is whether the energy density in the collisions is sufficient to have created a quark-gluon plasma and its subsequent cooling phases. There are many signatures for this, including the relative abundances of different final state particle types. For example, the large numbers of gluons in the plasma would lead to copious production of $s\bar{s}$ pairs via gluon fusion $gg \rightarrow s\bar{s}$, and hence production of strange particles in excess of that expected from nucleon-nucleon collisions at very high energies. On the other hand, the production of J/Ψ would be suppressed because the c and \bar{c} quarks produced (also from the gluon fusion) would be separated by many quarks of other flavors, leading instead to the production of charmed mesons, e.g. the D mesons. In practice, these arguments depend on how long the quarks remain in the central region of the plasma, and this will lead to angular dependences that provide the basis for more detailed tests. Present measurements are all consistent with the predicted energy density at which hadrons would be formed, while that of the initial fireball is considerably higher.

Ongoing experiments like RHIC and LHC and also the future experiments like CBM will play a crucial role in understanding the basic nature of deconfinement. Questions to be addressed include: ‘What is the nature of matter at the highest densities (experiments at RHIC suggest that the plasma behaves more like a liquid than a gas)?’, ‘Under what conditions can a quark-gluon plasma be made?’ and

‘What are the rules governing the evolution and the transition to and from this kind of matter?’ In order to map the QCD phase diagram with the accelerators and to review the experimental effort to study the QCD phase transitions, we compare the settings for the QCD phase transition during Big Bang to the prevailing experiments. Figure 1.7 shows the phase diagram of the hadronic and partonic matter. The QCD phase diagram and different regions studied with the accelerator experiments as well as the region of temperature and chemical potential prevailing in the first few μ seconds after the Big Bang is depicted in Fig. 1.7. A phase transition from the confined hadronic matter to the deconfined QGP matter is expected to happen at either high temperature (T) or large baryon chemical potential (μ_B). The strongly interacting matter would undergo different phases depending on the conditions of T and μ_B which is related to the density of baryons in the system. The different phases of this strongly interacting matter are; vacuum, hadron gas, nuclear matter, color super-conductor and quark gluon plasma. Normal nuclear matter consists of neutrons and protons, which are characterized by their low T and $\mu_B \sim 900$ MeV. The quarks and gluons are confined inside these composite particles which are known as hadrons. However, under the extreme conditions of high T or high μ_B (or both), quarks and gluons are set free due to the confinement breakdown. Deconfinement at large μ_B is considered to exist inside the core of neutron stars [11] and color super-conductors [12], where the nuclear matter is strongly compressed up to 10 times the normal nuclear density, while at very low μ_B the deconfinement by heating up nuclear matter can be achieved by colliding heavy nuclei at enormous energies, this phase is believed to have existed in the early universe or it can be reproduced in the laboratory in the experiments like LHC and RHIC. Along the first order phase transition line, the matter is believed to exist in mixed phase. Below it (*lower* T), the matter is in hadron gas phase and above it (*higher* T), the matter is in QGP

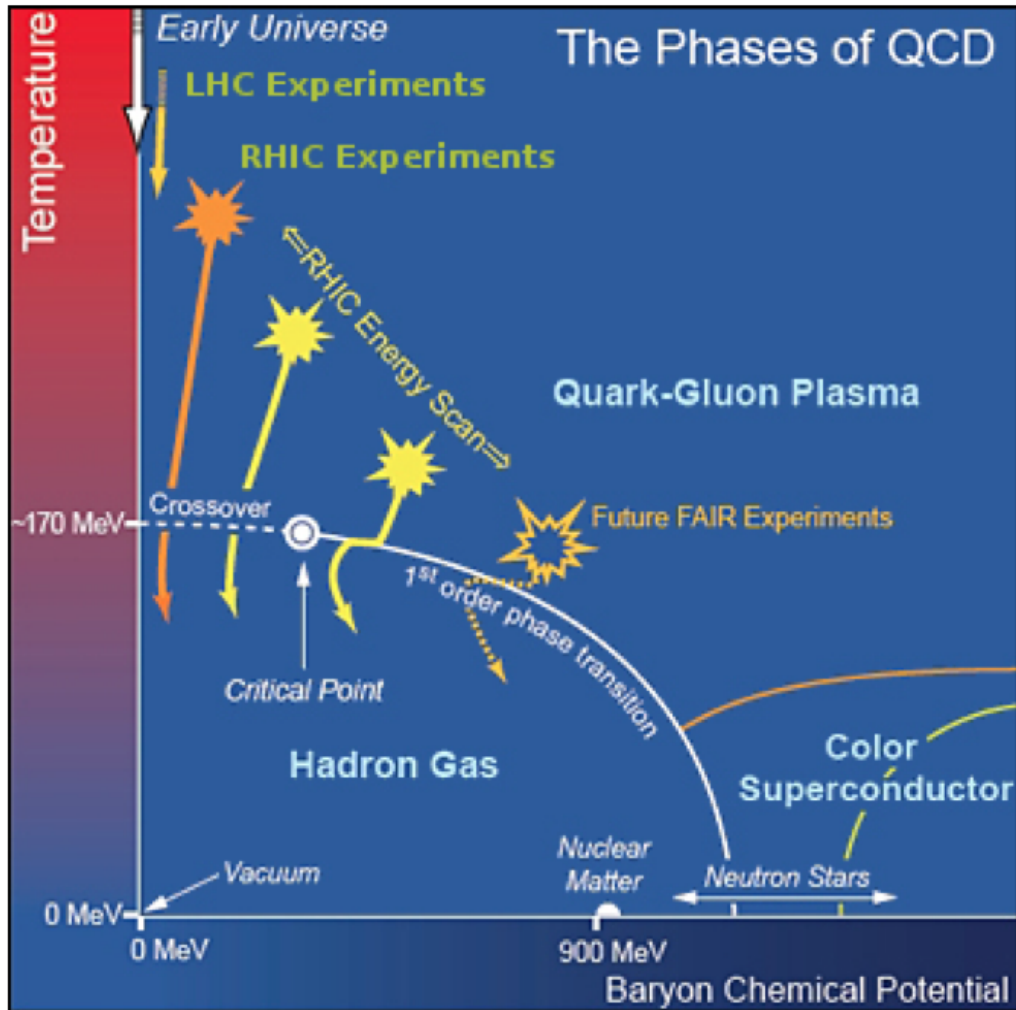


Figure 1.7: Schematic of QCD phase diagram. The solid lines show the phase boundaries for the indicated phases. The solid circle depicts the critical point where sharp distinction between the hadronic gas and QGP phases cease to exist. Possible trajectories for systems created in the QGP phase at different accelerator facilities are also shown.

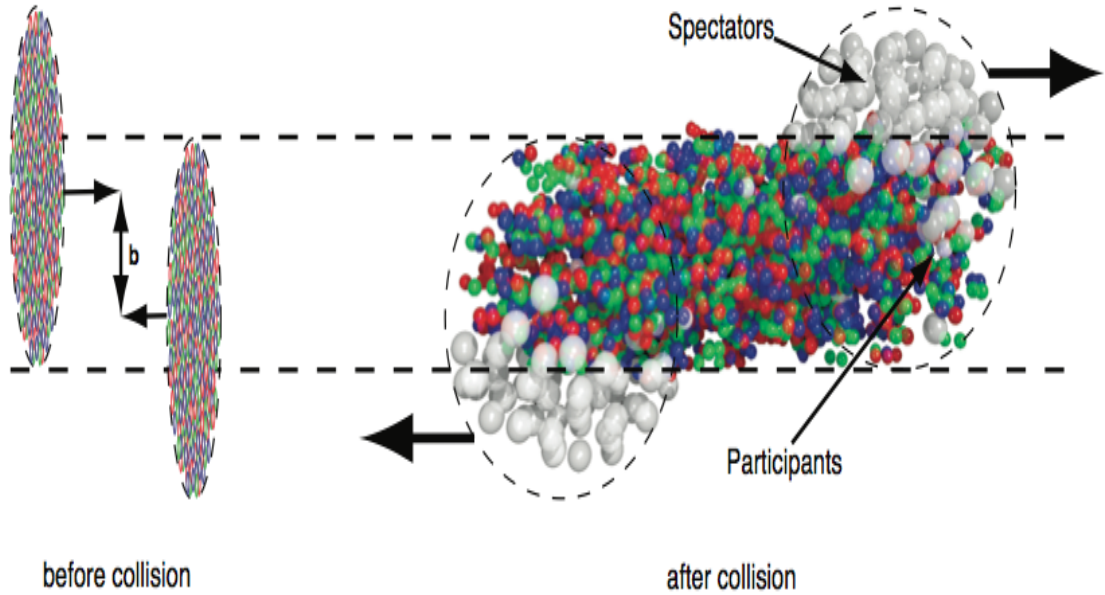


Figure 1.8: *Schematic view of two colliding nuclei in the geometrical model.*

phase. The point at which this line ends represents the *QCD critical point*, where first order phase transition ends [13]. Beyond this point, there is a smooth cross-over, where transition from one phase to another is very sharp. Locating the critical point both experimentally and theoretically is a great challenge. Current theoretical calculations are highly uncertain about the location of the critical point. The efforts had already been made and positive results attained in the RHIC Beam Energy Scan-I (BES-I) program undertaken in the year 2010-11, in which the data was recorded for 7 different beam energies ranging from 7.7 - 200 GeV. The purpose of BES-I was three-fold: (a) to search for threshold energies for the QGP signatures that have already been established at the top RHIC energies, thereby corroborating the past QGP discoveries; (b) to search for the signatures of first-order phase transition; and (c) to search for a QGP/QCD critical point.

1.4 Ultra-relativistic heavy ion collisions

In the ultra-relativistic heavy-ion collisions, two highly Lorentz contracted nuclei (appearing like “thin discs”) approach each other with velocities nearly equal to the velocity of light. Many nucleon-nucleon collisions occur in a region of geometrical overlap, which is determined by the distance between the centers of two colliding nuclei (called *impact parameter* (b)) as shown in Fig. 1.8. The impact parameter characterizes the centrality of the heavy-ion collisions. The corresponding nucleons in the overlapped region are so-called *participants*, which consists of protons and neutrons taking part in the collision. While the nucleons outside the overlapped region are called as *spectators*, which continue travelling almost unaffected. The participants interact with each other in the reaction zone, which lead to the formation of a hot and dense region, the fireball. The number of participating nucleons (N_{part}) is an important way of characterizing the heavy-ion collisions. It is also useful to know the number of binary nucleon-nucleon collisions N_{coll} . Both the N_{part} and N_{coll} can be calculated by a probabilistic model such as Glauber Model [14].

1.4.1 Space-time evolution

A schematic view of the ultra-relativistic nuclear collision involving various stages is presented in the top panel of Fig. 1.9. Sometimes it is useful to conceptualize such a collision in terms of a light cone diagram as shown in the lower panel of Fig. 1.9. Here, two Lorentz contracted nuclei approach each other with velocity nearly equal to the velocity of light and are colliding at $t = z = 0$. In the colliding instant, both contracted nuclei pass through each other in the region of geometrical overlap. Many processes involving parton-parton interaction with hard scattering occur in the overlapped region, which result in depositing a large amount of energy in a limited volume. The energy density and temperature at this stage is high enough

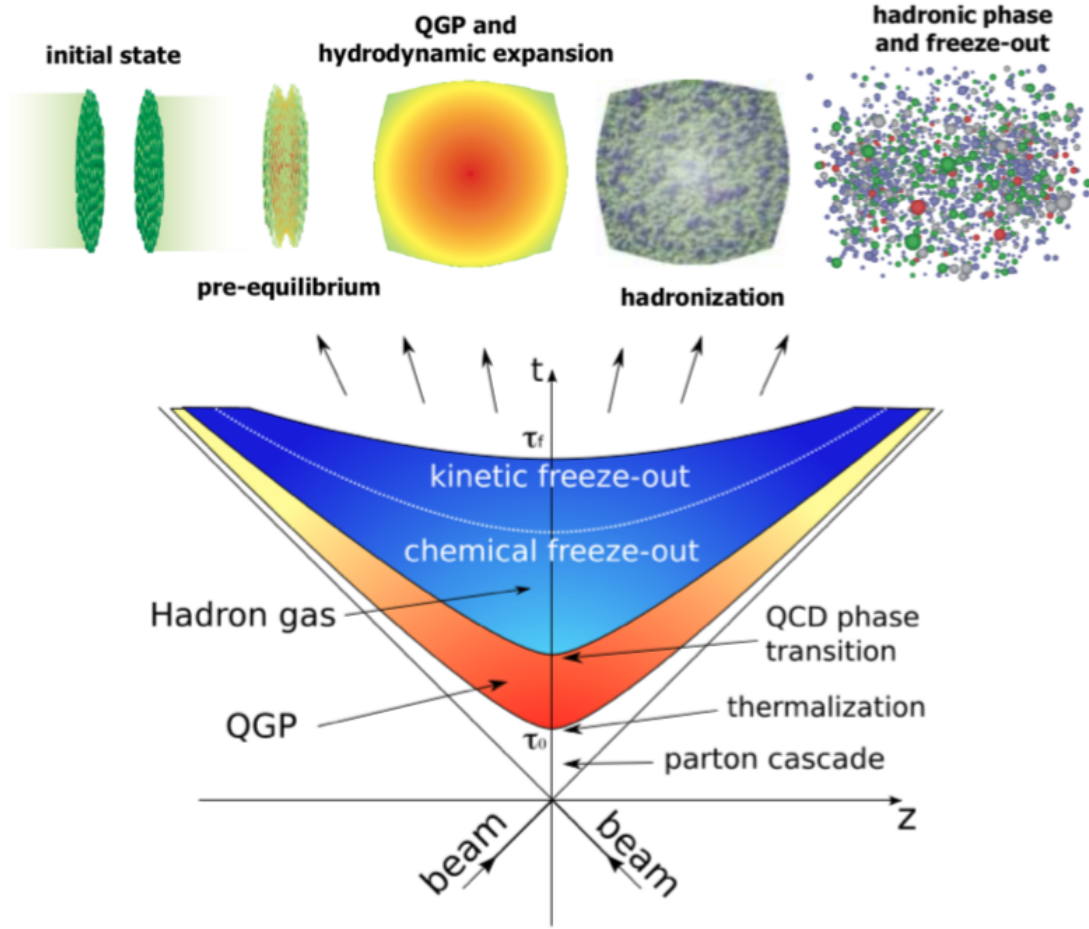


Figure 1.9: *Top panel : Overview of the space-time evolution in ultra-relativistic nuclear collision. Bottom panel : Schematic of various stages of heavy ion collision as a function of time and longitudinal coordinate (the collision axis)*

for the creation of QGP. The created matter expands in the space-time going through different stages till a large number of hadrons produced from the parton fragmentation arrive at the detectors eventually [15, 16].

The dynamics of heavy-ion collision can be nicely illustrated in the space-time diagram as shown in Fig. 1.9, where trajectories of the target and projectile nuclei are shown as thick lines. In simple words, the evolution of this picture is as :

- the two Lorentz-contracted nuclei interpenetrate each other. The tremendous temperature as well as energy density is supposed to be created due to high

momentum transfer owing to the hard scattering among the partons. The high momentum partons will interact inelastically and thereby lose their kinetic energy. The energy lost will lead to the creation of matter in the vicinity of collision which is often labelled as the fireball. If the fireball is hot enough the QGP will be formed. Also hard scattering processes with large momentum transfer will lead to the hadrons with large momentum.

- the further interaction of the particles (or the expansion of the fireball) drives the system towards chemical and thermal equilibrium. If QGP forms, the individual parton-parton scattering is expected to play an important role in thermalizing the system during this stage. The development of the collective flow is also believed to be originated at this moment. Rapid expansion (both in longitudinal and transverse direction, mainly former) lowers the temperature of the system and eventually approaches the critical temperature (T_c).
- As the system further expands, the inelastic collisions cease when the *chemical freeze-out temperature* (T_{ch}) is reached, which leads to the process of hadronization and at this moment the particle yields and ratios get fixed. The T_{ch} and μ_B obtained at this point could be used to study the QCD Phase diagram of the strongly interacting matter.
- As the system keeps evolving, eventually ceasing the elastic interactions when the *kinetic freeze-out temperature* (T_{fo}) is reached. At this moment, the momentum distribution of the particles get fixed and the hadrons can propagate freely thereafter.

1.4.2 Predicted signatures of QGP

Various experimental signatures have been associated with the formation of QGP and heavy-ion programmes have focussed on several of them. Here, the few of the observables that have been proposed as tell the tales of QGP are enlisted [10] :

1. *J/ Ψ Suppression*
2. *High p_T particle suppression : Jet Quenching*
3. *Strangeness Enhancement*
4. *Anisotropic Flow*
5. *Particle Ratios*

Moreover, it is interesting to know that we can only measure the final state particles in the experiment. These particles provide the very useful information to determine the initial conditions of the system via different mechanisms and probes. One such probe is the study of the “transverse momentum spectra” and the “particle ratios” of the various particles produced in the ultra-relativistic collisions. The detailed analysis for the production of π^\pm , K^\pm , p and \bar{p} in the light of these two observables (p_T spectra and particle ratios) at $\sqrt{s} = 62.4$ GeV with STAR experiment have been reported in this thesis.

1.5 Organization of the thesis

Although, some of the experimental data at SPS and RHIC have strongly indicated the existence of the QGP state, yet we still have no clear insight about what happens in the system formed in such high energy collisions, e.g., the space time extents of deconfinement state and the hadron gas. The particle spectra, therefore serve as a key

observable to investigate the space time evolution of the system and to understand a comprehensive picture of dynamics of expanding system from the formation of deconfined state to the hadron gas.

The work presented in this thesis involve the study of some of the important observables to understand the particle production mechanisms in high energy collisions. Also, it is very important to study the particle production as a function of both transverse momentum (p_T) and particle species which provide crucial input for modelling of hadronic interactions and the process of hadronization in such energetic collisions. The research work given in this thesis is based on the data analysis of the $p + p$ collisions at $\sqrt{s} = 62.4$ GeV collected by STAR experiment in the 2006 experimental run of the RHIC. The main physics observables studied in this thesis are p_T spectra, particle ratios, mean p_T and the particle yield per unit rapidity for the identified charged hadrons. *Chapter 2* gives a review of the observables like particle ratios and transverse momentum distribution in high energy collisions. The Monte Carlo models viz. PYTHIA, PHOJET and HIJING are also discussed briefly along with their physics mechanisms. *Chapter 3* gives a brief description of a RHIC accelerator facility and the STAR detector. *Chapter 4* contains the detail of the analysis methods and techniques used to study the various physics observables. The details of the particle identification in STAR detector to obtain the raw particle yields is also given in this chapter. *Chapter 5* gives the detail about the various corrections done to the uncorrected particle spectra to obtain the final yields. *Chapter 6* contains the final results for the invariant yields of π^\pm , K^\pm , p and \bar{p} along with their ratios. The results for the inclusive particle yield per unit rapidity (dN/dy) and the average transverse momentum ($\langle p_T \rangle$) are also discussed. The results are compared with the similar measurements obtained with Monte Carlo Models (PYTHIA, PHOJET) and also with those of the PHENIX experiment. *Chapter 7* finally summarizes and

concludes all the results obtained in this thesis.

Chapter 2

Elementary collisions, particle spectra and ratios

2.1 Introduction

In this chapter, the theoretical understanding of some basic properties of proton-proton collisions are discussed, with the special emphasis on the production of pions, kaons, protons and antiprotons. A short description of proton-proton collisions modelling is presented in Sec. 2.2 and Sec. 2.3. Some phenomenological models used to describe the particle production in proton-proton collisions and heavy ion collisions are also briefly described in the Sec. 2.4. The significance of the observables studied in this thesis is also emphasized in connection with the similar studies done previously at different energies and for the different systems (see Sec. 2.5).

2.2 Proton-proton collisions

The production of charged hadrons from the $p + p$ collisions is the main topic of this thesis and is an important area to test the predictions of QCD. While interesting in

their own right, the $p + p$ collisions provide a good reference or baseline for heavy ion collisions due to number of reasons. One of the main reasons is that the $p + p$ collisions have not been believed to create a QGP. Thus, the deviations in measured quantities in $p + p$ and heavy ion collisions can serve as a probe of the differences between the two systems. Therefore, if really no QGP is formed in $p + p$ collisions, then differences between the two systems are useful for directly probing the characteristics of the QGP formed in heavy ion collisions. However, it is noteworthy to mention that, it has indeed been proposed that collective effects, and possibly even the formation of a QGP, could occur in very high energy $p + p$ collisions [17].

Regardless of whether or not such a state is formed in $p + p$ collisions, these elementary measurements do have a full physics motivation in its own right, with an important contribution being the particle yields and their ratios as presented in this thesis. A schematic picture of a $p + p$ collisions is shown in Fig. 2.1.

Some worthy features of $p + p$ collisions are as enlisted below:

- ***Simpler System :*** A $p + p$ collision has a fewer components than a collision of two heavy ions. While the most central heavy ion collisions can involve up to ~ 200 separate nucleon-nucleon collisions, the $p + p$ collisions involve only one.
- ***No Collective Effects:*** The $p + p$ collisions have never been observed to exhibit the collective effects such as anisotropic transverse flow observed in heavy ion collisions. This means that properly scaled-up $p + p$ collisions can serve as a model for $A + A$ system without collective effects. It has been speculated that collective effects (most prominently flow) would begin to appear in high multiplicity $p + p$ collisions at LHC but this is yet to be observed. If one considers the energy density to be the crucial parameter, this certainly could be a possibility if enough energy was carried by the protons.
- ***Jet Studies:*** In heavy ion collisions, the observed high p_T suppression is

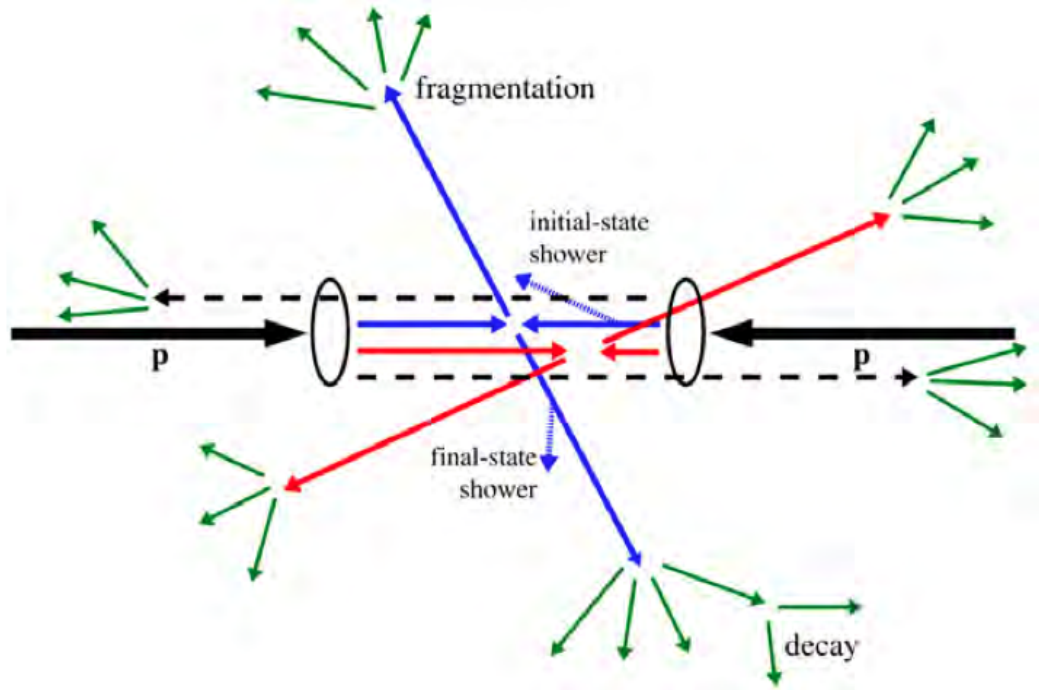


Figure 2.1: An incoming parton might branch ($q \rightarrow qg$) before the collision in an initial state shower. Similarly a parton branching after the collision is referred to as a final-state shower. After the collision, the color string span between the outgoing quarks and gluons. These fragments into colorless hadrons, which can be unstable and further decay [18].

often attributed to the interactions of the emitted jets with the hot and dense medium produced. The $p+p$ collisions allow for detailed studies of jets in a more fundamental environment since the mechanism of jet production is believed to be similar to the hard $q+q$ interactions.

While the system may seem simpler, studying $p+p$ collisions are not necessarily simpler than measuring properties of heavy ion collisions. There are several reasons for that. Firstly, all the accelerator effects that pollute the observations will affect the results in $p+p$ collisions the most because the particle production is much smaller in $p+p$ collisions. This makes it harder to distinguish signal and noise in $p+p$ collisions compared to heavy ion collisions where the higher multiplicities will make the signal ‘cleaner’. Secondly, there can be issues with the triggering of $p+p$ collisions where the low multiplicity makes it harder to detect the appropriate number of events. It requires accurate simulations to study the corrections for the lower trigger efficiency. These topics will be dealt in detail in the chapter 5.

2.3 Modelling of $p+p$ collisions

Proton-proton collisions are often well described by the Monte Carlo event generators which are based on perturbative QCD for hard scattering processes and use phenomenological models to describe the soft processes as well as many body dynamics that are present in $p+p$ collisions.

2.3.1 Classification of $p+p$ interaction

Colliding hadrons are color singlets. As they approach each other, they may exchange color octet gluon, making each hadronic cluster a color octet. To be able to separate into two separate systems, they need to exchange another gluon and become colorless.

As they move apart, color lines that connect them are stretched. Given time, this system gets complex and multi-particle production occurs. In $p+p$ (or more generally hadron-hadron) scattering, interactions are classified by the characteristics of the final states. Interactions can either be elastic or inelastic. Since interactions are characterized by their cross-sections, so one can also say that, in general the $p + p$ cross-section (σ_{pp}) can be of these two types (elastic or inelastic) based on the rapidity¹ (y) or the pseudorapidity (η) distributions of the product. In an elastic scattering ($p + p \rightarrow p + p$), both protons emerge intact and no other particles are produced. The outgoing protons change direction but still appear in the forward² region as shown by the dots in top right of Fig. 2.2.

In Fig. 2.2, the $p + p$ interactions with different scattering schemes and the final state of their corresponding interactions illustrated with ϕ vs η distributions are shown side by side for more clarity. In all these interactions the particle exchanged is a glueball structure called Pomeron (\mathbb{P}). The pomeron is a special case of reggeon. This is a concept coming from the Regge theory which was developed before QCD to explain the $p + p$ collisions. In QCD, the Pomeron is regarded as a colorless and flavorless multiple gluon state or a glueball exchange [20]. The LHC cross-section (at $\sqrt{s} = 14$ TeV) for elastic scattering is estimated to be ~ 30 mb [19]. The exchange of gluons can excite a hadron. This can result in the outgoing state preserving the internal quantum numbers of the incoming particles but having a higher mass. This is known as quasi-elastic scattering. Interactions where the final state is not identical to the initial state are called inelastic.

Inelastic collisions can be *diffractive* or *non-diffractive (ND)*. There are several possible description of diffraction, allowing several alternative approaches, though the

¹For the definitions of the rapidity and pseudorapidity see the Appendix B.

²Perpendicular to the beam axis the value of pseudorapidity (η) is equal to zero, increasing as the angle of the particle relative to the beam axis decreases. The ‘forward’ direction refers to the regions of a detector close to the beam axis.

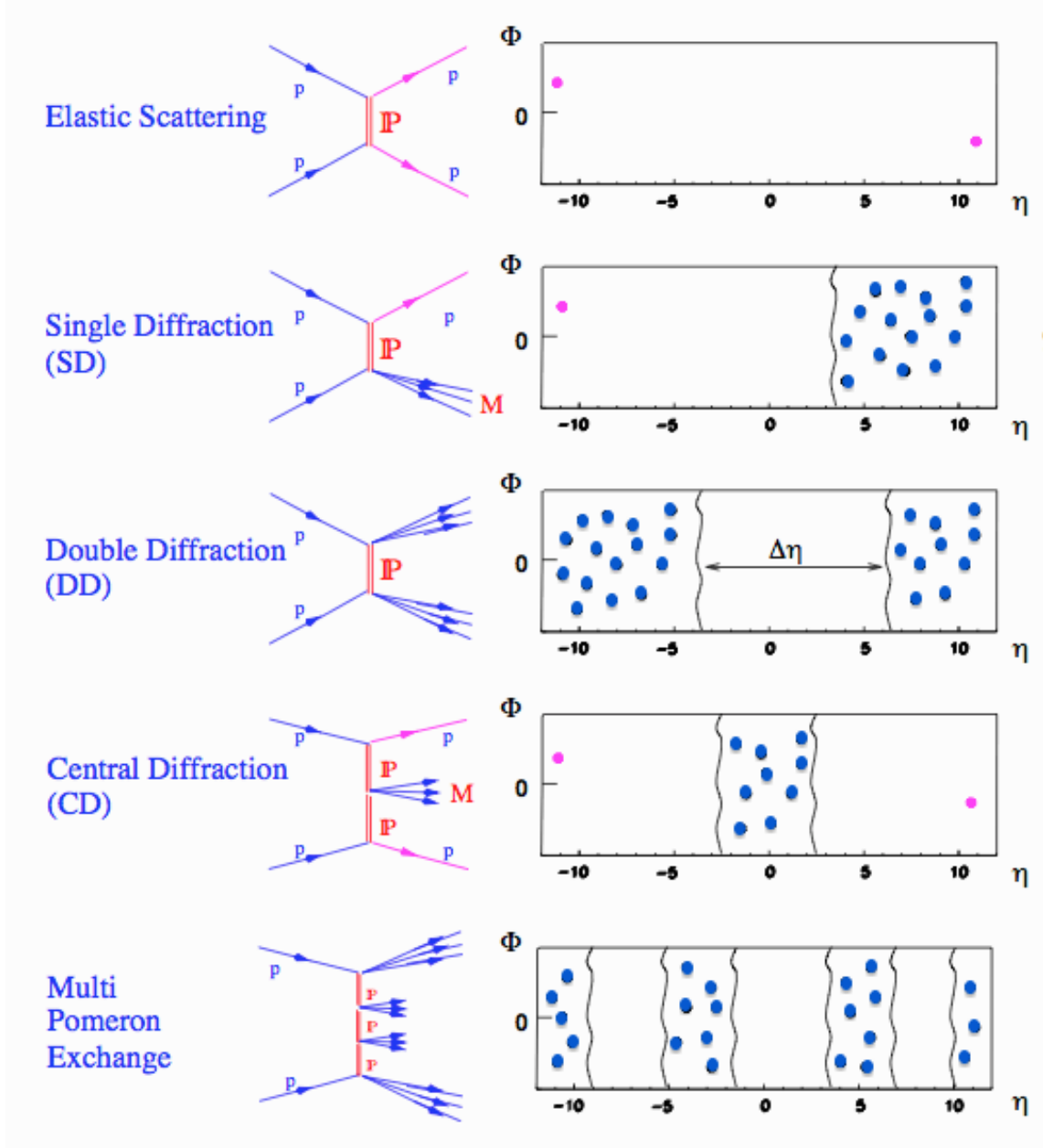


Figure 2.2: *Graphical Representation of the most common event types in $p + p$ collisions. The left side pictures are the graphical representations of the processes and right side pictures depicts their azimuthal distributions as a function of pseudorapidity in the final state of scattering.*

one which is more reliable and got more acceptance is the one described by the Regge theory [21] in terms of the exchange of a Pomeron. A diffractive reaction is one in which no internal quantum numbers (e.g. color or charge) are exchanged between the colliding particles. Diffraction occurs when the exchanged Pomeron interacts with the proton to produce a system of particles referred to as the diffractive system ('M' and also by the blue lines and blue dots as illustrated in Fig. 2.2). In diffractive scattering, the energy transfer between two interacting protons remains small, but one or both protons dissociate into multi-particle final states with the same internal quantum numbers of the colliding protons. The scheme of various diffractive processes as shown in Fig. 2.2 is as follows:

- If only one of the proton dissociates then the interaction is *Single Diffractive (SD)* ($p + p \rightarrow p + M$ or $p + p \rightarrow M + p$). The dissociated proton forms the diffractive system (M) and is depicted as spray of blue lines (dots). The non-dissociated proton is shown as the pink dot. The LHC cross-section (at $\sqrt{s} = 14$ TeV) for SD on both sides is estimated to be ~ 10 mb [19].
- If both the colliding protons dissociate, then the process is *Double Diffractive (DD)* ($p + p \rightarrow M + M$) as illustrated in Fig. 2.2 by the spray of blue arrows (dots) in the final state. These two diffractive systems populate the forward regions, leaving a central unpopulated region in the pseudorapidity. The LHC cross-section (at $\sqrt{s} = 14$ TeV) for DD is estimated to be ~ 7 mb [19].
- A different topology is also possible with the exchange of two Pomerons leading to the *Central Diffraction (CD)* processes ($p + p \rightarrow p + M + p$). In this process, both the protons are intact and are seen in the final state (as two dots in Fig. 2.2), besides having a spray of particles in the central region of the pseudorapidity. The LHC cross-section (at $\sqrt{s} = 14$ TeV) for CD is estimated to be ~ 1 mb [19].

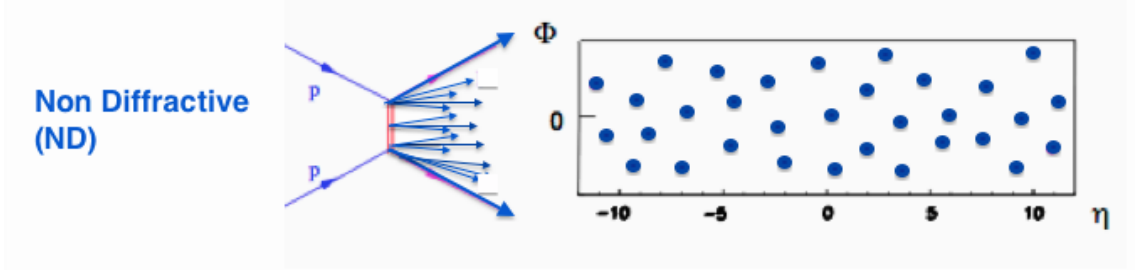


Figure 2.3: *Graphical Representation of the Non-Diffractive (ND) process in $p + p$ collisions. The left side represents the graphical picture of the process and right side depict the azimuthal distribution as a function of pseudorapidity in the final state of scattering.*

- In addition, there are interactions where many Pomerons are exchanged. In this process of *Multi Pomeron Exchange*, the particles are produced with the dissociation of both the protons, here particles are spread over the entire pseudorapidity region with symmetric gap in between as shown in Fig. 2.2. The LHC cross-section (at $\sqrt{s} = 14$ TeV) for multi-Pomeron exchange is estimated to be $\ll 1$ mb [19].
- Finally, in the *Non Diffractive (ND)* interactions there is an exchange of color charge and subsequently more hadrons are produced. This is shown in Fig. 2.3. These are the dominant processes in the $p + p$ interactions and are expected to be $\sim 58\%$ of all interactions at LHC with a cross-section estimated to be ~ 65 mb (at $\sqrt{s} = 14$ TeV) [19]. It is worth mentioning here that, the STAR experiment records the *Non Single Diffractive (NSD)* scatterings which involves the combination of ND and DD scattering processes.

Diffractive processes are characterized by a large (non exponentially suppressed) pseudorapidity gap in the final state. In other words, there is a large phase space separation between the outgoing proton and the diffractive system (or between the two diffractive systems in the case DD) in which no particles are detected. The probability density of a pseudorapidity gap $\Delta\eta$ is given by $e^{-\Delta\eta \frac{dN}{d\eta}}$, where $\frac{dN}{d\eta}$ is

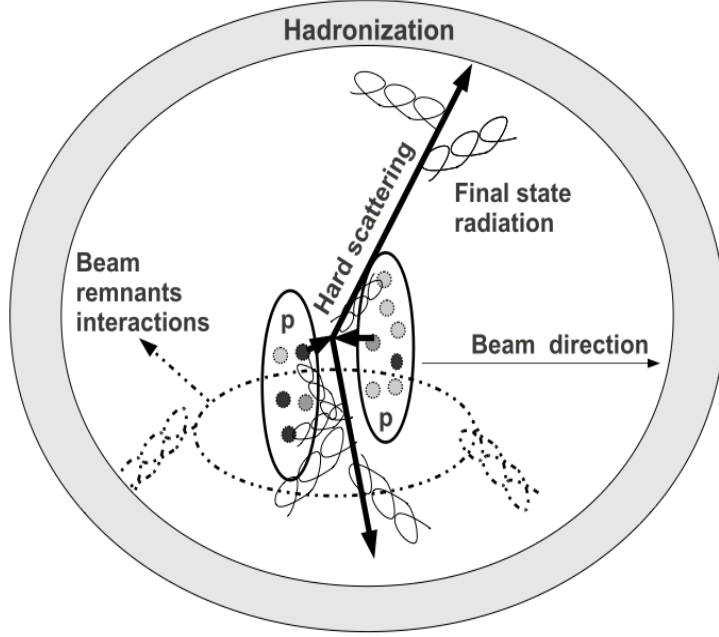


Figure 2.4: *Schematic view of the non-diffractive $p + p$ interaction.*

the pseudorapidity density. Those with $\Delta\eta > 3$ are mainly diffractive events. To summarize, the total $p + p$ cross-section is given by:

$$\sigma_{total} = \sigma_{elastic} + \sigma_{inelastic}, \quad (2.1)$$

where the inelastic cross-section can be further sub-divided into different types like single diffractive (SD), double diffractive (DD) and non-diffractive (ND), i.e.,

$$\sigma_{inelastic} = \sigma_{SD} + \sigma_{DD} + \sigma_{ND} + \dots, \quad (2.2)$$

the additional terms come from less common processes like central diffraction (CD) and multi-Pomeron exchange [22].

The ND collisions are the most complex. The schematic picture of the ND interactions is shown in Fig. 2.4, it can be further divided and well understood in terms of the following stages:

- initial state showers of partons inside the protons,
- hard collisions between two partons (due to high $|Q^2|$), involving the exchange of quantum numbers (this can happen more than once),
- radiations of partons in the hard collisions (parton showers),
- interaction of remnants of incoming protons (partons which do not take part in hard scattering),
- hadronization of all partons produced during the previous steps.

It is also significant to note that, the production of pions, kaons, protons and antiprotons is a part of the hadronization, which can be described using different approaches : independent hadronization, Lund String fragmentation and a cluster model. The production of hadrons with the large p_T with respect to proton beam axis is influenced by the final state radiation of partons produced in hard scattering and are described by fragmentation functions based on the perturbative calculations [23], whereas the production of the low p_T is influenced by the particle production in multiple interactions of beam remnants and soft products of parton showers. That is why the experiments have to provide the good quality measurements to constrain this part of the QCD.

2.3.2 Monte Carlo event generators

The Monte Carlo (MC)³ technique uses random numbers to solve problems. In a definition given by Halton [25], “the Monte Carlo method represents the solution of a problem as a parameter of a hypothetical population, using a random sequence of numbers to construct a sample of the population, from which statistical estimates of

³The term Monte Carlo was coined in the 1940s by physicists working on the Manhattan project in the Los Alamos National Laboratory [24].

the parameter can be obtained”. One of the main applications of MC calculations in high-energy physics is the integration of the relativistic phase space of multi-particle reactions.

Event generators produce hypothetical events in a simulated world with distributions predicted by theory to resemble real collisions. The objective is to provide, as accurately as possible, a representation of event properties in a wide range of reactions. Event generators in particle physics simulate particle collisions as they would be seen by a perfect detector. They are limited by our current understanding of the underlying physics and generally make use of both perturbative and phenomenological approaches. By understanding how the original physics input is distorted at every stage in the better controlled simulated world, event generators help us to understand the detector, trigger, data and background in the real world. Due to the extensive use of MC techniques, they are called the MC event generators. In an event generator the event is built in steps. For example, in a hadron-hadron interaction, the incoming hadrons have a partonic structure given by their *Parton Distribution Function (PDF)*. A collision of partons from the incoming hadrons results in one of many possible processes. The random selection of process is governed by the cross-sections of various processes. The type of process selected determines the next steps. As an example, the following steps occur in a hard process:

- When a collision occurs, the exchange of color and electric charge can result in gluon or electromagnetic bremsstrahlung radiation. Emissions that are associated with the two incoming and colliding partons are called Initial-State Radiation (IsR). These are modelled by space-like parton showers. Those emissions associated with the outgoing partons after the collision are called Final-State Radiation (FsR). These are approximated by time-like parton showers.
- In a collision of two hadrons, there is a possibility that more than one pair of

partons could collide, giving rise to multiple interactions (MI), each associated with its own IsR and FsR. Those partons that do not collide form the beam remnants. While a fraction of energy of the incoming hadrons is taken away by the colliding partons, most of the incoming energy remains in the beam remnants. The beam remnants continue to travel in their original direction, and carry color to compensate for that taken away by the colliding partons.

- With time of the order of fm/c , partons move away from each other and QCD confinement forces begin to act. The time evolution of confinement forces is not known from the first principles, and often, models are used. One such approach is called Lund Model [26], in which confinement fields are modelled as strings that are stretched between each color and its anti-color. As the partons move apart, the potential energy in the string increases, eventually breaking the string and producing a new quark-antiquark pair (or a diquark-antidiquark) at the point of breakage. The two resulting strings continue to fragment until the energy of the string is too small for further fragmentation. The resulting pieces of strings are mesons. Similarly, baryons are formed by diquark-antidiquark pairs being produced at the point of breakage. Baryons (and sometimes mesons) can also be produced by the *popcorn* mechanism [27] from the successive production of several $q\bar{q}$ pairs. While only some of these hadrons live long enough to be visible in a detector, many are unstable and decay at different time scales. The final products seen in a detector depend on their branching ratios, decay products and life-times.

A broad range of physics processes are described by MC event generators. The MC event generators used in this thesis for the comparison of results with the real data are PYTHIA and PHOJET. Both of these models use the Lund String Fragmentation (see Appendix A) for hadronization, the process responsible for the particle

production.

2.3.2.1 PYTHIA

PYTHIA⁴ is a MC event generator frequently used in high-energy physics that combines perturbative QCD and sophisticated, mostly phenomenologically motivated models. It uses perturbative QCD (pQCD) for both low and high regions in transverse momentum. Regions in low transverse momentum play a significant role in inelastic scattering. Perturbative QCD is divergent at low transverse momentum. This is corrected by one of the two methods, either a simple cut-off or a more complex correction factor [28].

It is basically a model of hadronic and lepton-hadron interactions commonly used at RHIC energies and above. It contains “theory and models for a number of physics aspects, including hard and soft interactions, parton distributions, initial and final state parton showers, multiple interactions, fragmentation and decay.” As noted above, for $p + p$ collisions one needs a phenomenological approach to soft interactions in addition to the hard scatterings. PYTHIA solves this issue by using pQCD for all interactions, but by *eikonalizing*⁵ the cross-section and using special methods to treat the divergent low- p_T parts. For a given impact parameter (b), PYTHIA performs multiple parton scatterings according to a Poissonian distribution, with the average number of scatterings being *b-dependent* according to a profile function $A(b)$. Two (main) ways of dealing with the low- p_T divergences within these multiple scatterings are implemented. One, known as simple scenario, is to simply introduce a cut-off parameter p_T^{cut} , such that $d\sigma/dp_T = 0$ for $p_T < p_T^{cut}$. This is the default scenario, with $p_T^{cut} = 1.9$ GeV/c. Another way, the so called complex scenario, is to correct all

⁴PYTHIA is not an abbreviation but a name taken from the ‘oracle’ in the ancient Greek city of Delphi. The heart of PYTHIA is the so-called ‘Lund String Model’.

⁵eikonal is a word borrowed from Gribov-Regge theory, where one studies minijets by assuming that the Pomeron can be split into two contributions, coming from soft and hard processes respectively.

divergent terms by a factor $p_T^4/(p_T^2 + p_{T0}^2)$ and replace p_T^2 by $p_T^2 + p_{T0}^2$ in determining α_s . Here, the p_{T0} is a cut-off parameter as in the first scenario, but the cut-off is continuous rather than abrupt. The first of these scenarios is equivalent to introducing a maximum impact parameter b_{max} above which there are no interactions, while the second assumes some matter distribution around the edges of a hadron. A third option is to turn-off multiple scattering completely, leaving PYTHIA as a simple two-string model. This is described by the authors as a ‘toy model’ only, pointing out the importance of this multiple scattering treatment in the model [29].

After calculating the interactions and treating the initial and final state radiation, PYTHIA performs hadronization using the string picture which is done in by setting the JETSET conditions in the source code, which is part of a complete PYTHIA package. PYTHIA is a very flexible, well documented and tunable model. All aspects of the program are controllable by the user, and the manual documents all options thoroughly. Amongst these options, it offers a parameter for tuning the probability for quark-diquark breakup. The value of this parameter can be used to better reproduce experimental results in $p+p$ collisions, especially for proton transport to midrapidity. In this thesis, in chapter 6, comparisons to PYTHIA are done using the default parameters only, which implies that the simple scenario for multiple scattering is used.

2.3.2.2 PHOJET

PHOJET is another Monte Carlo based event generator much like PYTHIA, except that instead of pQCD it uses the Gribov-Regge phenomenology and calculations briefly discussed above. It is intended to be used for simulations of hadronic multi particle production at high energies in hadron-hadron, photon-hadron, and photon-photon interactions. The ideas and methods used in PHOJET are based mainly on

the Dual Parton Model (DPM). The DPM is partonic version of the dual resonance model, where the basic observation is that in hadronic interactions through the formation of intermediate states, i.e., resonances, the s-channel and t-channel amplitudes will be equal. This *duality* gives the model its name. The amplitude can be written down as a convergent sum of interactions with varying ' s ' known as Veneziano amplitude, and this, combined with experimental high energy phenomenology, led to the description of such interactions through the exchange of *Pomeron*. The DPM extends the dual resonance models in the sense that it includes partons at the ends of the strings and interprets the hadrons in terms of the parton model [30].

These days, the DPM represents an attempt to give an almost complete description of hadronic interactions at high energies. It combines results obtained within Regge theory and by perturbative as well as non-perturbative QCD expansions with generally accepted arguments of unitarity and duality. Within this model one can calculate both elastic processes (i.e cross-sections) and inelastic processes (i.e. multi particle production) in a consistent way.

In order to combine the DPM treatment of soft processes with the predictive power of perturbative QCD, the PHOJET like PYTHIA, is formulated as two-component model with cross-sections split into a soft and a hard component. On the basis of the optical theorem, which relates the forward scattering amplitude in a reaction to the total cross-section, Regge phenomenology is used to parametrize the total and elastic cross-sections as well as a series of partial inelastic cross-sections. To preserve unitarity, i.e. conservation of probability, PHOJET uses so called 'multiple parton interaction' in one event, treating them through Gribov's Reggeon calculus. Since both soft and hard processes are treated in unified way, multiple soft and hard interactions may be generated in one event. PHOJET simulations of $p + p$ collisions at $\sqrt{s} = 62.4$ GeV, using default parameters, will be presented and compared with the

real data observation in the chapter 6 of this thesis.

2.3.2.3 HIJING

Perturbative QCD predicts jet production from parton scatterings in high energy hadronic interactions. Hard or semi-hard parton scatterings with p_T of a few GeV are expected to dominate high energy heavy ion collisions. The Heavy Ion Jet INteraction Generator (HIJING) [37] was developed by combining the pQCD inspired models of jet production using the Lund model for jet fragmentation. The HIJING model has been developed with special emphasis on the role of mini jets in pp, pA and AA interactions. The model includes multiple mini-jet production with initial and final state radiation. The soft processes in HIJING are guided by Lund FRITOF model and DPM. The hard processes are inspired by the perturbative QCD as implemented in PYTHIA. Binary scattering with Glauber geometry for multiple interactions are used to simulate pA and AA collisions. Two important features of HIJING are jet quenching and nuclear shadowing. Jet quenching is modelled by as assumed energy loss dE/dz of partons traversing the produced dense matter. Shadowing describes the modification of the free nucleon parton density in the nucleus. HIJING simulations of $p + p$ collisions at $\sqrt{s} = 62.4$ GeV, with default parameters, are used to extract the vertex efficiency (one of the corrections) to select the good number of events. This is discussed in detail in the chapter 5.

2.4 Phenomenological Models

In this section, the phenomenological models which describe the particle production in $p + p$ as well as heavy ion collisions are presented.

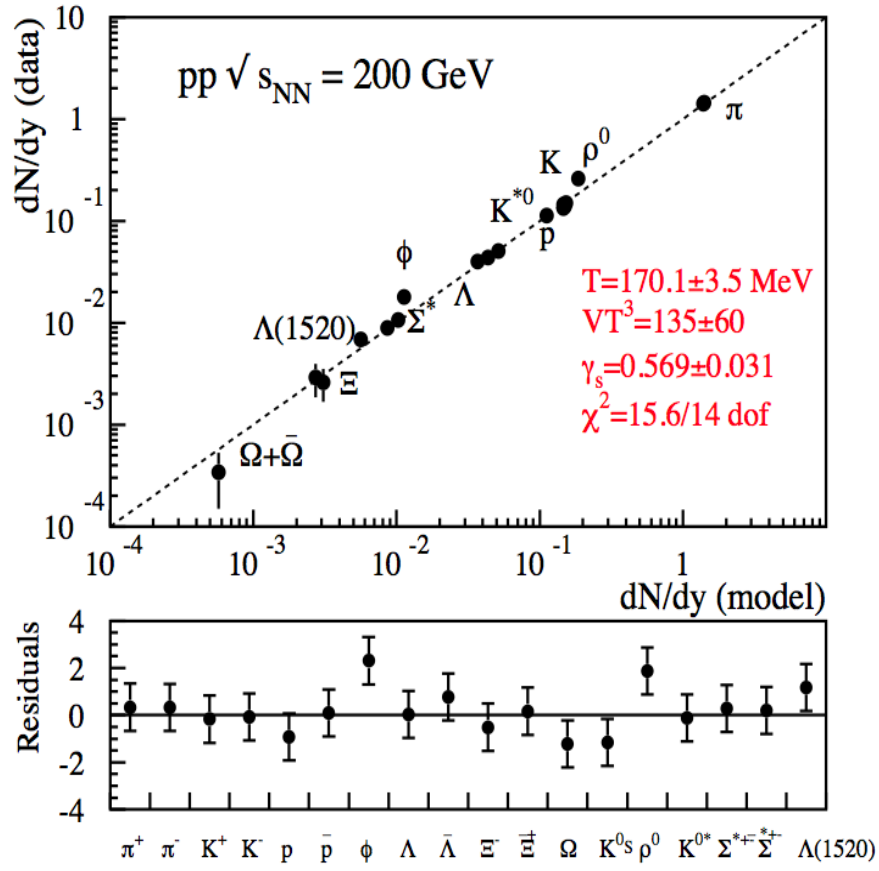


Figure 2.5: *Thermal model fit to the particle productions made by the STAR experiment [31].*

2.4.1 Thermal model

The thermal model describes the total particle production based on the statistical physics in the $p + p$ collisions. This approach assumes that the hadronization takes place from fireballs⁶ according to a canonical ensemble. The quantum numbers of the fireballs are constrained by the initial conditions. In this approach the total yields are described by three parameters: temperature (T), volume (V) and the strangeness suppression factor (γ_s), which is a phenomenological parameter introduced to reduce the phase space for the strange quark production. The volume in this model does not have a clear physical interpretation, unless the yields for the entire phase space are used. Results of the thermal model fit to the yields in $p + p$ collisions at $\sqrt{s} = 200$ GeV reported by the STAR experiment are shown in Fig. 2.5. The description of the yields by the thermal model is in good agreement with data but this does not imply a thermalization on an event-by-event basis, rather suggests that statistical emission is a property of the hadronization process. The obtained $T = 170$ MeV does not strongly depend on the collision energy.

2.4.2 Non-extensive thermodynamic model

For a long time the transverse momentum distributions (p_T spectra) of the particles produced in heavy ion and $p + p$ collisions have been described using the function $dN/dp_T \propto p_T \exp(-p_T/T)$, which is characteristic for an adiabatic expansion of a fireball at temperature (T) [32]. The increase of the energy of colliding protons has shown that this function cannot describe well the high p_T part of the particle spectra, which shows a power-law behavior (e.g. spectra in $p + p$ collisions at $\sqrt{s} = 200$ GeV). The power-law part is interpreted as the region where hard processes are dominant. A function which can describe such spectra in the whole p_T range can be derived

⁶regions of the pre-hadronic strongly interacting matter.

using the idea of the non-extensive thermodynamics (see Fig. 2.6). Non-extensive thermodynamics is based on the Tsallis entropy instead of the Boltzmann-Gibbs (BG) one [33]. In this thesis, the Tsallis distribution has been used to extract the integrated yield per unit rapidity (dN/dy) for the protons and antiprotons. In this fitting function, the free parameters are the dN/dy , q and T , while the mass (m) corresponds to the given hadron mass. The functional form of the Tsallis (Lévy) distribution is given as:

$$\frac{1}{2\pi p_T} \frac{d^2N}{dy dp_T} = \frac{dN}{dy} \times \frac{(q-1)(q-2)}{2\pi qT [qT + m(q-2)]} \times \left(1 + \frac{m_T - m}{qT}\right)^{-q}, \quad (2.3)$$

2.4.3 Collective behavior in $p + p$ collisions

An increase of the energy of $p + p$ collisions provides the possibility to observe collisions with the multiplicity (total number of produced particles) comparable with a multiplicity in heavy ion collisions at lower energies. Those events may exhibit collective behavior of the created system. Here the collective behavior of the system can be understood as a situation in which system is described using quantities like a density or a flow. Already some indications of the collective behavior in $p + p$ collisions are seen at $dN/d\eta > 6$ (multiplicity at mid-rapidity) as hints of the phase transition [34]. The evolution of the mean p_T of identified particles as a function of the multiplicity at mid-rapidity can add additional information. The shape of the spectra can provide evidence for collective behavior and it can be described using a Blast Wave model, which is given below:

Blast wave model : The Blast Wave model describes the shape of the p_T spectra in heavy ion collisions. It assumes a collective radial flow which modifies the thermal emission of the hadrons. The hadron emission takes place during the freeze-out de-

scribed by the freeze-out hyper surface [35]. In this model the shape of the spectra is nicely described by the following equation:

$$\frac{dN}{dp_T} \propto p_T \int_0^R r dr m_T I_0 \left(\frac{p_T \sinh(\rho)}{T_{kin}} \right) K_1 \left(\frac{m_T \cosh(\rho)}{T_{kin}} \right), \quad (2.4)$$

where, $\rho = \tanh^{-1}(\beta)$, I_0 and K_1 are the Bessel functions and β is the radial flow velocity. The radial flow velocity profile is parameterized as :

$$\beta = \beta_s (r/R)^n, \quad (2.5)$$

so that the $\langle \beta \rangle = 2 \beta_s / (n+2)$. The Blast Wave form derived using non-extensive thermodynamics has also been used to fit the p_T spectra [36] and is given by the following equation:

$$\begin{aligned} \frac{dN}{dp_T} \propto p_T m_T \int_{-Y}^Y \cosh(y) dy \int_{-\pi}^{\pi} d\phi \int_0^R r dr \\ \left(1 + \frac{(q-1)}{T} (m_T \cosh(y) \cosh(\rho) - p_T \sinh(\rho) \cos(\phi)) \right)^{\frac{1}{(1-q)}}, \end{aligned} \quad (2.6)$$

2.5 Particle yields and ratios

Matter made its appearance in the universe when *Supergravity* separates into combined nuclear forces (strong, weak, electromagnetic) and gravitation. This era is called Grand Unified Theory or *GUT matter*. The $SU(5)$ is the simplest GUT and it is something upon which the first grand unified theory was based, which is given by the simple relation:

$$SU(5) \supset SU(3) \times SU(2) \times U(1), \quad (2.7)$$

GUT matter is combined of what will become quarks, leptons and photons. Any matter that forms in the early universe quickly collides with other matter or energy and

is converted back into energy. The matter is in equilibrium with surrounding energy and the universe is radiation dominated. Since the temperature of early universe is high, only massive matter can form which are unstable particles [38]. As the universe cools, more stable, less massive particles forms. A weak asymmetry in the direction towards matter becomes evident.

The elimination of anti-matter while leaving behind matter known as baryogenesis [39], is one of the most fundamental problems of modern physics. The Big Bang and cosmological standard model assuming homogeneous and isotropic matter (anti-matter) distribution are conjectured to create matter and antimatter equally. But we experience only protons, neutrons, and electrons in our universe, i.e., the Baryon Asymmetry of the Universe (BAU) seems to be $\sim 100\%$. Exploration of solar systems and observational evidence from radio astronomy along with cosmic ray detection indicate that the Milky Way and other distant galaxies are made of matter. Theoretically, the well known Sakharov's Conditions [40], which have been suggested more than 40 years ago remains a solid framework explaining the circumstances that matter became dominant against anti-matter when universe cools/expands. On the other hand, the standard model for elementary particles apparently presents at least few conditions in order to explain this. The most noteworthy among them is, the anti-particle to particle ratio, which is a measure of this matter to anti-matter asymmetry at a given energy. The ratios for boson and baryons equal to unity implies that this asymmetry has completely vanished, this scenario is observed at very high energies.

2.5.1 Significance of particle spectra and ratios

From the corrected transverse momentum spectra of the charged particles, the important observables like $\langle p_T \rangle$, T_{inv} and dN/dy are obtained and are extrapolated outside of the measured transverse momentum region. The extrapolation is based on different

functional forms which will be discussed in chapter 6. In elementary collisions, particle production models describe a static, thermal source that leads to the exponential behavior of the low momentum spectra. As it was known from the lower energy heavy ion collisions, that the pressure generated during the collision boosts the produced particles away from the center of collision. This mechanism leads to an expanding source, which might be thermalized. This pressure generated boost manifests itself in the change of the shapes of particle spectra, depending on the mass of the measured particle [41].

A universal description for particle and/or antiparticle production at different center of mass energies of nucleon-nucleon (NN) collisions can be achieved by studying the dynamical fluctuations and multiplicities of particle yield ratios [42, 43]. The particle yield ratios are not only able to determine the freeze-out parameters, temperature (T) and chemical potential (μ), but also eliminate to a large extent, the volume fluctuations and the dependence of the freeze-out surface on the initial conditions. On the other hand, the study of particle yield ratios are very much essential for the evaluation of different statistical/thermal models, characterizing the chemical/thermal equilibration and last but not least, these studies help in the search for the unambiguous signals for the creation of the QGP [44].

The investigation of the average transverse momentum as a function of charged hadron multiplicity is a very useful study as the anomalous behavior of the average transverse momentum as a function of the measured charged particle multiplicity can indicate the phase transition from the QGP to the hadronic phase. Following Van Hove's approach: charged particle multiplicity is proportional to the entropy. Thus, the shape of the transverse momentum spectrum carries the combined effect of the temperature in the collision and the expansion of the system. Since, entropy is a quantity characterizing the direction of time in the evolution of a physical system —

in every irreversible process the entropy increases. In elementary interactions, and in particular those involving relativistic collisions of two large atomic nuclei, there is considerable production of particles and hence of entropy. A number of questions arise naturally in this context:

1. When is entropy produced in a quantum process, such as a nuclear collision?
2. How is production of hadronic particles related to production of entropy?
3. How does one measure the entropy produced in the reaction?

In the deconfined phase the color degree of freedom is melted. Therefore, the specific entropy content per baryon (S/B), evaluated at some given (measured) values of statistical parameters, is generally greater in the deconfined state than it is into the confined state. Entropy can only increase, and thus, once an entropy-rich state has formed, there is an opportunity, by measurement of the entropy created in the heavy ion collisions, to determine whether the color bonds of valence quarks present in the collisions have been broken.

The final entropy content of the hadronic particles emerging has to exceed the initial entropy of the thermal state. In fact, quantitative studies show that very little additional entropy is produced during the entire evolution of a fireball, after the initial thermalization stage. For this reason, the final hadronic state conveys the key information about the initial thermal state of dense and hot hadronic matter. For example, in the expanding quark-gluon fireball the quassi-entropy conserving evolution has been confirmed within a model study involving parton cascade [45]. The final-state entropy is largely produced in the first instant of heavy-ion collision. The entropy can be obtained using the momentum distribution function f_{BF} :

$$S_{B,F} = \int d^3x \int \frac{d^3p}{(2\pi)^3} [\pm(1 \pm f_{B,F}) \ln(1 \pm f_{B,F}) - f_{B,F} \ln(f_{B,F})], \quad (2.8)$$

The upper sign $+$ is for bosons (B) and the lower sign $-$ is for fermions (F), which is somewhat counterintuitive, but in fact it is in agreement with Fermi-Bose statistics. We are reminded of this change by the change in the usual sequence of letters ‘F, B’ in the subscript [46].

In heavy ion collisions, the enhanced antiparticles are conjectured as indicators for the formation of deconfined QGP [47, 48], whereas the possible annihilation might suppress such an enhancement [49]. This would explain why the values of antiparticle to particle ratios in $p + p$ collisions are higher than in heavy ion collisions. Therefore, the initial conditions and formation time can be reflected by the surviving antiparticle. Decelerating or even stopping of incident particle (projectile) and its break up in inelastic collisions have been discussed in literature [50]. Therefore, antiparticle to particle ratios can be used to study particle (or antiparticle) transport and production and therefore would have significant cosmological and astrophysical consequences. By mentioning astrophysics, it seems in order now to recall that the $n_{\bar{p}}/n_p$ ratios among others have been calculated and also observed in the cosmic rays revealing essentials details on astrophysical phenomena. Thus, the ratios and their description in the thermal model seem to provide fruitful tools to study the evolution of the matter-antimatter asymmetry with the changing energy.

2.5.1.1 Some Experimental Results

Here, we present some published results reflecting the above discussion pertaining to the transverse momentum spectra and particle ratios. Figure 2.6 shows the combined π^+ , K^+ and p transverse momentum spectra for $p + p$ collisions at $\sqrt{s} = 900$ GeV in ALICE experiment at LHC [51], whereas the transverse momentum spectra of π^\pm along with their antiparticle to particle ratio is shown in Fig. 2.7 for $Au + Au$ collisions at $\sqrt{s_{NN}} = 62.4$ GeV in STAR experiment at RHIC [52]. The spectra

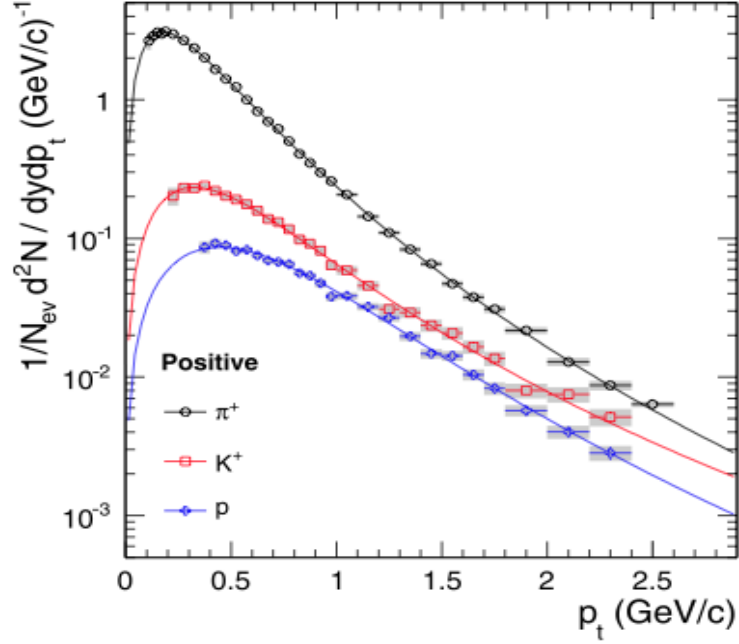


Figure 2.6: (Color online) Transverse momentum spectra of positive hadrons from $p + p$ collisions at $\sqrt{s} = 900$ GeV. The error shown is a systematic plus statistical added in quadrature. The solid curves represent the Lévy function used to extract the meaningful parameters [51].

shown in Fig. 2.6 are fitted with the Lévy (Tsallis) function. This function gives a good description of the spectra and has been used to extract the total yields and the $\langle p_T \rangle$ to form a solid conclusion about the particle production mechanism in a given collision. In addition to this, the results for the transverse momentum spectra of π^\pm , K^\pm , p and \bar{p} as presented in this thesis work can be used to construct the ‘nuclear modification factor’ (R_{AA}) as is shown in Fig. 2.8, wherein they have used the parameterization of the ISR data [53] to obtain the corresponding invariant yields for the $p + p$ collisions. The study of the R_{AA} at the $\sqrt{s} = 62.4$ GeV has been very crucial in understanding the parton energy loss and quark jets in the medium [52].

Strangeness has a special place in heavy ion physics. Enhanced production of strangeness has long been predicted as a prominent signature of QGP formation. In a hadron gas, strangeness has to be produced via strange hadron pairs, which requires

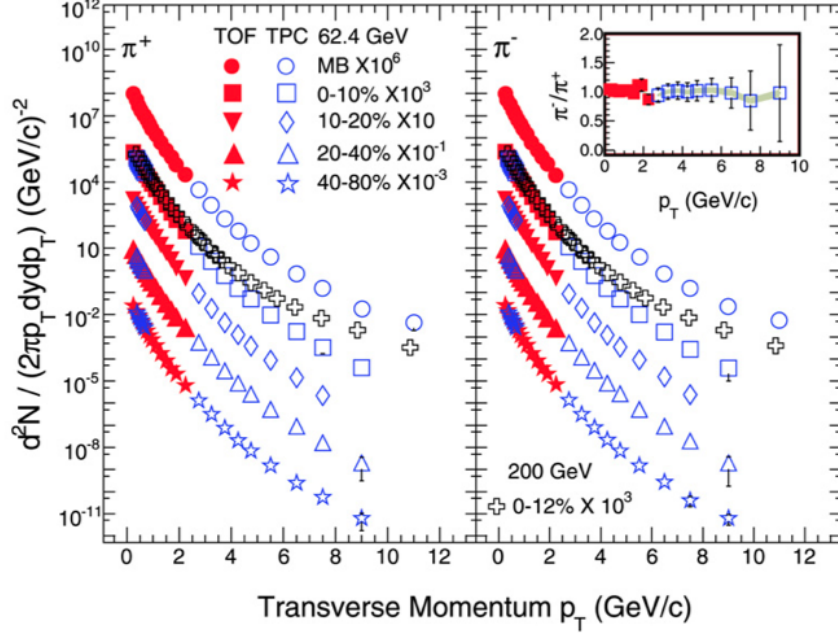


Figure 2.7: (Color online) Transverse momentum spectra of π^\pm from Au + Au collisions at $\sqrt{s_{NN}} = 62.4$ GeV. The π^-/π^+ ratio is also shown in the right panel. The errors shown are statistical, and the shaded bands reflect the systematic errors [52].

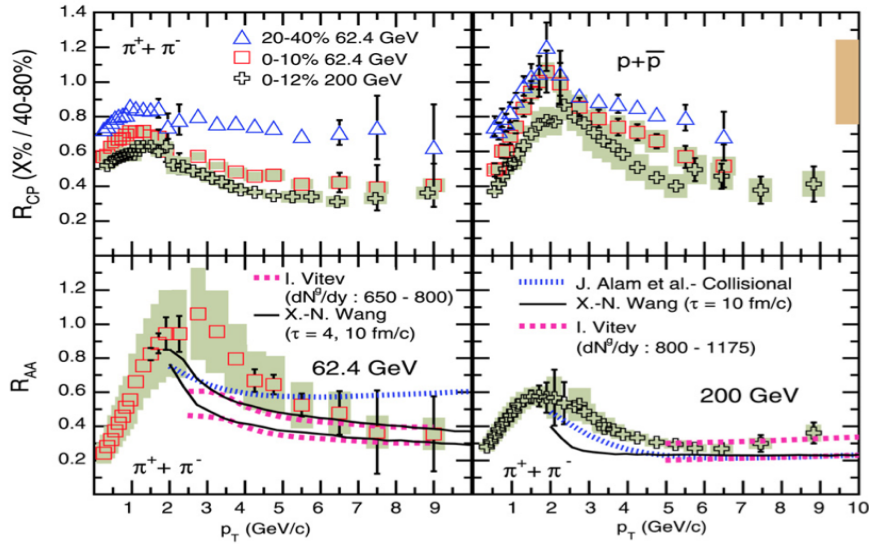


Figure 2.8: (Color online) Upper panels: Centrality and p_T dependance of R_{CP} for $\pi^+ + \pi^-$ and $p + \bar{p}$ for Au + Au at $\sqrt{s_{NN}} = 62.4$ GeV. Lower panels: R_{AA} for $\pi^+ + \pi^-$ at 62.4 GeV (0-10%) and 200 GeV (0-20%) compared to three model predictions. The errors shown are statistical, and the shaded bands reflect the systematic errors [52].

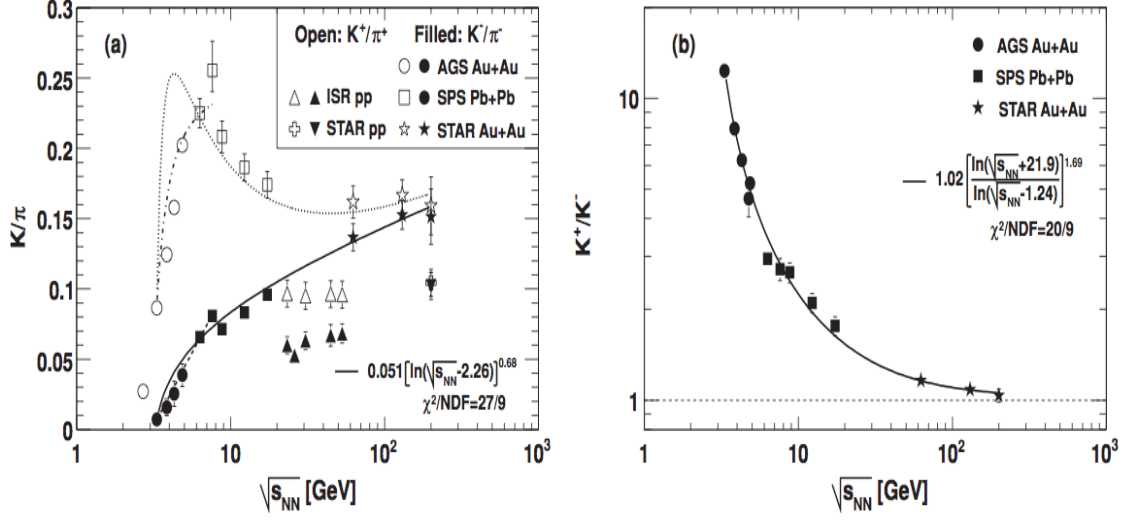


Figure 2.9: (a) K^+/π^+ and K^-/π^- ratios as a function of the collision energy in $p+p$ and central heavy ion collisions. (b) K^+/K^- ratio as a function of the collision energy in the central heavy ion collisions. The curves going through the heavy ion K^-/π^- and K^+/K^- data are phenomenological fits. The curves going through the heavy ion K^+/π^+ data are the product of the fit curves [55].

a large energy; whereas in QGP, it can be produced via strange quark-antiquark pair, which is energetically favored [54].

Figure 2.9 shows the combined results from different experiments at AGS, SPS, ISR and RHIC for the strangeness production and K/π ratio. One obvious feature in Fig. 2.9(a) in heavy ion collisions is that it steadily increases with $\sqrt{s_{NN}}$, while K^+/π^+ ratio sharply increases at low energies. The addition of the K^+/π^+ ratio measurements at RHIC energies clearly demonstrates that this ratio drops at high energies. A maximum K^+/π^+ value is reached at about $\sqrt{s_{NN}} \sim 10$ GeV. This behavior of K^+/π^+ is partially attributed to the net baryon density, which changes significantly with $\sqrt{s_{NN}}$. This could shed light on the two possible production mechanisms for the K : pair production of K and \bar{K} , which is sensitive to $\sqrt{s_{NN}}$, and the associated production of $K(\bar{K})$ with a hyperon (antihyperon), which is sensitive to the baryon (antibaryon) density. The excess of K over \bar{K} is due to the finite net-baryon density.

To visualize the relative contributions from the two mechanisms, Fig. 2.9(b) shows the ratio of K^+/K^- as a function of $\sqrt{s_{NN}}$ in central heavy ion collisions. The ratio sharply drops with energy, demonstrating the transition from associated production of K^+ dominant at low energies to the dominance of equal production of K^+ and K^- via either pair production of K^+K^- or associated production of $K^+(K^-)$ with hyperon (antihyperon) at high energies [55].

Chapter 3

Experimental Facility

3.1 Introduction

The data analysed for the present thesis work is from the Solenoidal Tracker At RHIC (STAR) housed at Brookhaven National Laboratory (BNL) as a part of the Relativistic Heavy-Ion Collider (RHIC) facility. The RHIC Project began in the early 1990s followed by 10 years of development and construction. The first $Au + Au$ collisions at a center of mass energy per nucleon ($\sqrt{s_{NN}}$) = 130 GeV took place in the summer of 2000. The primary physics goals of the RHIC are to produce and investigate the properties of the QGP with heavy ion collisions and to investigate the spin structure of the nucleons with the polarized proton collisions. In this chapter the RHIC experimental facility and the STAR detector are described in detail.

3.2 RHIC Complex

The RHIC experimental facility consists of accelerators, transfer lines, detectors and computational facilities for data storage and analysis. It has the capability to accelerate and collide a large variety of particle configurations such as $d + Au$, $Cu + Cu$,

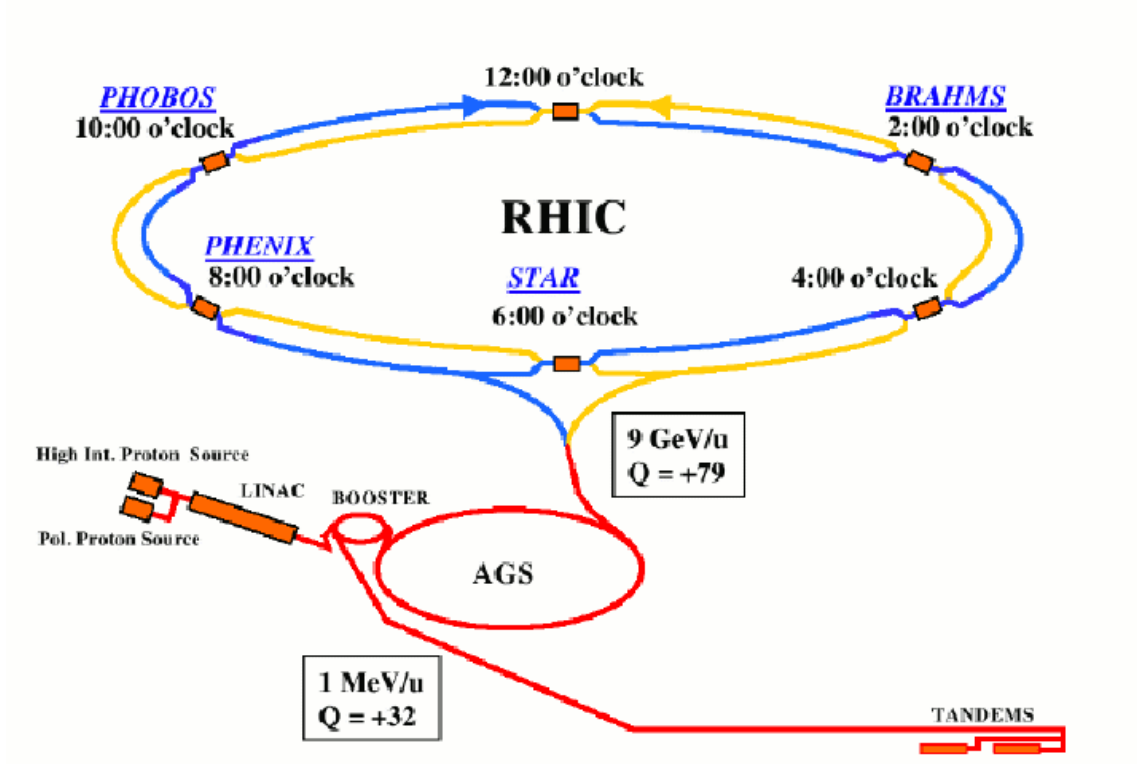


Figure 3.1: *The Relativistic Heavy Ion Collider Complex.*

$Au + Au$, $Cu + Au$, $He + Au$ and $U + U$ at energies ranging from $\sqrt{s_{NN}} = 7$ to 200 GeV for heavy ions and for polarized as well as unpolarized $p + p$ at $\sqrt{s} = 62.4$ to 500 GeV. The schematic diagram of the RHIC accelerator complex is shown Fig. 3.1. The collider has two concentric rings: a “blue” ring for clockwise-beam revolution and a “yellow” ring for counter clockwise-beam revolution and it is also obvious from the the same figure that the rings are not circular, but have six straight sections and six arc sections, and is total 3.8 Km in circumference. There are six intersection points at the center of each straight section and four of them are occupied by the STAR, PHENIX, BRAHMS, and PHOBOS experiments [56]. As of 2014, the BRAHMS, and PHOBOS had already completed their physics programs, while STAR and PHENIX continue to take data.

Figure 3.1 shows the operational steps of accelerating the beams. For Au ion beams, negatively charged ions are produced from a pulsed sputter ion source at the

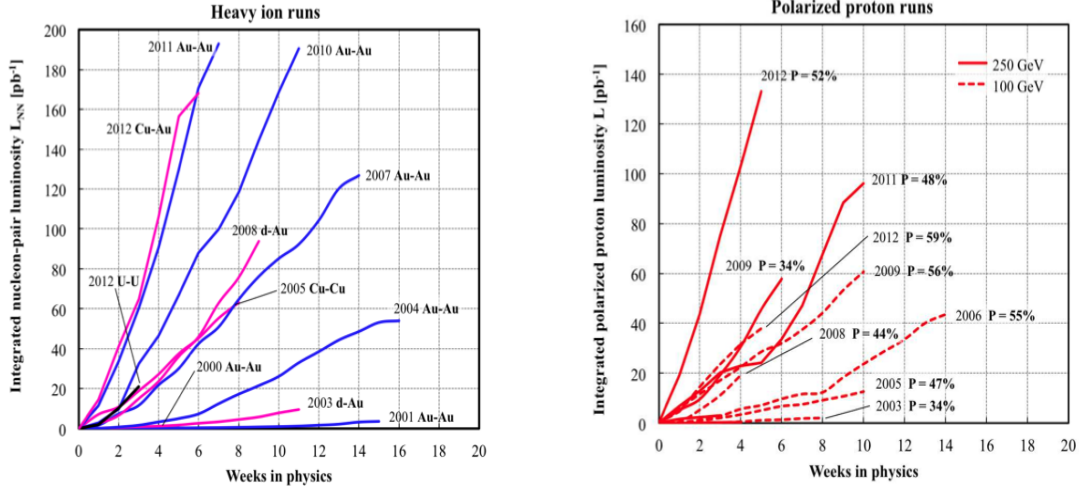


Figure 3.2: *RHIC integrated luminosity for heavy ion and proton-proton collision.*

Tandem Van de Graaff [57], which accelerates the ions to an energy of 1 MeV/A and partially strips their electrons. After passing through another stripping foil and charge selection magnets, the ions with a charge of +32 are delivered to the Booster synchrotron where they are accelerated to the injection energy, 95 MeV/A, of the Alternating Gradient Synchrotron (AGS). For proton beams, polarized protons are sourced at the Linear Accelerator (LINAC) where they are accelerated to the injection energy of AGS. At the entrance and exit of AGS, the ions are fully stripped and reach a charge state of +79. The ions or protons are bunched and accelerated to RHIC injection energy of 10.8 GeV/A before being injected into RHIC via the AGS-to-RHIC Beam Transfer Line (ATR). In RHIC, two counter revolving beams can be accelerated up to the maximum design energy of 100 GeV/A for heavy ions and 250 GeV for protons. For more than 10 years after the first run, the RHIC collider experts have been successfully improving not only luminosities but also the range of the colliding energy with variety of particle species as shown in Fig. 3.2.

RHIC is designed to accelerate heavy ions to nearly the speed of the light in two concentric collider rings. It is worth noting that up to 112 particle bunches per ring

can be injected and in each case the time interval between bunch crossings at the interaction points is of the order of nano second. A summary of the development of heavy-ion collider is given in Table 3.1.

Run (year)	Species	Energy (c.m.s ¹) [GeV/nucleon]	Luminosity
Run1 (2000)	$Au^{79} + Au^{79}$	65.0	$20 \mu b^{-1}$
	$Au^{79} + Au^{79}$	28.0	$<0.001 \mu b^{-1}$
Run2 (2001-2002)	$Au^{79} + Au^{79}$	100.0	$258 \mu b^{-1}$
	$Au^{79} + Au^{79}$	9.8	$0.4 \mu b^{-1}$
	$p + p$	100.0	$1.4 pb^{-1}$
Run3 (2002-2003)	$d + Au^{79}$	100.0	$73 nb^{-1}$
	$p + p$	100.0	$5.5 pb^{-1}$
Run4 (2003-2004)	$Au^{79} + Au^{79}$	100.0	$3.5 nb^{-1}$
	$Au^{79} + Au^{79}$	31.2	$67 \mu b^{-1}$
	$p + p$	100.0	$7.1 pb^{-1}$
Run5 (2004-2005)	$Cu^{29} + Cu^{29}$	100.0	$42.1 nb^{-1}$
	$Cu^{29} + Cu^{29}$	31.2	$1.5 nb^{-1}$
	$p + p$	100.0	$29.5 pb^{-1}$
Run6 (2006)	$p + p$	100.0	$88.6 pb^{-1}$
	$p + p$	31.2	$1.05 pb^{-1}$
Run7 (2007)	$Au^{79} + Au^{79}$	100.0	$7250 \mu b^{-1}$
	$Au^{79} + Au^{79}$	4.6	<i>small</i>
Run8 (2007-2008)	$d + Au^{79}$	100.0	$437 nb^{-1}$
	$p + p$	100.0	$38.4 pb^{-1}$
	$Au^{79} + Au^{79}$	4.6	<i>small</i>
Run9 (2008-2009)	$p + p$	250.0	$110.4 pb^{-1}$
	$p + p$	100.0	$114.0 pb^{-1}$

Run (year)	Species	Energy [GeV/nucleon]	Luminosity
	$pp2pp$	100.0	0.6 nb^{-1}
Run10 (2009-2010)	$Au^{79} + Au^{79}$	100.0	10.3 nb^{-1}
	$Au^{79} + Au^{79}$	31.2	$544.0 \text{ } \mu\text{b}^{-1}$
	$Au^{79} + Au^{79}$	19.5	$206.0 \text{ } \mu\text{b}^{-1}$
	$Au^{79} + Au^{79}$	3.85	$4.23 \text{ } \mu\text{b}^{-1}$
	$Au^{79} + Au^{79}$	5.75	$7.80 \text{ } \mu\text{b}^{-1}$
Run11 (2010-2011)	$p + p$	250.0	166.0 pb^{-1}
	$Au^{79} + Au^{79}$	9.8	$33.2 \text{ } \mu\text{b}^{-1}$
	$Au^{79} + Au^{79}$	100.0	9.79 nb^{-1}
	$Au^{79} + Au^{79}$	13.5	$63.1 \text{ } \mu\text{b}^{-1}$
Run12 (2011-2012)	$p + p$	100.0	74.0 pb^{-1}
	$p + p$	250.0	277.0 pb^{-1}
	$U^{92} + U^{92}$	96.5	$736.0 \text{ } \mu\text{b}^{-1}$
	$Cu^{29} + Au^{79}$	100.0	27.0 nb^{-1}
Run13 (2012-13)	$p + p$	250.0	1.04 fb^{-1}
Run14 (2013-2014)	$Au^{79} + Au^{79}$	7.25	$42.2 \text{ } \mu\text{b}^{-1}$
	$Au^{79} + Au^{79}$	100.0	43.9 nb^{-1}
	$He^2 + Au^{79}$	100.0	134.0 nb^{-1}

Table 3.1: *The Summary of RHIC runs [58].*

RHIC is also capable of accelerating polarized and unpolarized proton beams to a maximum energy of 250 GeV. Besides supplying important baseline information with

respect to $A + A$ collisions, the study of $p + p$ collisions will provide data on the proton spin problem where it has been shown that the valence quarks of the proton do not provide the total spin observed [59]. Collision of asymmetric species, i.e. different species in the two beams ($d + Au$, $Cu + Au$ and $He + Au$), is also possible due to independent rings with independent steering magnets. This diversity allows the study of colliding systems as a function of both energy and system size. As discussed briefly above, that the heavy ions begins their journey in Tandem Van de Graaff accelerator. The ions then travel through a transfer line to the small circular Booster where, with each pass, they are accelerated to higher energy. From the Booster, ions travel to the Alternating Gradient Synchrotron (AGS), which then injects the beams via another beamline into the two rings of RHIC. In RHIC, the beams get a final accelerator “kick up” in energy from powerful, highly focussed radio waves. Once accelerated, the ions can “orbit” inside the rings for hours. RHIC’s 2.4 mile ring has six intersection points where its two rings of accelerating magnets cross, allowing the particle beams to collide. The collisions produce the fleeting signals that, when captured by one of RHIC’s experimental detectors, provide physicists with information about the most fundamental workings of nature [61]. RHIC can also conduct colliding-beam experiments with polarized protons using this accelerator chain.

Furthermore, another important aspect of RHIC is to provide beams of very high luminosities, which makes possible to measure rare processes having small cross sections. For a process with the cross section σ_i , the event rate (R_i) is given by $R_i = \sigma_i \times \mathcal{L}$, where \mathcal{L} is the *Integrated Luminosity* and is given by $\mathcal{L} = fn \frac{N_1 N_2}{A}$, where N_1 and N_2 are the number of particles contained in each bunch, A is the cross-sectional area of the overlap between the two colliding beams of particles, f is the frequency of revolution, and n is the number of bunches per beam. High luminosities can therefore

Parameter	Value
Luminosity (Au + Au)	$2 \times 10^{26} \text{ cm}^{-2} \text{ sec}^{-1}$
Luminosity (p + p)	$1.4 \times 10^{31} \text{ cm}^{-2} \text{ sec}^{-1}$
Beam energy (Au + Au)	3.85→100 GeV/nucleon
Beam energy (proton)	31.2→250 GeV
No. of bunches per ring	60→120
Revolution Frequency	78 KHz
Ions per bunch (Au)	10^9
Ions per bunch (proton)	10^{11}
No. of interaction points	6
Beam life time	~10 hours
Ring circumference	3833.845 m

Table 3.2: *The List of some RHIC design parameters.*

be achieved by maximizing f , n and decreasing the beam profile. A list of some RHIC design parameters is given in the Table 3.2.

3.3 STAR experiment

The STAR experiment was specially constructed to investigate the behavior of strongly interacting matter at high energy density and to search for signatures of QGP information. RHIC creates a nuclear environment of a large number of produced particles (up to approximately one thousand per unit pseudorapidity) and high momentum particles from hard parton-parton scattering. The main motivation to build the STAR was to measure many observables simultaneously to study signatures of a possible QGP phase transition and to understand the space-time evolution of the collision process in ultra- relativistic heavy ion collisions. The goal is to obtain a fundamen-

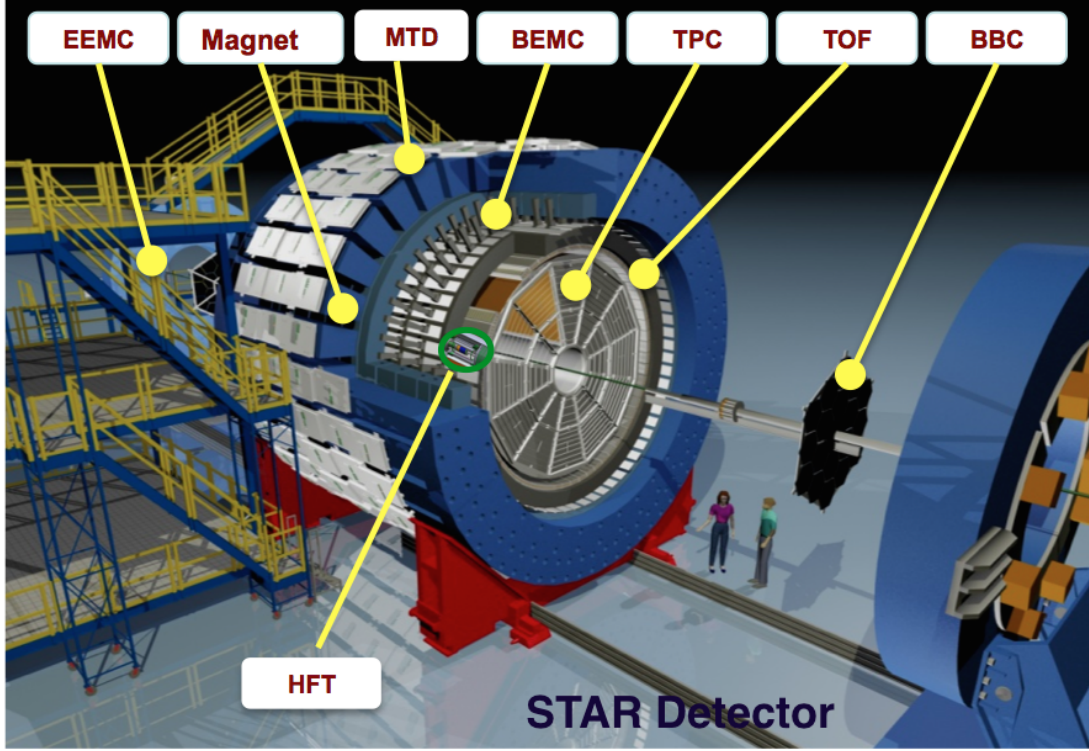


Figure 3.3: *Perspective view of the STAR detector, with a cutaway for viewing inner detector systems [61].*

tal understanding of the microscopic structure of these hadronic interactions at high energy densities. In order to accomplish this, STAR was designed primarily for measurements of hadron production over a large solid angle. STAR is also very effective in high precision tracking, momentum analysis, and particle identification at the central rapidity region. The large acceptance of STAR detector makes it well suited for event-by-event characterizations of heavy ion collisions and for the detection of hadron jets [60].

Figure 3.3 shows the layout of the STAR detector along with its various subsystems. The STAR magnet system is a room temperature solenoidal magnet which was designed in cylindrical shape with a length of 6.85 m and has inner as well as outer diameter of 5.27 m and 7.32 m, respectively. It provides a uniform magnetic field which acts parallels to the beam direction (z direction) with a maximum value 0.5 T.

STAR magnet can work under full field (+0.5 T), reversed full field (-0.5 T) and half field configuration (± 0.25 T).

Being a cylindrical detector, the STAR has an symmetric azimuthal acceptance and it covers large range around mid-rapidity ($|\eta| < 1$, 2π azimuthal coverage). Very close to the beam pipe is the Heavy Flavor Tracker (HFT), it is the latest sub-detector added in the STAR in 2014 experimental run. As its name indicate, the HFT is designed to measure the heavy flavor production by the measurement of displaced vertices and to do the direct topological identification of open charm hadrons. The Time Projection Chamber (TPC) is the main 3D tracker at STAR which has a coverage of $|\eta| < 1$ along with the 2π azimuthal coverage. The Time Of Flight (TOF) detector is surrounding the TPC which also has a similar η and azimuthal coverage. The Barrel Electro-Magnetic Calorimeter (BEMC) located outside of the TOF and covers $|\eta| < 1$ with complete azimuthal symmetry. The Endcap Electro-Magnetic Calorimeter (EEMC) covers for $1 < |\eta| < 2$, over the full azimuthal range. The EMCs are used to distinguish high momentum single photons from photon pairs of π and η meson decays and also electrons from charged hadrons. Outside the BEMC is the magnet system which provides a uniform magnetic field parallel to the beam direction and together with BEMC it also servers as the electron and hadron absorber for the Muon Telescope Detector (MTD). The MTD is also a new added detector, which was installed in 2013 and is operational since then. It is designed to detect high p_T muon for heavy flavor collectivity and production.

Along the beam pipe, there are some trigger detectors: Zero Degree Calorimeter (ZDC), Vertex Position Detector (VPD) and Beam-Beam Counter (BBC). Two ZDCs are located on each side at a distance of ~ 18 m from the interaction point. The ZDCs are designed as hadronic calorimeters to detect the outgoing neutrons. Dipole magnets are put before the ZDC detectors to bend away the charged fragments. The ZDC

signals are used for monitoring the heavy ion beam luminosity and for the experiments triggers. The BBC subsystem covers $3.3 < |\eta| < 5.0$ and consists of two disk shaped scintillating detectors. They are placed at the endcaps of the TPC (3.5 m from TPC center). Each BBC disk is made up of close packed hexagonal scintillator tiles in two rings. A BBC trigger corresponds to a prompt coincidence between at least one (out of eighteen total) tile firing in both BBC EAST and BBC WEST within a time window. This BBC trigger defines a minimum bias trigger corresponding to a pp cross section of ≈ 26 mb, 87% of the pp Non-Singly Diffractive (NSD) cross section. The VPD detector has two assembly which consists of two rings of readout detectors (19 channels). The two assemblies are mounted symmetrically with respect to the center of STAR at a distance of 5.7 m and cover $4.24 < \eta < 5.1$. The signals from VPD are used to select minimum bias collisions, to constrain the location of the primary collision vertex along the beam pipe and to provide start time for STAR fast timing detectors. EMCs is also used to trigger on high p_T particle events.

3.3.1 Trigger detectors

The main trigger detectors are ZDC, BBC, VPD, and EMC. Since the various detector subsystems in STAR have different readout speeds, so the purpose of the STAR trigger is to instruct the slower detectors on when to record data. A schematic view of a nucleus-nucleus collision and STAR trigger system are shown in Fig. 3.4.

The two ZDCs are positioned at ± 18.25 meters along the beam axis relative to $z=0$. The ZDCs are hadronic calorimeters designed to measure the energy from the remaining neutrons from the colliding nuclei after collision in a small solid angle near zero degrees ($\theta < 2$ mrad). The energy deposited by the neutrons can be related to the multiplicity. For a minimum bias trigger, a coincidence between the two ZDCs is required with a summed signal greater than $\approx 40\%$ of a single neutron signal. The

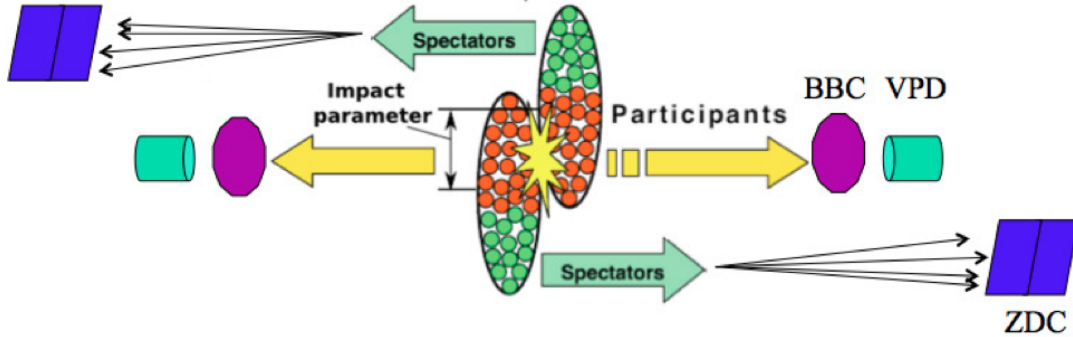


Figure 3.4: (Color online) A schematic view of a nucleus-nucleus collisions and STAR trigger systems.

BBC [62] consists of a hexagonal scintillator array structure, located on each side of the interaction region covering the full azimuth and $2.1 < |\eta| < 5.0$. It is mounted around the beam pipe at a distance of 3.7 m from the interaction point. For a minimum bias trigger, a coincidence of signals is required between two BBC. The timing difference between the two counters is used to get information of the primary vertex position. BBC coincidences are also used to reject beam gas events. In addition, the small tiles of BBC are used to reconstruct the first order event plane for flow analysis [63].

Since 2009, a pair of VPD were used to select events. Each VPD consists of 19 lead converters plus plastic scintillators with photomultiplier tube readout that are positioned very close to the beam pipe on each side of STAR. Each VPD is approximately 5.7 m from the interaction point and covers the pseudo-rapidity range $4.24 < |\eta| < 5.1$. Trigger for the minimum-bias (MB) events using VPD is defined as a coincidence signal in the east and west VPD detectors. The VPD can also provide the information about the Z component of the vertex. The VPD has much better timing resolution than BBC. The EMC can be used to select events with rare probes such as high energy γ and π^0 particles, or electrons from J/ψ decays.

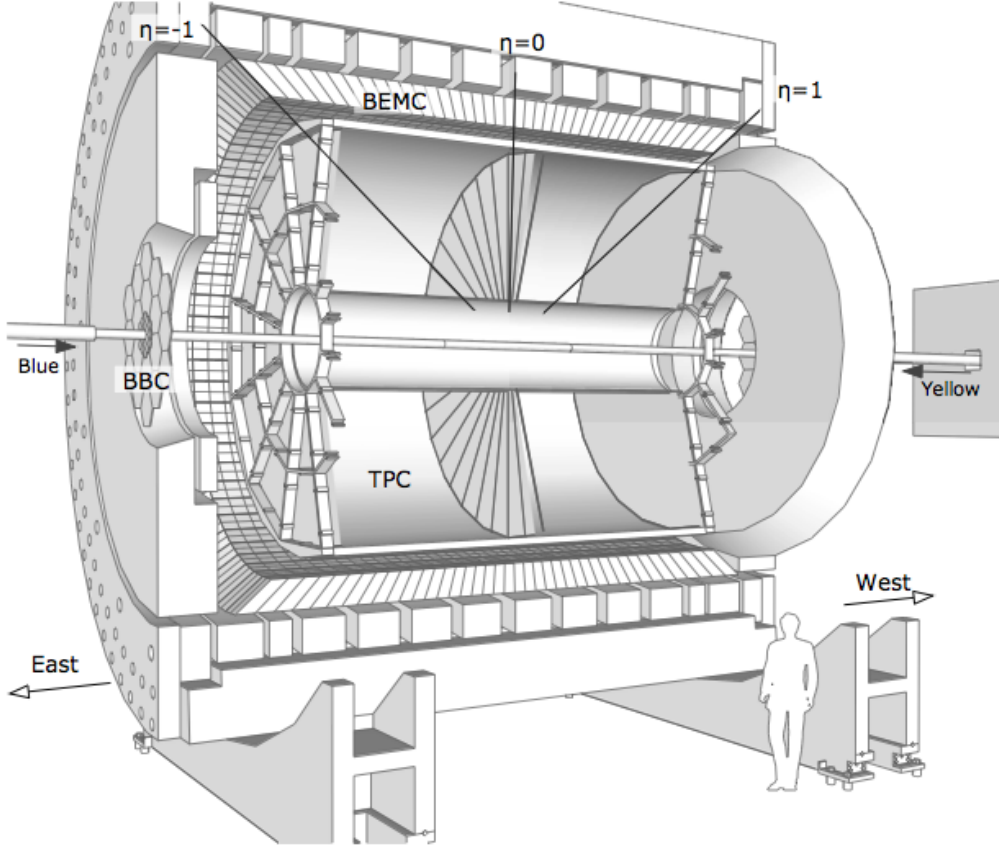


Figure 3.5: *Cutaway view of the TPC along with some other sub-detectors.*

3.3.2 Time Projection Chamber

TPC is the main tracking detector of the STAR experiment and it is designed to provide information on momentum and energy loss of charged particles in heavy ion collisions over a large solid angle in high precision. This large acceptance is very important to study, for example, particle correlations in an event-by-event basis and it also helps to increase statistics for rare processes such as resonances with decay channels with small branching ratios. A schematic picture of the TPC is given in Fig. 3.5.

The STAR TPC is described in terms of the following main features:

3.3.2.1 Physics Objectives:

The STAR's TPC performs the role of 3D camera, capturing the images of the flight of subatomic particles and is used to record the collisions at RHIC. It is the central element in the suite of detectors that surrounds the interaction vertex [67]. The main physics goals for which it is employed are:

- Given the magnetic field, it helps in the measurement of the particle momentum.
- It also helps in the particle identification by measuring the ionization energy loss of the charged particles.
- It also helps in the determining the charge of the particle track.
- It helps in identifying charged particle over the momentum range (0.1 - 1.2 GeV/c), whereas it also helps in the track reconstruction of the charged particles over the momentum range (0.1 - 30 GeV/c).

3.3.2.2 Design & geometry:

The TPC sits in a large solenoidal magnet that produces a maximum of ± 0.5 T magnetic field and it is 4.2 m long and 4 m in diameter. It covers pseudo-rapidity $|\eta| < 1.0$ and 2π azimuthal coverage as is quite obvious from Fig. 3.5 and Fig. 3.6. Important features regarding the TPC's design are cathode & field cage, TPC's endcaps with anodes & pad-planes and drift gas.

The Central-membrane at the centre of TPC serves as “cathode”, the Field Cage is composed of series of equi-potential rings that divide the space between the central membrane and the anode planes into 182 equally spaced segments. One ring at the center is common to both the ends, the central membrane is attached to that ring. It serves two important functions:

- It helps in the gas containment within the cylinder.

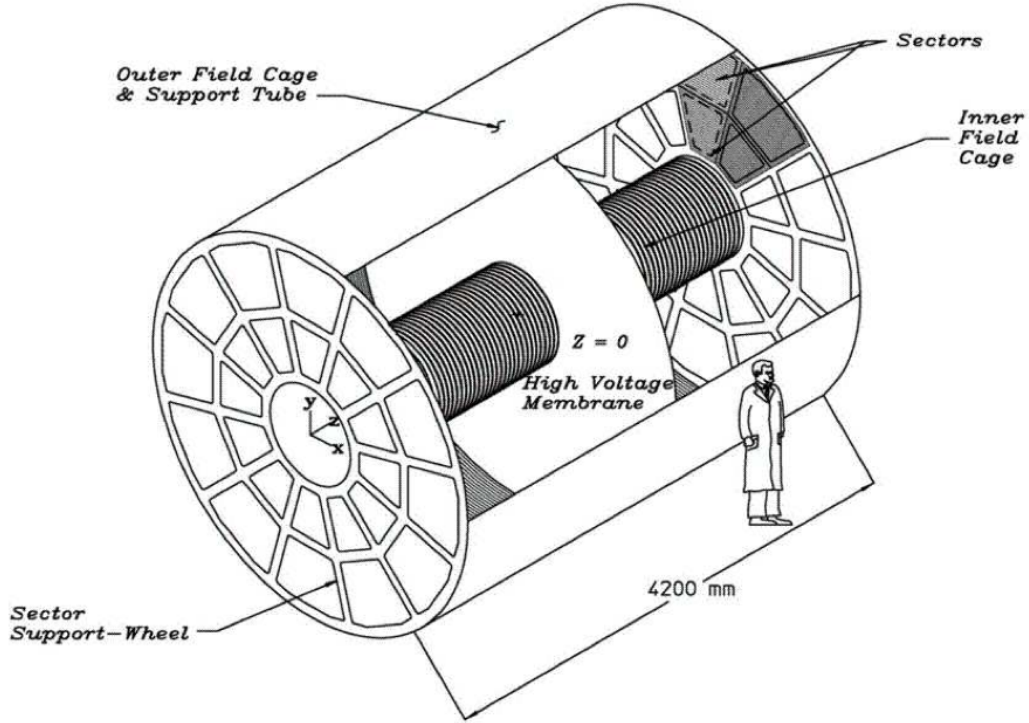


Figure 3.6: *Time Projection Chamber.*

- It helps in maintaining the uniform electric field throughout the drift volume.

At both the ends of TPC, see Fig. 3.6, we have *read-out planes* serving as Multi-Wire Proportional Counters (MWPC) chambers with read-out pads, and these modular units are mounted on the aluminium support wheels as 12-sectors around the circle. Such wheels are aligned on both sides of the central-membrane to form the so called Field Cage as shown in the *read-out planes*. Here each wheel is composed of 12 sectors known as read-out planes and are further sub divided into outer sub-sector & inner sub-sector. The outer sub-sectors use pads with large dimensions as compared to the pads of inner sub-sectors. The significance of outer and inner sub-sectors lies in the fact that:

- The outer sub-sectors have continuous pad coverage to optimize the (dE/dx) resolution.

- The inner sub-sectors are in the region of highest track density and are thus optimized for good two hit resolution; that means they serve to give the better position resolution and lower momentum particles.

Further each MWPC (read-out plane) consists of four planes; three wire planes and one pad plane. They are aligned in the manner as shown in Fig. 3.7. The Wire Plane is comprised of Gating-Grid Plane, Ground Wire Plane and Anode Wire Plane [68], the significance of each of these wire planes are as:

- The Gating-Grid Wire Plane works as a shutter to control the entries of electrons from TPC's drift volume into the MWPC chambers.
- The Ground Wire Plane terminate the fields from penetrating into the avalanche region so that it may provide additional “rf-shielding” for the pads.
- The Anode Wire Plane works as an amplifier and discriminator.

Layout of the one complete sector (which are 12 towards both the ends) is shown in Fig. 3.8.

Gas : The TPC is filled with a P10 gas mixture, that is a mixture of 90% Argon and 10% Methane. Argon (a noble gas) is chosen because it requires low electric field intensities for avalanche formation and has a fast drift velocity. Methane is added to suppress high energy photons caused by excited Argon atoms. The Argon atoms are excited, instead of being ionized, by particles passing by [64]. The pressure of the gas is 2 mbar higher than the atmospheric pressure to prevent contamination by electronegative gas such as H_2O and O_2 , which capture the drifting electrons, reduce drift time, and reduce the efficiency of creating avalanches at read out pads.

Electric Field : A well-defined, uniform, electric field of 135 V/cm along beam

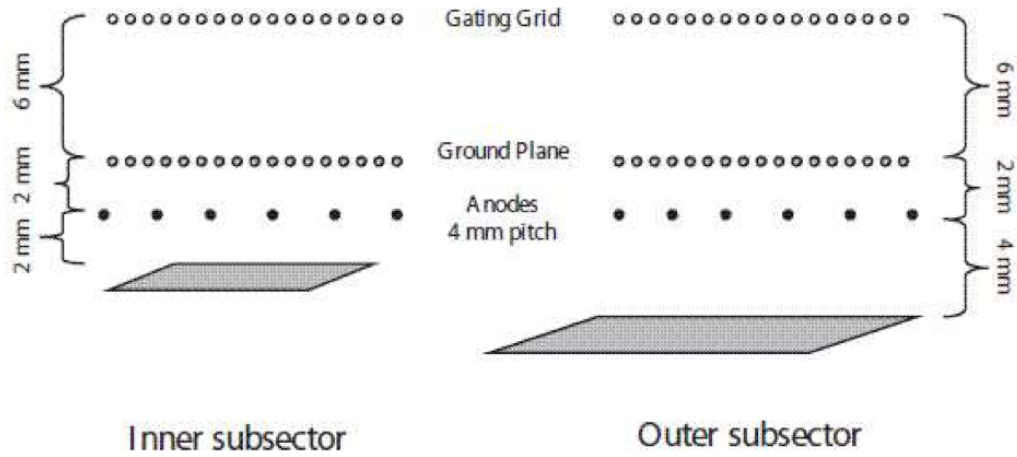


Figure 3.7: *Arrangement of Read-out Chamber in Time Projection Chamber.*

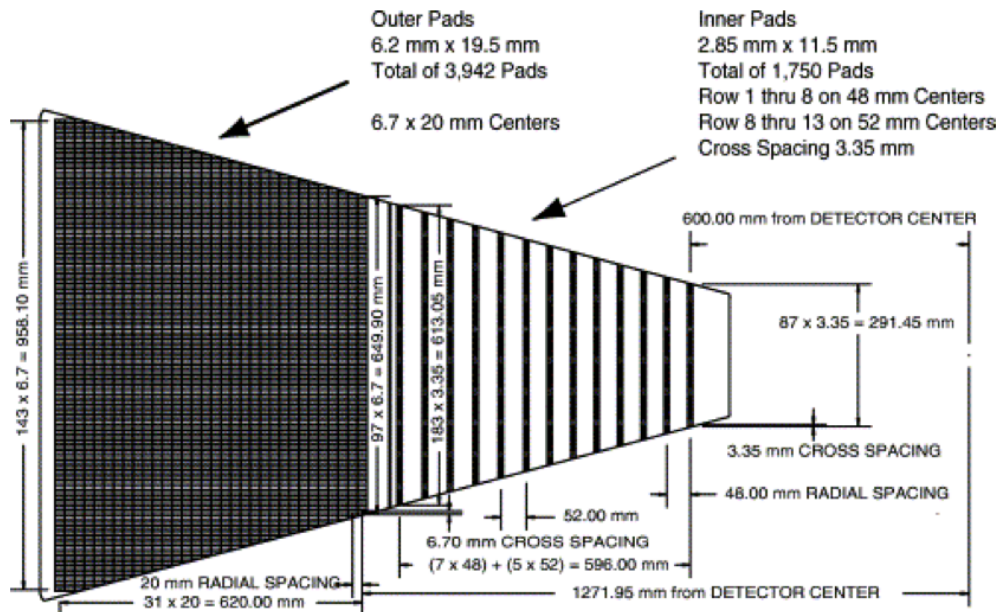


Figure 3.8: *A sector of the TPC anode plane indicating the inner and outer subsectors and their respective padrows.*

axis is applied so that ionized gas particles (electrons) drift into the readout channels on both sides of the TPC. The uniform electric field is created by a thin conductive cathode membrane at the center, concentric inner and outer field-cage cylinders (which are respectively 0.5 m and 2 m from beam axis), and anode wires at the readout end cap.

Read-Out System : The readout system is mounted on aluminum support wheels at both end caps of the TPC. It consists of MWPC chambers and readout pads as is shown in Fig. 3.5 and Fig. 3.6. The drifting electrons avalanche in high electric fields between the shielding grid at ground potential and anode wires. Positive ions created in the avalanche induce image charges on the readout pads. The gating grid prevents the slow positive ions from entering the drift region by closing the gates after electrons have drifted through.

3.3.2.3 Basic Mechanism :

The most important function of the TPC is to reconstruct the paths of particles. When a charged particle passes through the gas, it ionizes the gas molecules and creates electrons and ions. Due to a sufficiently strong electric field, the electrons separate from the ions and drift to the ends of the TPC. The electrons drift with an average velocity of $5.45 \text{ cm}/\mu\text{s}$ to the readout channels (end caps). Different drift distances result in different readout times. With this timing information and the 2D position on the read out pads, 3D tracks can be reconstructed. For this reason, it is called the **Time Projection Chamber**. Since magnetic fields curve a charged particle's path according to its momentum, the momentum can be calculated from the curvature of the path according to following equation,

$$p_T = \frac{e}{c}BR = 0.3BR, \quad (3.1)$$

where B is the strength of a constant magnetic field and R is the radius of curvature. Since particles continuously lose their energy and momentum as they travel through the gas in the TPC, measured momenta are corrected using expected energy loss values, which are functions of a particles velocity. By default, a pion mass is assumed for all particles to estimate velocity. This is a good approximation at high momentum for other species of particles. However, at low momentum the pion mass assumption causes the momentum away from the true value for other species of particles. Though, this problem can be corrected using simulation after particle identification is done.

3.3.2.4 Performance of TPC :

Reconstruction of x, y and z coordinates

The reconstruction of the x,y and z coordinates in TPC employs the principle mechanism of both MWPC & Drift chamber. The x-y position determination is based on the MWPC's principle, while the z position determination is based on the Drift chamber's principle. The x-y coordinates of a cluster are determined by the charge measured on adjacent pads in a single pad row. The z coordinate of a point inside the TPC is determined by the knowledge of time of a drift of a cluster of a secondary electrons from the point of origin to the anodes on the endcaps and average drift velocity [69].

Distortions

The study of distortions is very important because if it is taken for granted, then the spatial as well as momentum resolution will be adversely affected. The position of a secondary electron at the pad plane can be distorted the non-uniformities and global

misalignments in the electric and magnetic fields of the TPC [70]. Various causes of the distortions in the TPC are as follows:

1. Non-uniform magnetic field.
2. The angular offset between electric and magnetic fields.
3. Cathode's non-flat shape and tilt.
4. Geometrical effect between the inner and outer sub-sectors.
5. TPC endcaps non-flat shape and tilt.
6. Misalignments between IFC (Inner Field Cage) and OFC (Outer Field Cage).
7. Space charge build up in the TPC.

Two Hit Resolution & Tracking Efficiency

The two hit resolution and tracking efficiency are also very important features of TPC. The inner and outer sub-sectors have different size pads, so their two hit resolutions are different. Moreover the two hits can be completely resolved when they are separated in the padrow direction by at least 0.8 cm in the inner sector and 1.3 cm in the outer sector. Along the z-direction two hits can be completely resolved when they are separated by 2.7 cm in the inner sector and 3.2 cm in the outer sector. The tracking efficiency of the TPC relies on:

1. Acceptance of the detector.
2. Two hit separation capability.
3. Dead channels and bad pads.
4. Fiducial cuts & merging of the tracks.

Vertex Resolution

To ensure the good tracking the resolution of the primary vertex is very important. The primary vertex is found by considering all the tracks reconstructed in the TPC and then extrapolating them back to the origin. The global average is the vertex position. Also it is calculated by comparing the position of the vertices that are reconstructed using each side of the TPC separately. Furthermore, the primary vertex can be used to improve the momentum resolution of the tracks and the secondary vertices can be separated from the primary vertices if the vertex resolution is good enough.

Momentum Resolution

The transverse momentum p_T of a track is determined by fitting a circle through the x-y coordinates of the vertex and the points along the track. The total momentum is calculated using the radius of curvature and the angle that tracks makes w.r.t. z-axis of TPC, This procedure works for all the primary particles coming from the vertex but for secondary decays, such as Λ s or k_s^0 s, the circle fit must be done without reference to the primary vertex. For the precise momentum resolution, the use of embedding technique is also ensured. As, the momentum resolution at low p_T , significantly depends on determination of the contribution of Multiple Coulomb Scattering (MCS) and that at the high p_T , it is independent of mass and is only limited to the strength of the magnetic field.

Particle Identification

Energy lost by the charged particles inside the TPC volume is a valuable tool for determining the different particle species. But this works well for the low momentum particles and with the increase in the particles energy (momentum), the energy loss become less mass dependent making it hard to separate the particles with velocity greater than 0.7 c. The resolution of good dE/dx requires: large track length, large

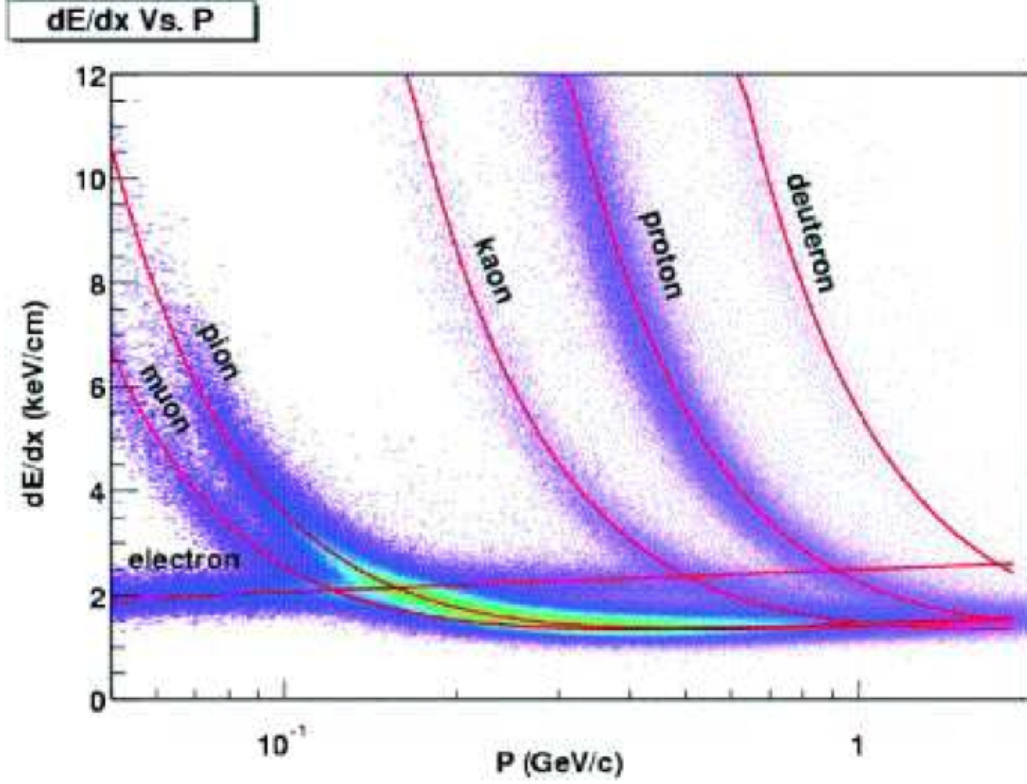


Figure 3.9: *Ionization Energy Loss method.*

number of tracks, good calibration, minimum noise etc.. The most probable energy loss is preferred, but as energy loss is skewed towards the higher values, leading to the Landau's tail so truncated mean is used to characterize the energy loss [71]. As the energy lost by a particle when it travels through the TPC volume is a function of the velocity with which it travels and is described by a Bethe-Bloch formula, the details of which is given in the chapter 4.

The Figure 3.9 shows the measured dE/dx for the particles in the TPC as a function of the particle momentum. Various bands, corresponding to different mass particles, are clearly separated at low p_T . At the modest momentum, the bands start to overlap: e^\pm and K^\pm merge at ~ 0.45 GeV/c, K^\pm and π^\pm merge at ~ 0.75 GeV/c, and p (\bar{p}) and π^\pm merge at ~ 1.2 GeV/c.

Calibration :

Several calibrations have to be done to achieve precise momentum measurement. The main sources of error in the momentum measurement are from changes in the drift velocity and electric and magnetic field distortions [65]. The drift velocity is calibrated using a narrow specific wavelength ($\lambda = 266$ nm) laser which can produce ionization in the TPC equivalent to relativistic particles [66]. Laser events are taken for this purpose in every beam fill. The potential sources of field distortions are field misalignment which arises from slightly unparallel E and B fields, space charge distortion caused by a buildup of positive charged ions in the TPC gas, and grid leak of ionic charge into the main TPC volume from the high gain anode region. Calibrations can be done for those distortions by applying a residual space charge model with parameters. The parameters are determined by minimizing χ^2 values of the helix fit of good quality tracks. Moreover the necessary information regarding the basic parameters along with the associated hardware for the STAR TPC is also given in the Table 3.3.

3.3.3 Time Of Flight

The TOF system was built to improve the PID capability of the STAR experiment and was designed to provide a time resolution less than 100 pico seconds (10^{-9}) to achieve this goal. The heart of this detector is the Multi-gap Resistive Plate Chamber (MRPC) which has been developed at CERN for the detectors at the LHC [74]. The MRPC is based on relatively inexpensive technologies and materials, which enabled the building of the TOF system over a large area within a reasonable budget. After dedicated R&D and remote construction of the TOF detectors [75], about 75% of trays were installed in 2009. The full 120 trays have been installed and taking data since 2010. Since then almost all the analysis in the STAR collaboration have exploited

Item	Dimension	Comment
Length of the TPC	420 cm	Two halves, 210 cm long
Outer Diameter of Drift Volume	400 cm	200 cm radius
Inner Diameter of the Drift Volume the Drift Volume	100 cm	50 cm radius
Distance: Cathode to Ground Plane Ground Plane	209.3 cm	Each side
Cathode	400 cm diameter	At the center of the TPC
Cathode Potential	28 KV	Typical
Drift Gas	P10	10% methane, 90% argon
Pressure	Atmospheric + 2 mbar	Regulated at 2 mbar above Atm. pressure
Drift Velocity	5.45 cm/ μ s	Typical
Number of Anode Sectors Sectors	24	12 per end
Number of Pads	136,608	
Signal to Noise Ratio	20 : 1	
Electronics Shaping Time	180 ns	FWHM
Signal Dynamic Range	10 bits	
Sampling Rate	9.4 MHz	
Sampling Depth	512 time buckets	380 time buckets typical
Magnetic Field	0, ± 0.25 T, ± 0.5 T	Solenoidal
Transverse Diffusion (σ)	$230\mu m/\sqrt{cm}$	140 V/cm & 0.5 T
Longitudinal Diffusion (σ)	$360\mu m/\sqrt{cm}$	140 V/cm

Table 3.3: *Basic Parameters and its associated hardware for the STAR TPC*

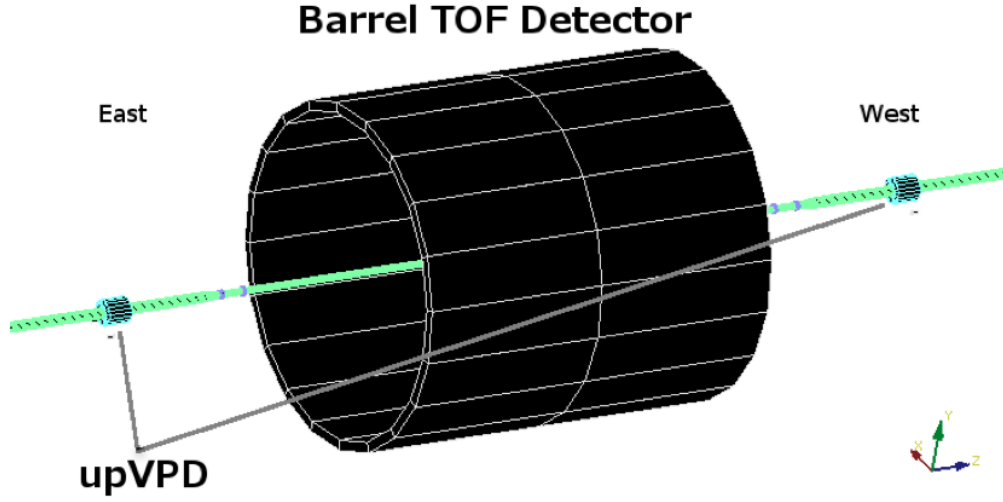


Figure 3.10: *Schematics of the TOF system: Barrel TOF trays and upVPD's upon the beam pipe on the east and west sides .*

TOF information and the TOF system has become an indispensable part of the STAR experiment. The schematic of the TOF detector is shown in Fig. 3.10.

A TOF system measures the time span that particles spend to fly from one point to another. In the STAR experiment the first point is assumed to be the collision vertex. So the TOF information is calculated for only primary tracks, not for global tracks, which might contain secondary tracks, like weakly decaying daughter particles. The collision time (start time) is determined by upgraded Vertex Position Detector (upVPD). The second time measurement is at the stop-side-detectors, barrel TOF trays, which measures the time at which a particle reaches the detector. The TOF has not enough information to provide PID, which will ultimately depend on the particle velocity. Therefore, path length (flight distance) is also required. The path length is estimated by extrapolating the track helix from the TPC onto a channel on the TOF trays, that matched the TOF hit.

As discussed above, the TOF system extends the TPC charged hadron identification capabilities to higher particle momenta. The TPC alone can separate charged

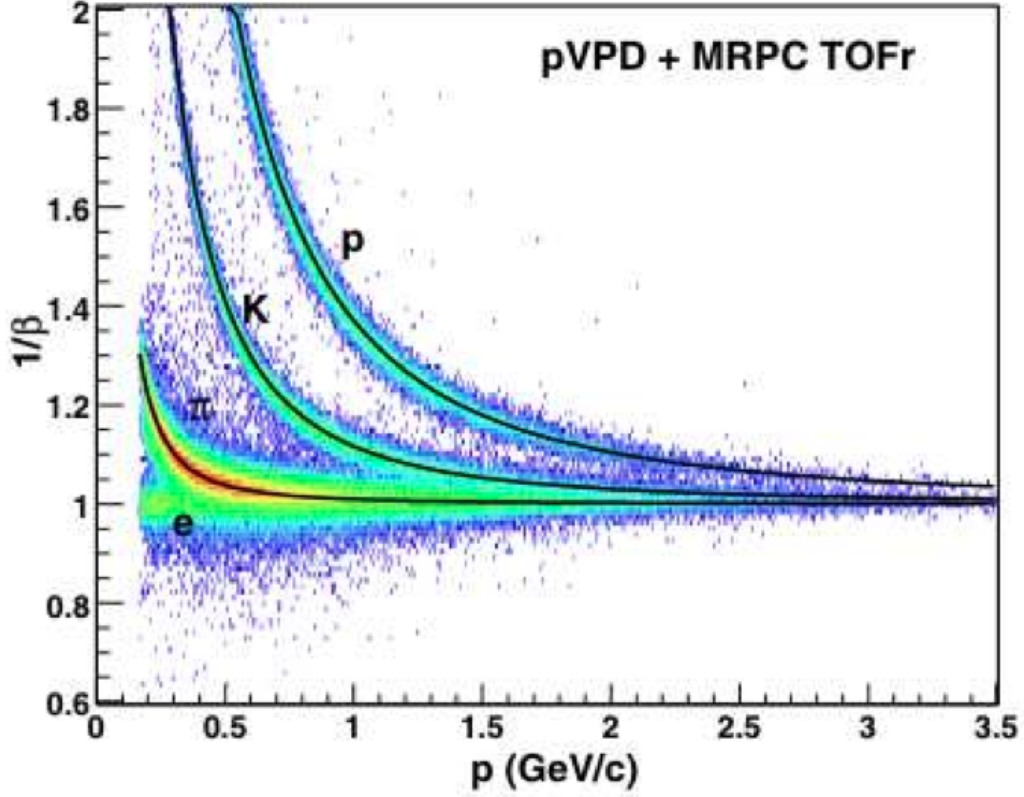


Figure 3.11: *Particle identification using TOF.*

π/K and $(\pi+K)/p$ up to $P \approx 0.7$ and 1.1 GeV/ c respectively, whereas the TOF provide charged hadrons separation for π/K and $(\pi+K)/p$ up to $P \approx 1.6$ and 3.0 GeV/ c respectively. The inverse velocity, $1/\beta$ -distribution as a function of particle momentum is shown in Fig. 3.11. The timing resolution for TOF is $\tau \lesssim 100$ ps. Charged hadron identification can be extended to $2 < P < 4$ GeV/ c using a combination of TPC and TOF detectors. More details about the TOF system can be obtained from this particular STAR Ref. [75, 76]

3.3.4 Barrel Electromagnetic Calorimeter

This analysis relies to some extent on this STAR sub-system called as BEMC for obtaining the MinBias trigger. BEMC sits inside the solenoidal magnet as shown in

Fig.3.3 and it covers the 60 m^2 area just outside the TOF sub-system. It thus has an acceptance and η -coverage congruent to the TPC and TOF-Barrel. It is a lead-scintillator sampling electromagnetic calorimeter with a total depth of 20 radiation lengths ($20X_0$) at $\eta=0$. The BEMC is composed of 120 modules which subtends 6° in $\Delta\phi$ and 1.0 unit in $\Delta\eta$, each module is made of 2 rows of $20\Delta\phi \times \Delta\eta = 0.05 \times 0.05$ towers for a total of 4800 towers covering the full BEMC, the towers are projective to the center of the interaction diamond as shown in Fig. 3.12.

Each module consists of a stack of 20 layers of lead and 21 layers of scintillators with an active depth of 23.5 cm (Fig. 3.13 left). To provide a finer spatial resolution in the towers a Barrel Shower Maximum Detector (BSMD) is implanted at a depth of $\sim 5X_0$ (Fig. 3.13). A two sided aluminum extrusion provides ground channels for two independent planes of proportional wires, each of these layers contain 18000 wires orthogonal to each other to cover the η and ϕ , thus it provides a 2-dimensional image of the showers, the SMD is located near the depth of the maximum electromagnetic showers with energies 1-2 GeV as opposed to hadronic showers which peak at one interaction length [78].

3.3.5 Endcap Electromagnetic Calorimeter

Supplementing the BEMC in the forward region $1 < |\eta| < 2$, the EEMC covers the full azimuth as in STAR's TPC. Just like an BEMC, it also plays a vital role in the detection of the photon, electromagnetic decaying mesons like, π^0 and η in the energy range 10-40 GeV. It also helps in high p_T triggering system in STAR and discriminating pre-shower and post-shower layers intended to discriminate hadrons from electrons. The further details of this specific sub-system can be obtained from this particular Ref. [80].

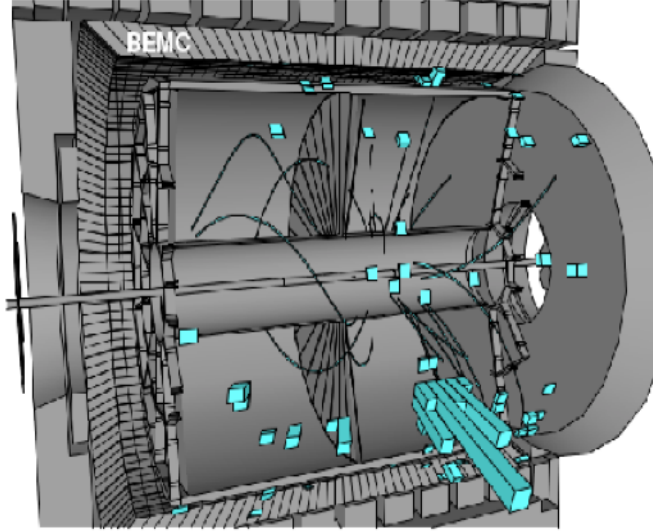


Figure 3.12: *Schematic of STAR's BEMC. The BEMC towers are annotated and their projectivity to the interaction diamond is illustrated by the tilting of towers. Shown in green are energy deposited by tracks coming from the vertex .*

3.3.6 STAR's DAQ

The STAR's Data Acquisition (DAQ) system is driven by the characteristics of STAR's main detectors like TPC, TOF etc.. These detectors produce 80 MB of data per event and are able to read out events at 100 Hz. The storage of raw data is managed by RHIC Computing Facility (RCF) using High Performance Storage System (HPSS), the limit for STAR is 30 MB/s. So the task of DAQ is then to read data from the detectors at rates up to 8000 MB/s to reduce the data rate to 30 MB/s, and to store the data in the HPSS facility. There are many other detectors that need to be read out too, but all with smaller data volumes. Thus, STAR DAQ system is a modular design [79].

The large input data is processed parallel at the DAQ front end. Multiple receiver boards (RB's) receive data in parallel on separate optical fibers from the detectors. The RB's are grouped together in VME crates. Each crate controlled by a Detector

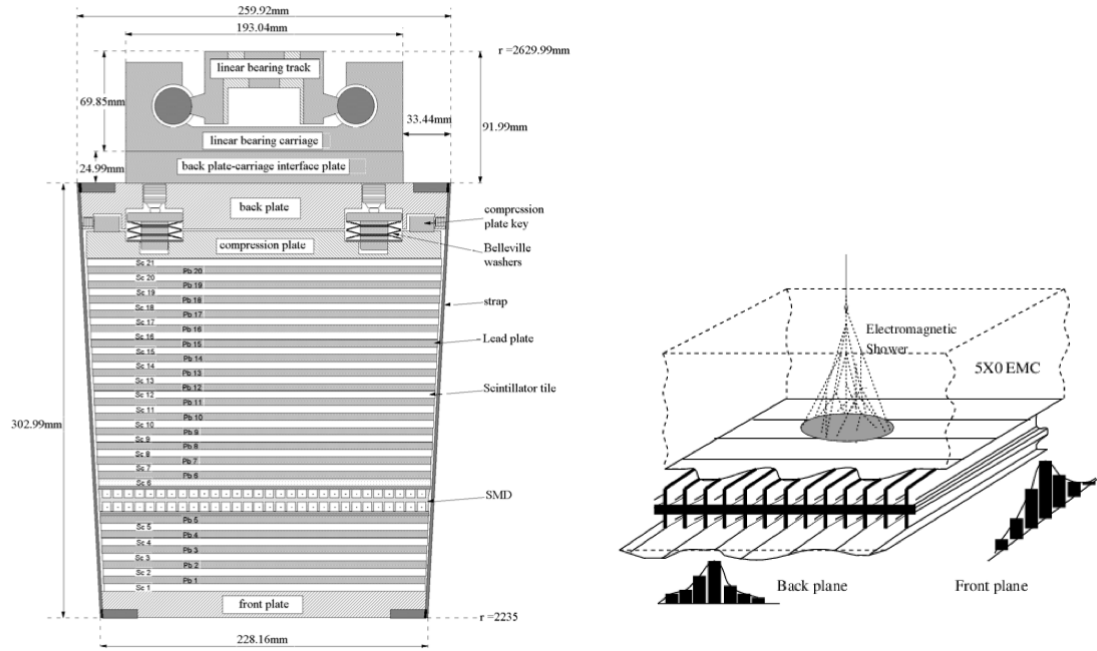


Figure 3.13: (Left) Side view of the BEMC module showing the 20 lead layers and 21 layers of scintillators. Also shown are the two layers of Shower Maximum Detector (BSMD) sitting at a depth of $\sim 5X_0$ from the front face at $\eta=0$. (Right) A schematic illustration of an electromagnetic shower at the BSMD wire layers which provide a two-dimensional image of the shower.

Broker CPU (DET). Two strategies (zero-suppress and 13 for physical filter) are used to reduce the data volume. Events from small detectors are read into MVME processors over private, point-to-point 100 MB/s ethernet. The detector brokers present a detector-independent interface to the DAQ network. After all the events are read into the DETs, the Global Broker (GB) assigns these events to Level 3 Trigger (L3) and wait for an event decision. If the event is rejected, GB instructs the DETs to release the buffers associated with this event. If the event is accepted by L3, the event is transferred to the Event Builder (EVB). The EVB collects and formats all the data, then instructs the DETs to release the buffers associated with the event and passes the event to a Spooler which handles the writing of events to RCF. The Spooler thus transfers the data to RCF. A fraction of the data is written to a event pool for online monitoring too.

3.3.7 Recent Upgrade

Most recently, two new subsystems have been introduced into the STAR detector system, they are MTD and HFT. Installed in the most outside of all subsystems of STAR is the MTD, which is a specifically meant for the μ detection. MTD is based on the long-MRPC technology, it covers $|\eta| < 0.5$ in terms of pseudorapidity and 2π in azimuthal direction. It uses the BEMC and the magnet steel as the absorber for electrons and hadrons. Its first prototype was installed in STAR in the year 2007 and showed good performance in the following runs. In 2013, MTD had been fully installed and tested, however the significant data set was taken with it in the year 2014.

The most recent detector added into the STAR system is the HFT, which has been included in 2014, it is a inner vertex detector and is positioned between Beam pipe and TPC. The HFT is a state-of-art micro-vertex detector utilizing active pixel sensors

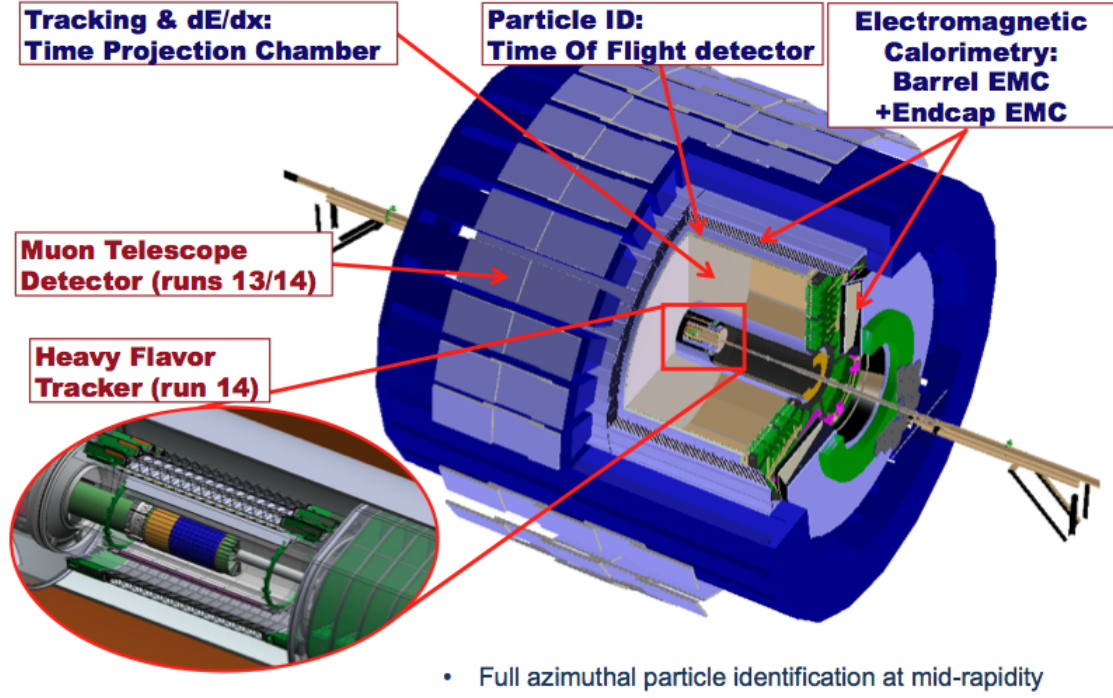


Figure 3.14: *Partial schematic view of the STAR system including the MTD and the HFT [77].*

and silicon strip technology. The HFT consists of 4 layers of silicon detectors grouped into three subsystems with different technologies, guaranteeing increasing resolution when tracking from the TPC towards the vertex of the collision. The Silicon Strip Detector (SSD) is an existing detector in double-sided strip technology. It forms the outermost layer of HFT. The Intermediate Silicon Tracker (IST), consisting of a layer of single-sided strip-pixel detectors, is located inside the SSD. Two layers of silicon Pixel detector (PXL) are inside the IST. The PXL detectors have the resolution necessary for a precision measurement of the displaced vertex. With the HFT, the TOF, the TPC, and the BEMC, the STAR will study the physics of mid-rapidity charm and bottom production. The schematic of the cutaway STAR-detector with some of its main component detectors along with the MTD and the HFT is given in Fig. 3.14.

The primary motivation for the HFT is to extend STAR's capability to study

heavy flavor production in $p + p$, $p + A$ and $A + A$ collisions by the measurement of displaced vertices and the direct topological identification of open charm hadrons. The yield and distribution of bottom hadrons will be estimated from the charm production and non-photonic electron measurements and also via the impact parameter reconstruction of their decay electrons. The primary physics topics to be addressed by the HFT include heavy flavor energy loss, flow, and a test of partonic thermalization at RHIC. These measurements have been identified as necessary goals for the RHIC program in the Nuclear Physics Long Range Plan and in the RHIC mid-term scientific plan [81].

3.4 Event Reconstruction in the TPC

The offline simulation and reconstruction software is a major component of the experiments, as one has to rely on it to reconstruct the collision event to a sufficient extent that the physics goals and the physics capabilities of the sub-detectors can be realized, to evaluate and visualize the results to determine their adequacy as well as correctness, and also to generate acceptance and reconstruction efficiency. The offline software includes all major sub-detectors. The task of the event reconstruction software is to take the digital information from the detectors and convert it into reconstructed track from which the properties of particles emitted from the collision can be extracted. The process of event reconstruction consists of various basic steps viz. hit & cluster finding², track finding³, particle identification and vertex finding⁴.

The primary objective of any reconstruction software is to reduce the data taken in any event to lists of meaningful quantities such as space points, particle tracks,

²Locating the positions in the detectors where a track passed.

³Reconstructing the tracks as sub-collections of hits and clusters which represent that paths of particles emitted from the collision.

⁴Reconstructing the primary vertex from the track collection.

vertices. It must employ the best available knowledge of the relevant calibration parameters for each experimental run. These include for example the drift velocity of the electrons in the gas, trigger time offsets, temperature, pressure, magnetic and electric fields.

The technique employed here is typical of that employed in many other experiments. The offline event reconstruction procedure in the TPC uses the cluster/hit finder as a first step. Corrections to the hits are applied after the finding process. The reconstruction of trajectories is then performed on the basis of the coordinates of the found hits. The specific energy loss of the particle along its path (dE/dx) is calculated from the deposited charges (ADC) of the accepted clusters on the track.

3.4.1 Cluster/Hit Reconstruction

A particle traversing the TPC ionizes molecules of the TPC gas. Electrons released in the ionization process along the particle trajectory knock other electrons out of the gas molecules, so that clouds of electrons (clusters) emerge. Due to the constant electric field, these charged clusters drift towards a segmented readout plane, where they induce a signal on the pads. The cluster coordinate is then derived from the x-y position of the pads and through the clusters drift time, the longitudinal (z) position is obtained.

A pixel is the integer ADC value for a pad in a single time-bin. A cluster gives rise to a signal in consecutive pixels of the adjacent pads. The task of the cluster finder (TCL) is to find groups of pixels and determine the center of gravity of the cluster with respect to the deposited charge [82, 83]. The TPC zero suppressed raw data from the ASIC's on the readout boards contain pixel information and are arranged in a format of potential clusters. The charge information of each pad is corrected for individual gain variations. To find clusters, the following procedure is followed:

In a pixel sequence a center of gravities are determined. Then it is checked whether if in the sequence of a previous pad, center of gravities in the same time-bin range are found. If so, the accruing pixels are marked that they belong to clusters. This procedure is applied in each individual padrow, and results in a list of cluster centroids in pad space-time, where only clusters fulfilling certain quality criteria are accepted.

The hit finder (TPH) is applied to each cluster to reconstruct local peaks. In the case of merged clusters, this can happen if tracks are too close and clusters from these tracks merge into one, clusters are then treated by a “multi-peak finder” algorithm, such kind of scenarios are mostly observed in the $A + A$ (nucleus-nucleus) collisions. Once a peak of a cluster is found, the hit position is extracted. The hit position along the padrow is determined using a 3-point Gaussian fit. The position in time direction is determined by a weight mean of the ADC values. The $x - y$ coordinates are then derived from the geometrical position of the padrow, and the z -coordinate is calculated by multiplying the time-bin position with the constant drift velocity.

3.4.2 Coordinate transformation and distortion corrections

Before track reconstruction, the hit positions are translated from local sector coordinates (sector, row, pad, time) to global coordinates. The x and y coordinates can be calculated using geometrical transformations from the sector coordinates. However, the z coordinate requires knowledge of the drift velocity of the TPC gas mixture with a precision of 0.1%, as well as the offset of the first time-bin [68]. The drift velocity varies due to the dependence on atmospheric pressure and the gas mixture. To minimize this effect, the TPC is operated so that the electric field in the TPC corresponds to the peak in the drift velocity curve [84]. Additionally, a laser calibration is performed before each run. Due to the known position of the laser beams inside the TPC, the drift velocity can be determined by measuring the drift time of clusters

generated by the laser beam.

The offset of the first time-bin is constant over the full TPC volume and can be corrected by reconstructing the event vertex of a given event separately in the two halves of the TPC, and merging the resulting vertex positions. At this level of the reconstruction procedure, differences between reconstructed hit positions and actual positions of the originating clusters caused by distortions are taken into account. Known effects which cause distortions are:

1. $E \times B$ distortions are caused if field lines of the drift field (E-field) are not perpendicular to those of the magnetic field (B-field), due to field inhomogeneities.
2. The non-flat shape and tilt of the central membrane (cathode) and TPC endcaps causes an inhomogeneous drift field.
3. The TPC is placed at a slight angular offset relative to the axis of the magnetic field.
4. Misalignment between the inner and outer field cage causes a shift of hit coordinates.
5. Space charge build up causes a shift of cluster coordinates in the area of high track density (effect is most dominant at the center of the TPC, when dealing the $A + A$ collisions).

The magnitude of the distortions are shown in Table 3.4. Although the distortions are all below 1 mm, they would have an impact on the momentum determination of tracks having high momentum and a large radius (e.g. $r = 33$ m at $p = 5$ GeV/ c). Distortions at the central membrane are most undesirable, since clusters from particle trajectories in this area have a long drift time. In order to understand the distortions and correct for them, the magnetic field of the STAR magnet was mapped out with

Distortion	Magnitude of Imperfection	Magnitude of Correction
Non-uniform B field	± 0.0040 T	0.10 cm
Geometrical effect between inner and outer sub-sectors	Exact calculation depends on geometry	0.05 cm (near padrow 13)
Cathode's non-flat shape and tilt	0.1 cm	0.04 cm
Angular offset between E and B fields	0.2 mr	0.03 cm
TPC endcaps non-flat shape and tilt	0.1 cm	0.03 cm
Misalignment between IFC and OFC	0.1 cm	0.03 cm
Space charge build up in the TPC	$0.001 \text{ C}/\epsilon_0$	0.03 cm

Table 3.4: *Distortion Corrections in STAR TPC [68].*

Hall and Nuclear Magnetic Resonance (NMR) probes before the TPC was installed, while the electric field was calculated taking the geometry of the TPC into account. Since the dependence of the field strength on the coordinates is known, the correct hit position along the padrows can be calculated. The corrections to the hit coordinates are carried out before the track reconstruction and reduce the relative error between a point and the track model fit to $50 \mu\text{m}$, while the absolute error for any point is about $500 \mu\text{m}$. [68]

3.4.3 Track Reconstruction

To reconstruct the trajectories along which charged particles traverse the TPC, hit positions of reconstructed clusters are connected. TPC Tracking (TPT) software uses the follow-your-nose algorithm, which has already been used in experiments such as NA49 at the SPS. It starts by connecting hits in the outermost padrows, where the track density is smallest, to form the track seeds. Using the track seeds, a straight line parametrization is extrapolated inwards. Hits lying along this extrapolation are added to the original seeds and will define a track segment. Once a track segment has been defined, the associated hits are marked as used and new seed is found to form

another track segment. This process is continued until all track segments are found. Attempts are then made to add additional hits to the track segments that were not assigned to the track in the first place, starting with the largest segments. In contrast to the linear extrapolation used in the initial segment formation, a helix track model is used to predict the location of the next hit. Hits on the track are marked as used and added to the collection of points forming the track. The extension of the track segment continues inwards towards the interaction region in the center of the TPC and then outwards, until no further hits can be assigned to the track. The last step in the tracking process is to merge the split tracks.

3.4.3.1 Helix Parameterization

As already discussed above, the trajectory of charged particle in a static uniform magnetic field with $\vec{B}=(0,0,B_z)$ is a helix. To determine the helix parameters of a given track, a circle-line fit is performed in two independent procedures [85]: The transverse momentum associated with the track is obtained by fitting a circle to the collection of assigned hits projected onto the plane perpendicular ($x-y$) to the magnetic field vector as shown in Fig. 3.15(a). A least square fit of the track hits to a straight line in the bend ($s-z$) plane gives the longitudinal momentum along the beam axis, where s is the path length along the track as shown in the Fig. 3.15(b). The circle-line fits are performed within the errors of the reconstructed hits. The helix parameterization in STAR is given by the following:

$$x(s) = x_0 + \frac{1}{\kappa}(\cos(\Phi_0 + h s \kappa \cos \lambda) - \cos \Phi_0), \quad (3.2)$$

$$y(s) = y_0 + \frac{1}{\kappa}(\sin(\Phi_0 + h s \kappa \cos \lambda) - \sin \Phi_0), \quad (3.3)$$

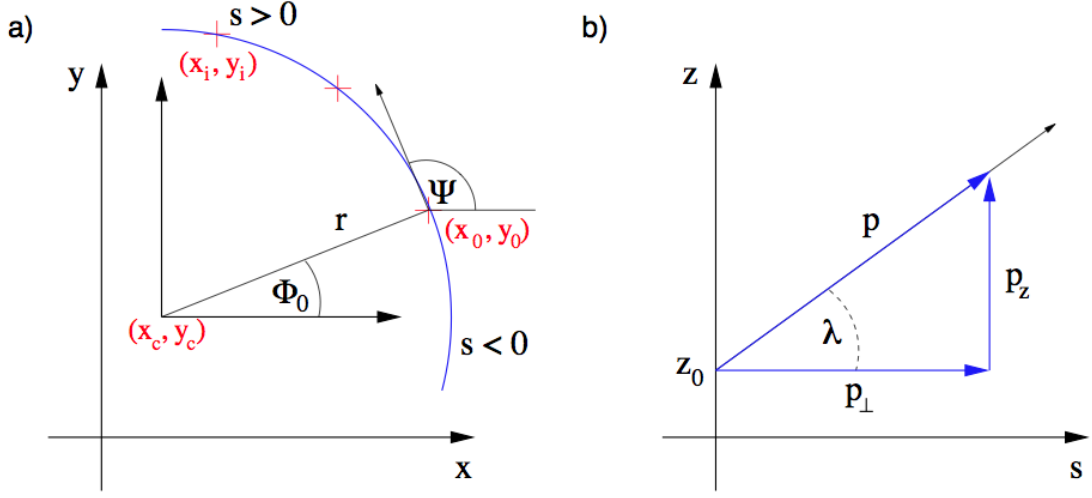


Figure 3.15: a) Projection of a helix onto the transverse (x - y) plane. b) Projection onto the bend (s - z) plane [85].

$$z(s) = z_0 + s \sin \lambda, \quad (3.4)$$

where x , y , z are Cartesian coordinates expressed as functions of the path length s along the helix, (x_0, y_0, z_0) is the origin at $s=s_0=0$, λ is the dip angle, κ is the curvature ($\kappa = 1/r$), q is the particle charge in units of positron charge, h is the direction of rotation of the projected helix in the $x - y$ plane ($h = -(qB) = \pm 1$), Φ_0 is the azimuth angle of the track direction at the origin, i.e. $\tan^{-1}(dy/dx)$ at $s = 0$.

The parameters can be visualized with the aid of Fig 3.15, where in (a), a particle trajectory is projected onto the transverse ($x - y$) plane and appears as a circle. The projection onto the bend (s - z) plane illustrated in (b) shows a linear dependence of the longitudinal component z on the path length s , due to fact that the magnetic field lines are parallel to the particle trajectory in the longitudinal direction. From these parameters, the transverse and longitudinal momentum (p_T , p_z) can be calculated. To calculate the momentum components of the particle trajectory (p_x, p_y, p_z), the helix has to be extrapolated to the origin, where the particle is produced (e.g. the

main event vertex for a primary particle), in order to determine the azimuthal angle (Ψ), of the track direction at that point.

3.4.4 Vertex reconstruction

The vertex of the collision is the point where the two nuclei collide or appear to collide, interaction point of the two nuclei would also be a good phrase to define a vertex. Figure 3.16(a) shows the side-wise view of the STAR's TPC in a high multiplicity $p + p$ event. In the given Fig. 3.16, the counter revolving beams enter from the left and the right through the beam pipe which is represented by the two center-most horizontal lines. The beam pipe can be seen more easily as the innermost circle in the end-wise view shown in Fig. 3.16(b). The color scale of the tracks is based on the magnitude of p_T of the corresponding tracks, with low p_T tracks shown in the blue while orange color is meant for the high p_T tracks. Most of the tracks originate from a point near the center of TPC, this point is called the vertex and is symbolized on the event display as a red star. Tracks that come from the vertex referred to as the *primary tracks* and they corresponds to the required signal. Tracks that do not project to the vertex are background tracks. These background tracks have many sources — pile-up, cosmic rays, and decays of primary tracks.

As it has been observed that in an experiment based on Laboratory System, the position of the vertex must be within the target, whereas in RHIC which has a colliding beams (Center of Mass System), has primary vertices located anywhere along the beamline. If the bunches are not steered or collimated well, the vertex can wander longitudinally. When the vertex is close to the edge of the TPC, many of the tracks will not be reconstructed because they do not fall within the acceptance of the TPC. Therefore, the vertex position must be constrained to near the center of TPC in order to maintain the uniform acceptance. Figure 3.17(a) shows the longitudinal

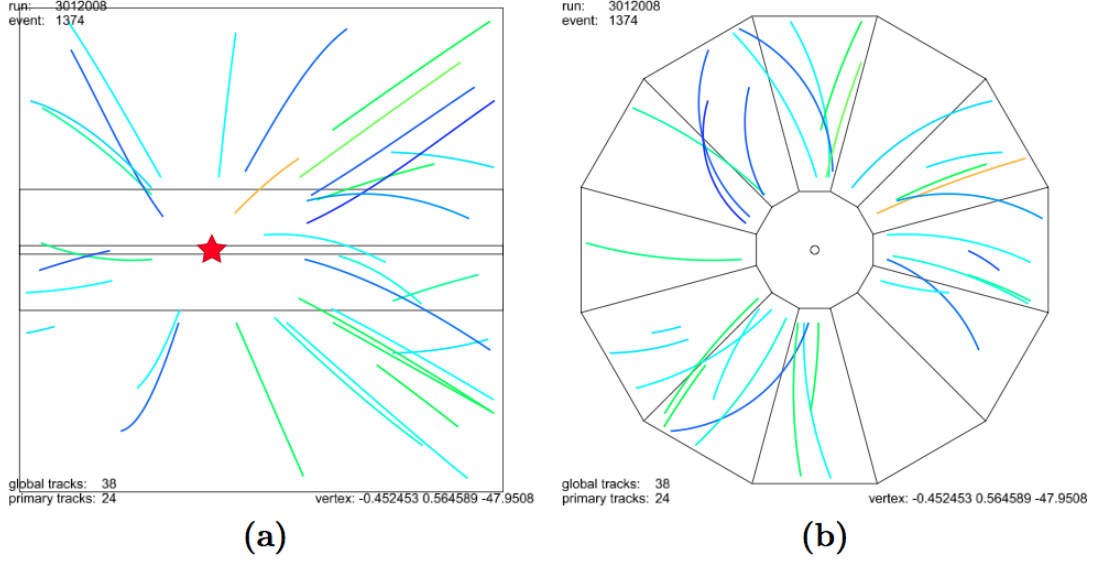


Figure 3.16: a) Side-wise view and, b) End-wise view of the $p + p$ event. The red star symbol represents the vertex position determined by the software [86].

vertex position distribution for the high multiplicity $p + p$ event. The distribution is very wide, therefore many outlier events are required to be rejected. The transverse position distribution is more constrained because it must occur within the beam pipe diameter and does not depend strongly on the bunch timing. The transverse position distribution is shown in the Fig. 3.17(b) [86].

In the standard method of vertex finding, a minimization is performed to find the vertex. Schematically, what is done is to minimize the distance of closest approach of all the tracks in the event. If a track comes from the vertex, one would expect the distance of closest approach (DCA) of a track to the vertex to be zero. An iterative approach is used to remove the outliers in order to find a more precise vertex location. The software package that performs this function is referred to as the *proton-proton Low Multiplicity Vertex (ppLMV)* finder. The quantity to be minimized is given as :

$$\chi^2 = \frac{1}{N} \sum_{i=1}^N \frac{\Delta x_i^2}{\sigma_i^2}, \quad (3.5)$$

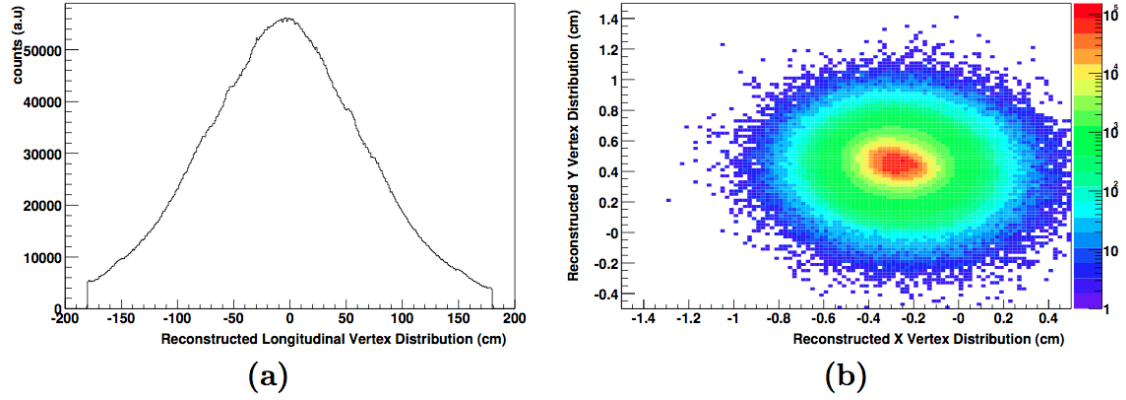


Figure 3.17: *a) Vertex distribution along longitudinal and, b) transverse direction in $p + p$ event [86].*

where Δx_i is the distance of closest approach between the requested vertex and the current track, σ_i is the error on Δx_i and is a function of momentum and other track parameters. The error can also be used as a weighing function to give a larger influence on the vertex for certain high quality tracks. For instance, a high p_T track has a small curvature and undergoes less scattering in comparison to low p_T track. Therefore, the high p_T tracks should have a small error when projecting back to the vertex.

In a $Au + Au$ event there are approximately 5000 tracks per event, so there are sufficient constraints to produce a reliable and accurate fit. However, in a $p + p$ event, because of comparatively fewer tracks per event, so extra constraints must be added to produce a reliable fit. Since the transverse position of the beam is very well confined, as shown in Fig. 3.17(b), so this can be used as a constraint on the vertex position. In order to use this as a constraint, the standard vertex finder is run without restrictions on the transverse position. The transverse position versus the longitudinal position is then parameterized by a fit, which is referred to as the beamline. The vertex finder is then re-run with the beamline added in as a highly weighted track. This effectively constrains the vertex to lie along the beamline. Since the beam steering changes every time RHIC is filled, a beamline parametrization is calculated for every run.

3.5 Particle Identification by dE/dx

As the main tracking detector of the STAR, the TPC can identify particles by measuring the mass dependent ionization energy loss (dE/dx) at low momentum ($P < 1.2$ GeV). A charged particle traversing the TPC gas volume ionizes the gas atoms. In the electric field these charge clouds drift from their creation point to the two ends of the TPC [68], where the charges are readout on the padrows. Produced charge in each hit on a padrow is proportional to the energy loss of particles traversing through the TPC volume. If a particle travels through the entire TPC volume, 45 dE/dx points can be measured on the 45 padrows. This specific ionization energy loss, called the dE/dx , is a function of the particle momentum magnitude. This property is used for particle identification. In this thesis work we shall focus on the low p_T region. While the extension of particle identification to high momentum (P) is possible by the Time of Flight (TOF) patch and by using the relativistic rise of the specific ionization energy loss [74, 75, 76]. The details of the TOF and the relativistic ionization energy loss are out of the scope of this thesis work.

The electron ionization process has large fluctuations, so the measured dE/dx sample for a given track length follows the Landau distribution. But the mean distribution is sensitive to the fluctuations in the tail of the distribution. Therefore, highest 30% of the measured charged clusters are discarded for each track, and the truncated mean from the remaining 70 % of the charged clusters for each track are selected for data analysis.

The resolution of the obtained $\langle dE/dx \rangle$ depends on; the track length and the particle momentum: greater the track length greater will be the number of hits and hence more will be the resolution, while smaller the momentum, more the ionization and thus greater will be the resolution of mean dE/dx . The ionization energy loss by

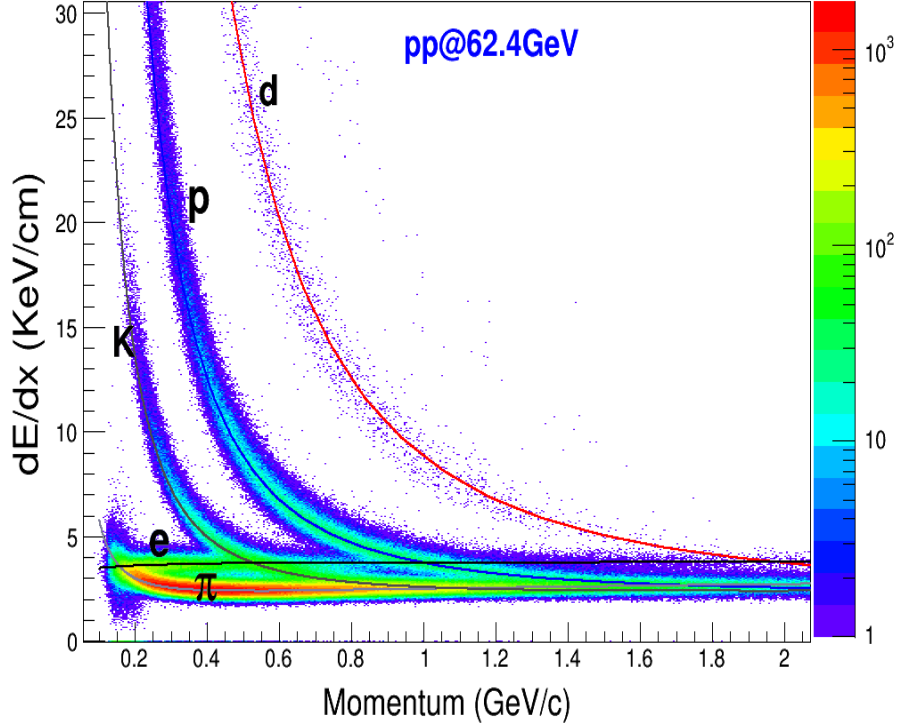


Figure 3.18: *Identification of the particles by Ionization Energy Loss.*

charged particles in material is given by the Bethe-Bloch formula [87] :

$$-\frac{dE}{dx} = 4\pi N_0 r_e^2 m_e c^2 \frac{Z}{A} \rho \frac{1}{\beta^2} z^2 \left[\ln \left(\frac{2m_e c^2}{I} \beta^2 \gamma^2 \right) - \beta^2 - \frac{\delta}{2} \right] \quad (3.6)$$

where N_0 is the Avogadro number, r_e is the classical electron radius, Z is the atomic number (only when used in eq. 3.6) of the medium, I is the ionization potential of the medium and δ accounts for the density effect of the medium. Now, Fig. 3.18 shows the measured $\langle dE/dx \rangle$ versus total momentum for the particles in $|\eta| \leq 0.5$ and gives the distribution of different $\langle dE/dx \rangle$ bands for positive charged particles. Various bands, corresponding to different mass particles, are clearly separated at low momentum. At the modest momentum, the bands start to overlap. However,

particles can still be statistically identified by a fitting procedure to deconvolute the overlapped distribution into several components, this point will be more clear by the various Z -*distribution*⁵ results discussed in Chapter 4. Moreover, the separation of the dE/dx bands depends on the rapidity region and decreases toward higher rapidities. To obtain the maximal separation we only concentrate on the midrapidity region ($|y| < 0.1$) for the present analysis.

⁵A method used in STAR to extract the raw particle yields of charged particles in TPC.

Chapter 4

Analysis Techniques

4.1 Introduction

The offline simulation and reconstruction software is a major component of the experiments, as one has to rely on it to reconstruct the collision event to a sufficient extent that the physics goals and the physics capabilities of the sub-detectors can be realized, to evaluate and visualize the results to determine their adequacy as well as correctness, and also to generate acceptance and reconstruction efficiency. The offline software includes all major sub-detectors.

In this chapter, the strategy used for performing the data analysis for the given thesis work is discussed and illustrated with the basic results derived from the analysis. The procedure for extracting the raw particle yields for various charged particles is also given. The results obtained for these raw yields are presented at different transverse momenta for π^\pm , K^\pm , p and \bar{p} . In addition to this, the basic information about the data set used to obtain these results is also given along with some *quality assurance* plots emphasizing the good quality of data with the optimum event and track selection employed in this analysis.

4.2 Strategy of data analysis

Before the detailed discussion, a general overview is given to provide a conceptual framework for the data analysis. In this section a general procedure is described to extract the uncorrected as well as corrected particle spectra and their properties for identified pions, kaons, protons along with their antiparticles, these corrected particle yields are further used to get the anti-particle to particle ratios. Steps of the analysis leading to the identified particle spectra are enlisted below:

1. Good events are selected from data on tape, satisfying trigger and vertex requirements. Event variables such as the uncorrected charged particle multiplicity are corrected for vertex inefficiencies upon selecting the good events in the minimum bias $p + p$ collisions. The multiplicity of the uncorrected charged hadrons in the mid-rapidity ($|\eta| \leq 0.5$) region for the present analysis work is given in Fig. 4.1 referred to as the reference multiplicity for all the charged particles (hadrons).
2. Once a good event is identified, good tracks are selected based on the analysis specific quality cuts. The details of these quality cuts for the good events as well as good tracks will be discussed in the sections to be followed viz. event selection and track selection.
3. At this point, selected data includes event and track corrections, which is followed by the extraction of raw particle yields from the multi-Gaussian fits to the $Z - distributions$ and it will be described in section 4.6.
4. The extracted raw yield at this juncture could be corrected for tracking efficiency and acceptance depending on the particle type, and multiplicity for obtaining the fully corrected identified spectra which follows the pattern as:

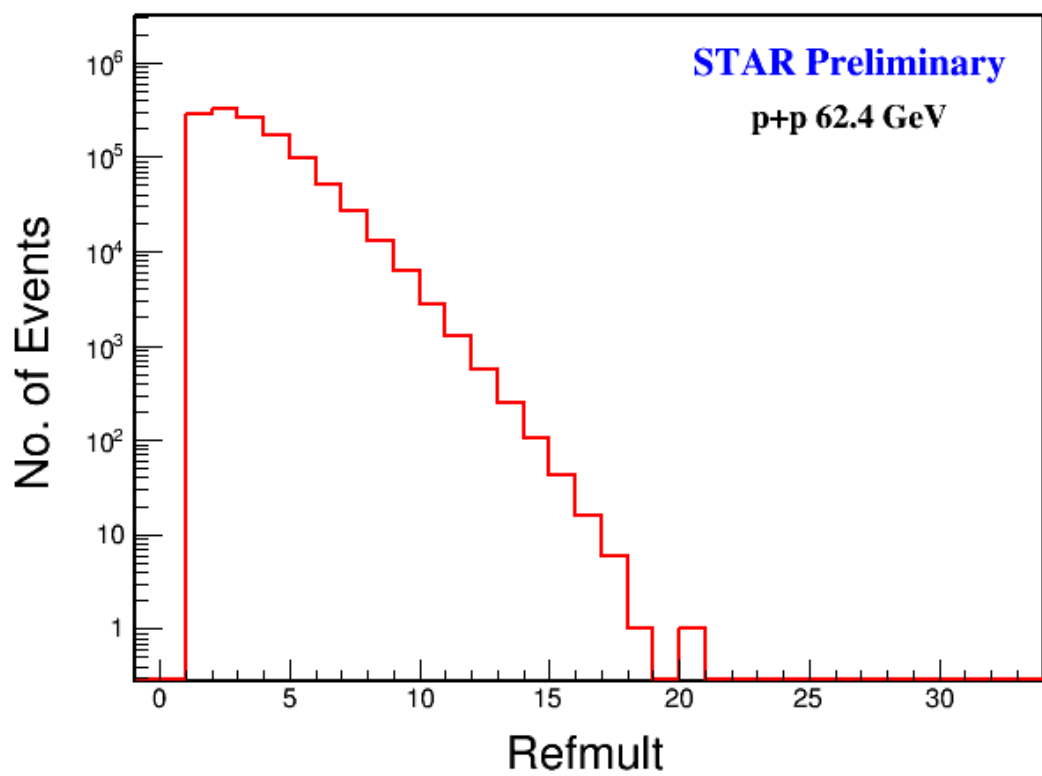


Figure 4.1: *Reference multiplicity of charged particles.*

- Raw pion yield is further corrected for weak decay contamination.
 - Raw proton yield is corrected for background contribution from detector material.
 - Finally point-to-point systematics error are assigned to each spectrum point.
5. At the end of this procedure, the fully corrected identified particle spectra could be obtained. But pertaining to this analysis work we have obtained these results for various charged particles, these particle yields are further used in estimating the useful physics observables as dN/dy , mean p_T and various particle ratios.

4.3 Data-set information

Data presented here are collected in the year 2006, for the $p + p$ collisions at center of mass energy 62.4 GeV from the production P12ia, with the minimum biased trigger with the trigger set up *ppProduction62* & *ppProductionMB62* having the trigger Id *147001*. In STAR experiment, NSD events are selected by the coincidence of the two BBC's (Beam Beam Counter) measuring the charged particle multiplicity near beam rapidity. The magnetic field used in this particular experimental Run is 0.5 Tesla. The overall approximate number of events studied before selecting the criteria for good events and tracks are of the order of ~ 1.3 million.

4.4 Event selection

The selection of quality events is of prime importance in any analysis, without which the final results obtained may actually mislead the experimentlist. It is observed that, the position of the collision points (vertices) are distributed around the center

Quantity	Cut Applied
Refmult	> 0
Ranking	> 0
V_r (cm)	< 1.0
$ V_z $ (cm)	< 30.0

Table 4.1: *The event quality cuts.*

of the TPC (center of the detector). The primary vertex position should be confined in order to select the events with the uniform detector acceptance in a given pseudo-rapidity region. Selection on the z component of the primary vertex is specific to the colliding species. The quality cuts used to select the good number of events for this analysis are shown in the Table 4.1. The relevant plots corresponding to the event information are shown in Fig. 4.2.

4.5 Track selection

Just like event cuts, tracks must also conform to certain specified limits to provide good number of tracks. The first criterion is the low p_T cut, since for the charged particle track to traverse the full volume of a TPC it must have the minimum p_T of 0.10 GeV/c. As the track having the minimum required momentum to traverse the complete volume of TPC can leave the maximum 45 hits, so in order to avoid the splitting tracks the good primary tracks should have at least 20 fit points on the track. To make sure that the tracks to be analysed come from the primary vertex the distance of closest approach (DCA) for those tracks has to be within the 3 cm of the collision point. Such tracks are termed as primary tracks. In addition to the above cuts, there are still some more quality selection cuts related to the spectra analysis involving the required number of dE/dx points and also rapidity cuts for the specific

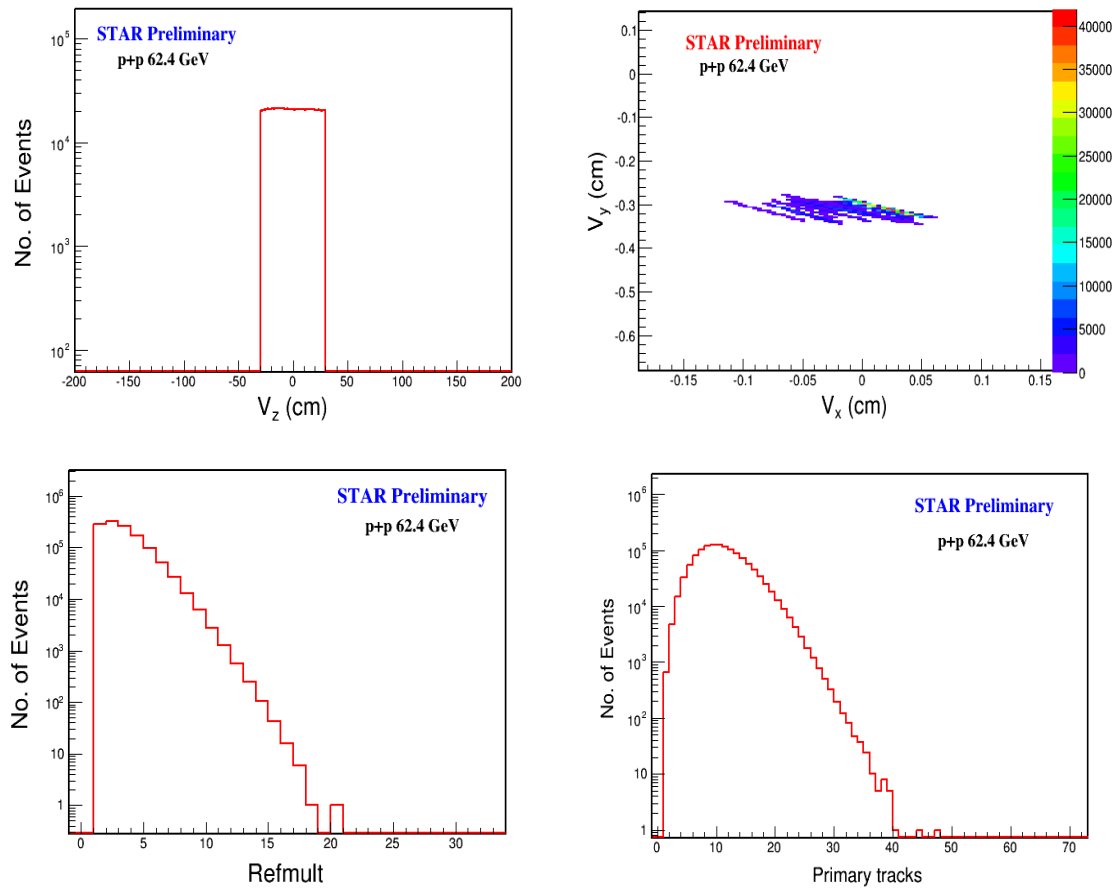


Figure 4.2: *Quality assurance plots displaying the event information.*

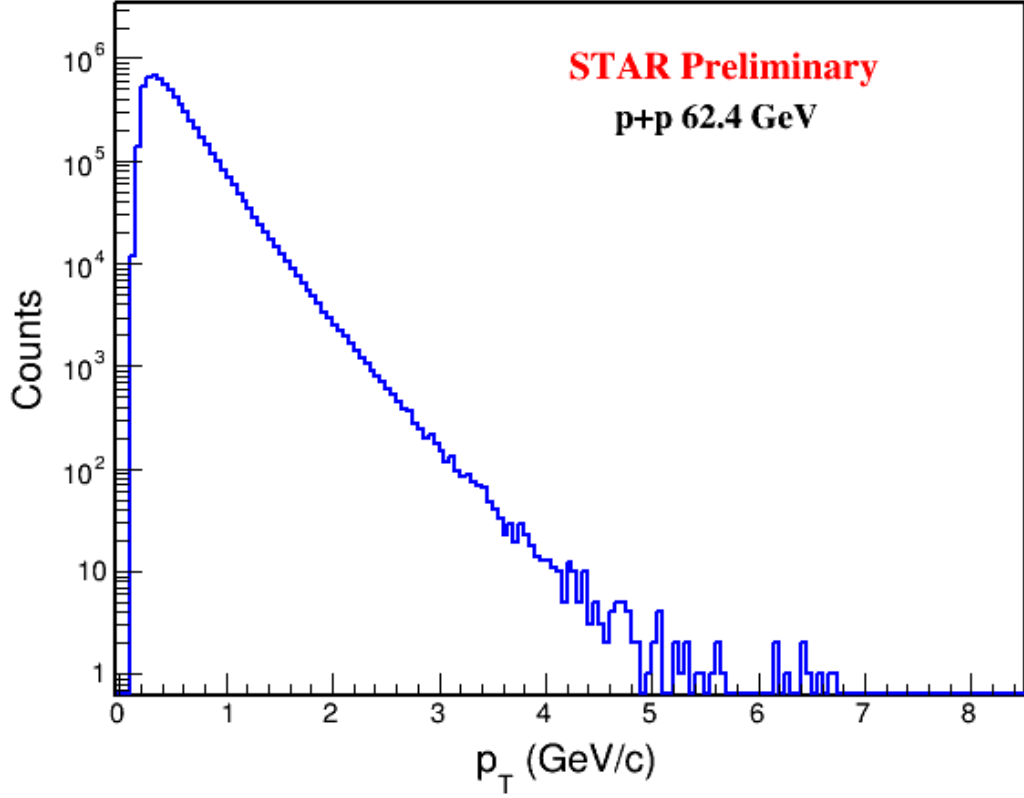


Figure 4.3: *Transverse momentum distribution of charged particles in p+p collisions.*

particles. The appropriate values for the track cuts used for this analysis are given in the Table 4.2. The p_T distribution of the charged particles is shown in the Fig. 4.3 and other relevant plots providing the track information are shown in Fig. 4.4.

4.6 Extraction of raw particle yields for various particles

In general, the gaussian distribution is described by a gaussian function $g(x)$, it has three parameters: amplitude, mean and width (sigma) and is expressed as:

$$g(x) = a \exp \left\{ -\frac{(x - b)^2}{2c^2} \right\} \quad (4.1)$$

Quantity	Cut Applied
p_T (GeV/c)	> 0.1
NfitsPts	> 20
NfitsPts/NfitsPoss	> 0.52
DCA (cm)	< 3
DCA for p & pbar (cm)	< 2
dE/dx Pts	> 5
$ y $	< 0.1

Table 4.2: *The track quality cuts*

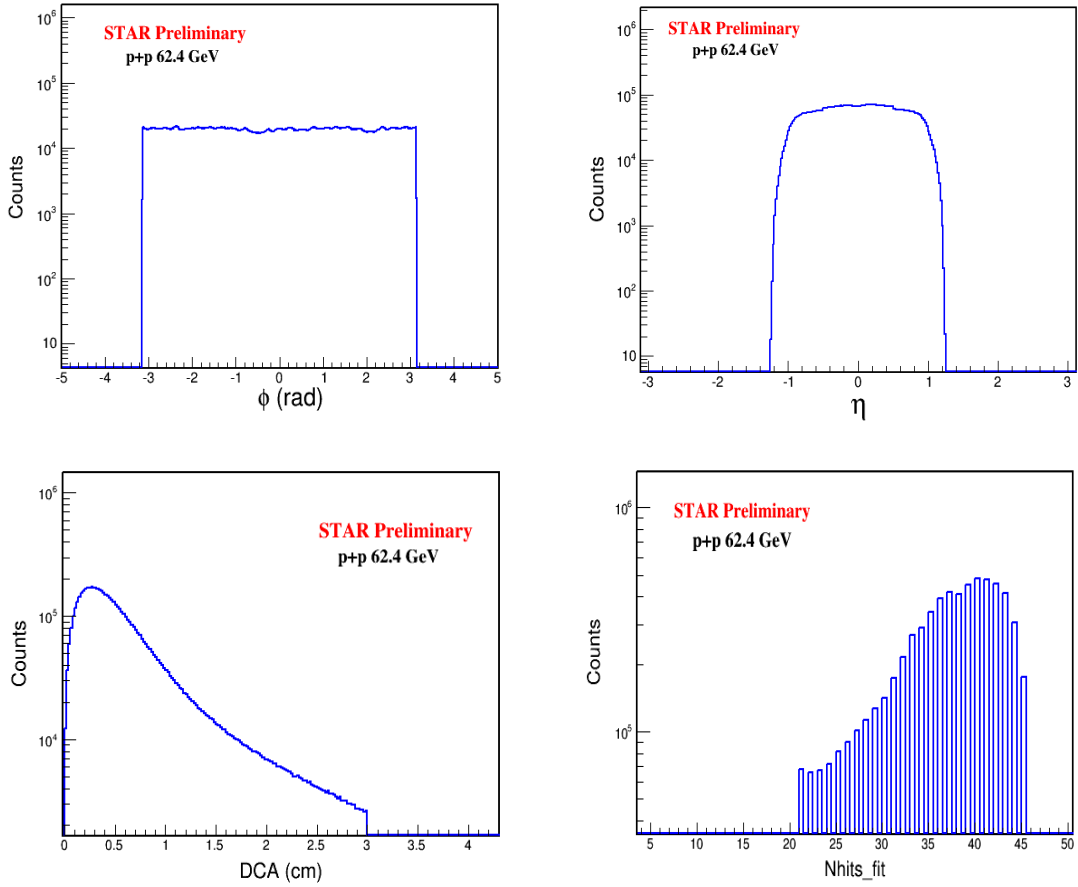


Figure 4.4: *Quality assurance plots displaying the track information.*

where a is the amplitude of the distribution, b is the mean of the distribution which is generally denoted by μ and c is the width of the distribution which is generally denoted by σ . Also the amplitude a is given as:

$$a = \frac{1}{c \sqrt{2\pi}} \quad (4.2)$$

so the equation 4.1 can be rewritten as:

$$g(x) = \frac{1}{\sigma \sqrt{2\pi}} \exp \left\{ -\frac{(x - \mu)^2}{2\sigma^2} \right\} \quad (4.3)$$

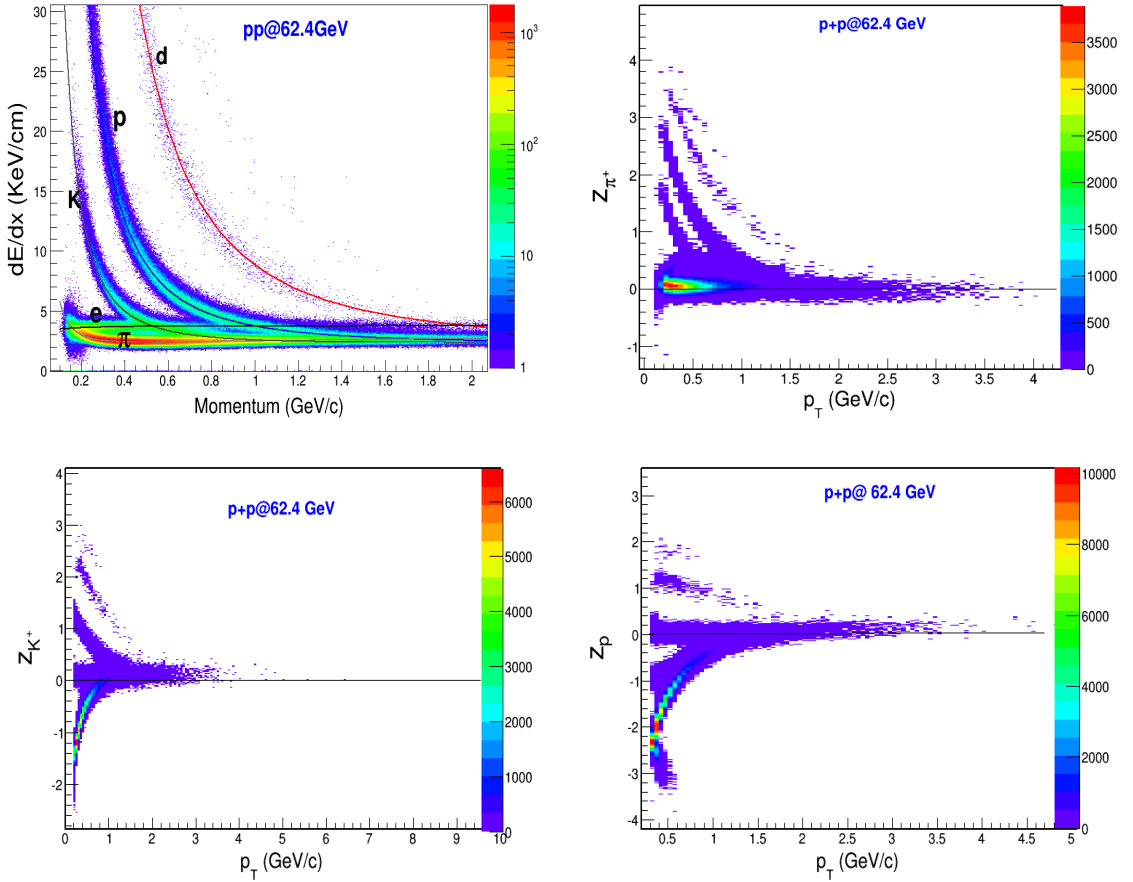


Figure 4.5: *Identification of the particles by Ionization Energy Loss.*

Since the $\langle dE/dx \rangle$ distribution (discussed in section 3.5 of Chapter 3 and is shown in the top left plot in Fig. 4.5) for a fixed particle type is not Gaussian, a new variable is useful in order to have a proper deconvolution into gaussians. It is shown that a better Gaussian variable, for any given particle type, is the Z -variable, defined as

$$Z_i = \ln \left(\frac{\langle dE/dx \rangle}{\langle dE/dx \rangle_i^{BB}} \right), \quad (4.4)$$

where $\langle dE/dx \rangle_i^{BB}$ is the Bethe-Bloch (Bichsel) [88] expectation of $\langle dE/dx \rangle$ for the given particle type i ($i = \pi, K, p$). In the present analysis, $\langle dE/dx \rangle_i^{BB}$ is parameterized as

$$\langle dE/dx \rangle_i^{BB} = A_i \left(1 + \frac{m_i^2}{p_{mag}^2} \right), \quad (4.5)$$

where m_i is the particle's rest mass, p_{mag} is the particle's momentum magnitude and A_i is the normalization factor. This parameterization is found to describe the data well. The expected value of Z_i for the any particle type in study is around zero [89]. The z distributions as a function of p_T for π^+ , K^+ and p are also shown in the top right plot and bottom plots in Fig. 4.5. For extracting the raw particle yield, the Z distributions are used for all the charged particles.

In this method, for a given particle type the z distributions/peaks are simultaneously fitted by the multiple gaussian functions, as shown in all the Fig. 4.6. Now, the parameters for the multi-gaussian fits are essentially the amplitude, mean and width for all the gaussians involved. In extracting the raw particle yield, the particle and anti-particle width are kept the same. And the particle yield extracted from the fit to the corresponding Z_i distribution is the raw yield where i represents the specific particle type. The Z_{π^+} distribution is shown for a specific p_T -bin ($0.40 \text{ GeV}/c \leq p_T \leq 0.45 \text{ GeV}/c$) as shown in Fig. 4.6, in which the blue solid-circles represent the measured Z_i distribution and the colored curves represent the multi-gaussian fits to π^\pm , K^\pm , e^\pm , $p(\bar{p})$ and also the combined fit. The fit yields from the other particle

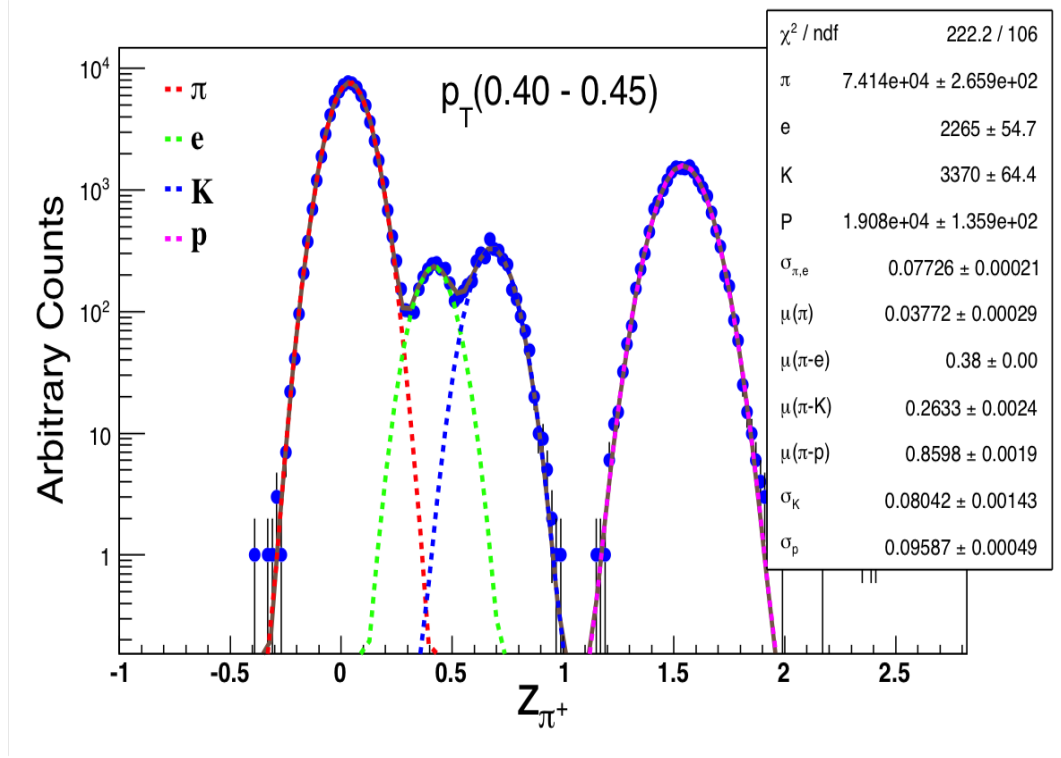


Figure 4.6: Multi-gaussian fit for the Z_{π^+} distribution for a specific p_T bin.

peaks in the distribution for specific particle cannot be used, because the rapidity calculation will be incorrect for those particle types. The same procedure is repeated for each particle type separately. For instance the charged pions can be separated in the p_T region 200-850 MeV/c. Various plots corresponding to Z_{π^+} for six different p_T bins, are shown in Fig. 4.7, whereas the plots corresponding to Z_{π^-} for six different p_T bins, are shown in Fig. 4.8.

The raw kaon yield can be extracted in the p_T region ~ 200 -800 MeV/c. The extraction of the raw kaon yield is more complicated since the electron and the kaon peaks start to merge at ~ 500 MeV/c. Therefore, the raw electron yield is extracted in the p_T region < 500 MeV/c and extrapolated in the merged bins to obtain the raw kaon yield. The measured raw electron yield is fitted to an exponential function in the p_T range 200-500 MeV/c. The fit result is fed to the multi-gaussian fit in the large p_T region and the electron yield is either fixed or left to vary within a reasonable

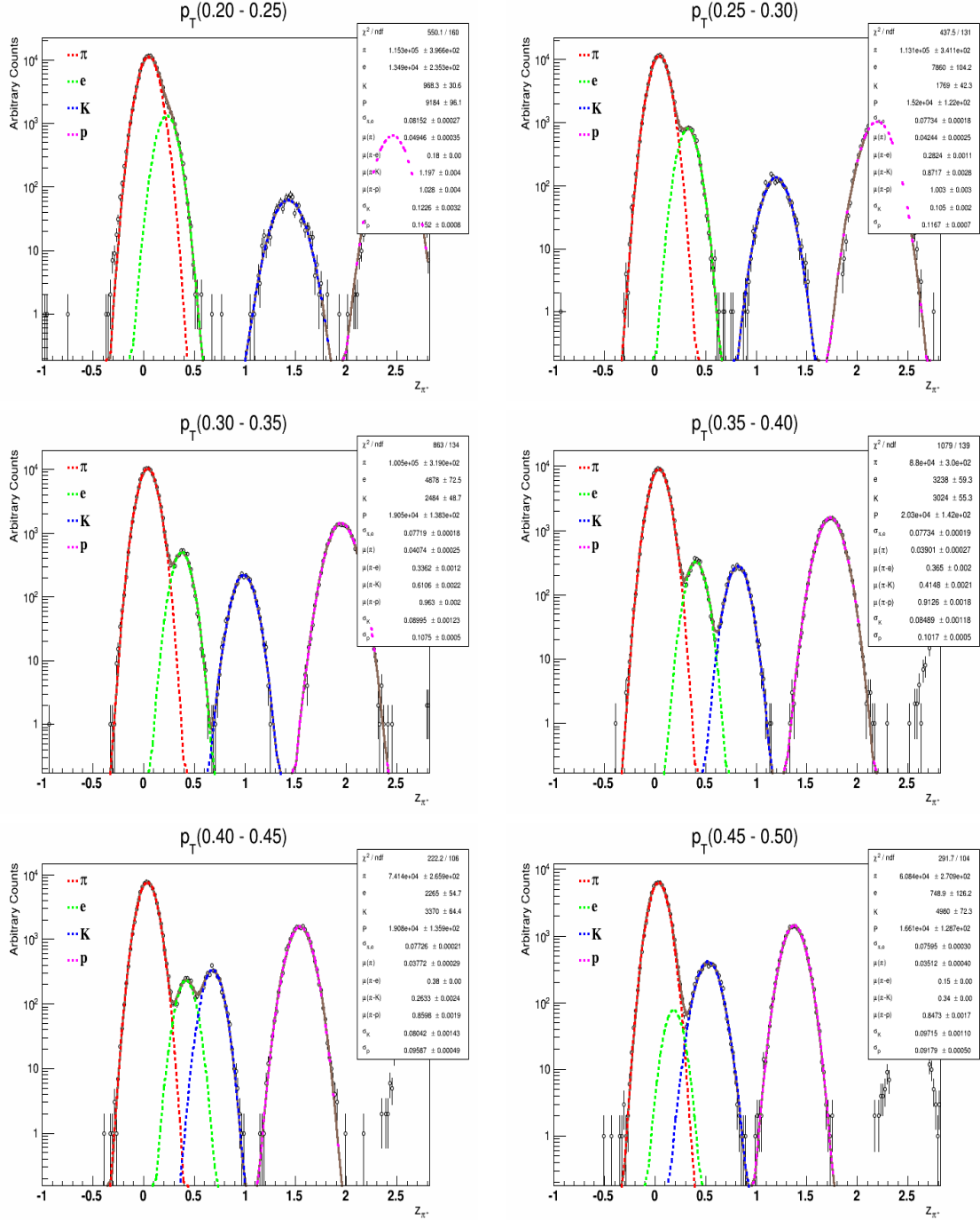


Figure 4.7: Multi-gaussian fits for Z_{π^+} for 6-different p_T bins.

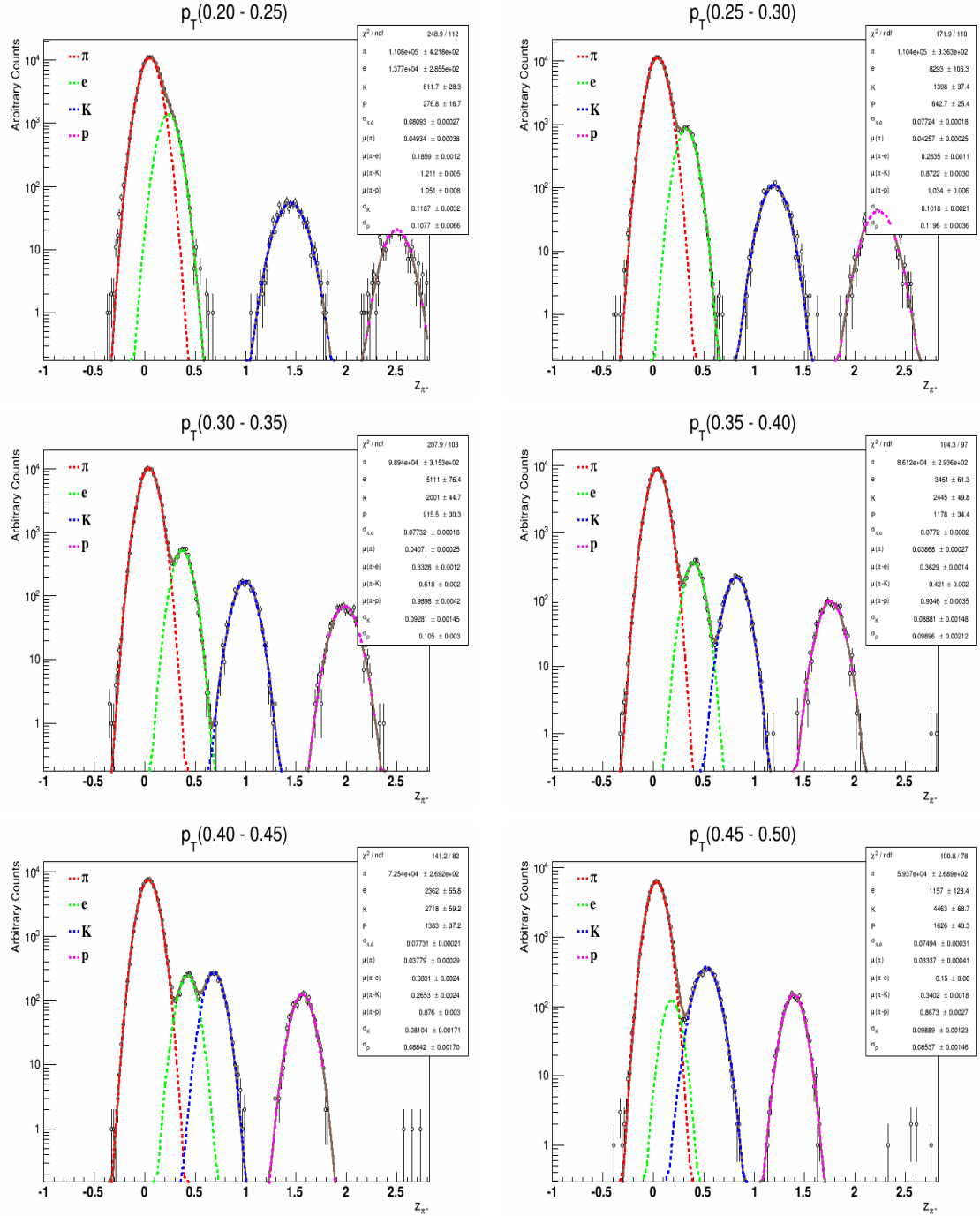


Figure 4.8: Multi-gaussian fits for Z_{π^-} for 6-different p_T bins.

range around the fitted value. The fit results for the kaons are thus shown in the various plots in Fig. 4.9 for the six different p_T bins for the Z_{K^+} , whereas the plots corresponding to Z_{K^-} for six different p_T bins, are given in Fig. 4.10.

The protons (antiprotons) are well separated from the rest of particles in the momentum region ~ 300 - 1200 MeV/c. The Z distribution plots with the multi-gaussian fits for protons and antiprotons for six different p_T bins are shown in Figures 4.11 and 4.12 respectively. So in this manner, the raw particle yield is obtained for different charged hadrons from multi-gaussian fits.

The further details of the method used for extracting the raw particle yields for charged hadrons in the lower momentum range can be obtained from the STAR Collaboration's paper [55].

4.7 Systematic uncertainties

It is important to note that, the results for all the particle yields are obtained along with their statistical uncertainties. Furthermore, the errors shown for all the final results in this thesis work for the observables like p_T spectra, particle ratios, dN/dy and mean p_T are both statistical and systematic. For the final corrected invariant yield of π^\pm , K^\pm , p and \bar{p} , the average bin to bin systematic uncertainty is estimated to be of the order of 9%. Different combinations of the various experimental variables are chosen to estimate the systematic errors. The various experimental variables selected for this study are: longitudinal vertex distribution (V_z), distance of closest approach (DCA), number of hits distribution ($NhitsPts$), dE/dx fit points ($dE/dxPts$), bin-counting method (*bin-counting*) and vertex efficiency (ϵ_{vtx}). The systematic errors in our measurements were found to be particle type and p_T dependent. For all the identified charged particles, the systematic uncertainty due to ϵ_{vtx} is of the order of 3 – 5%. For pions: the major contribution to the systematic uncertainties were due

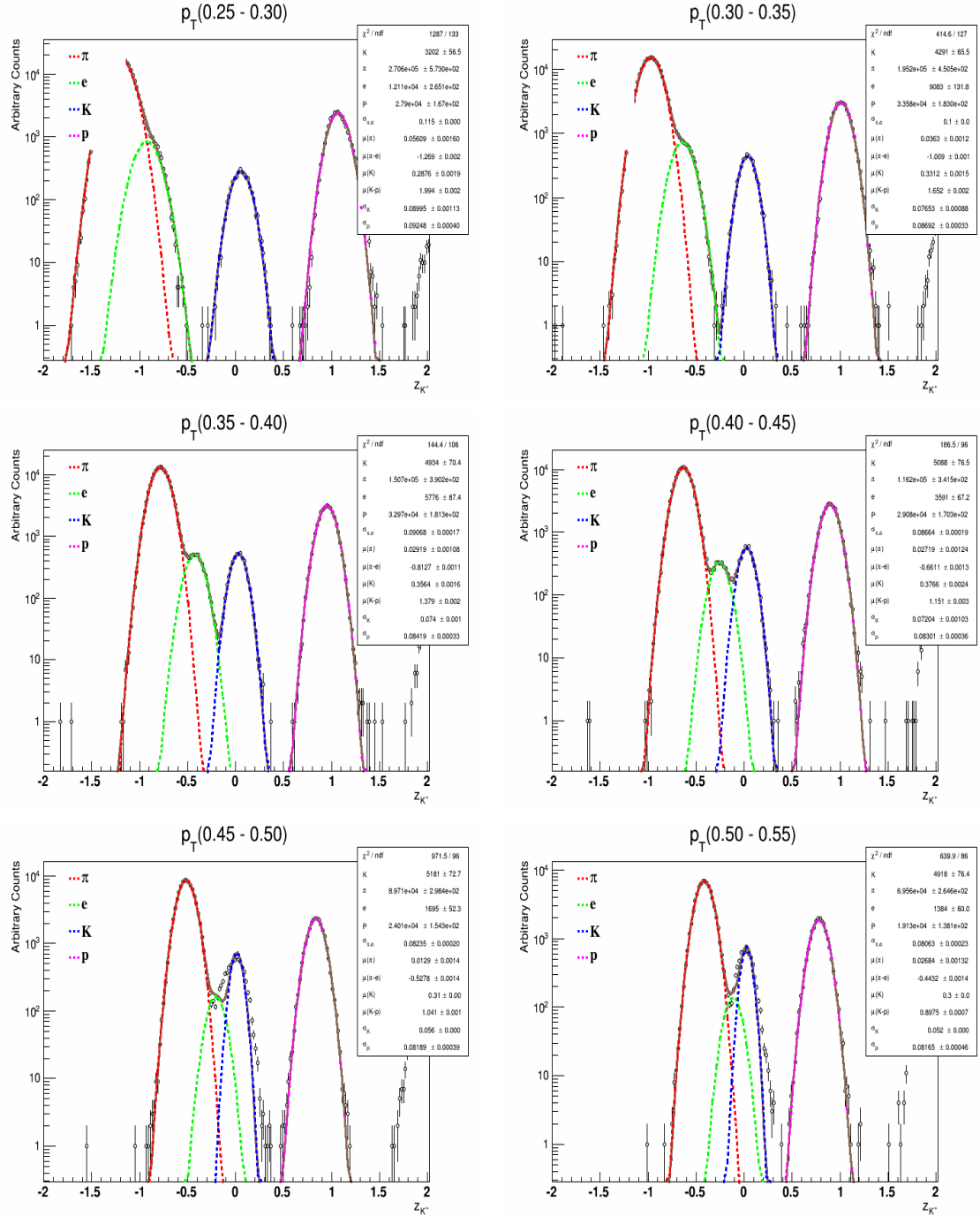


Figure 4.9: Multi-gaussian fits for Z_{K^+} for 6-different p_T bins.

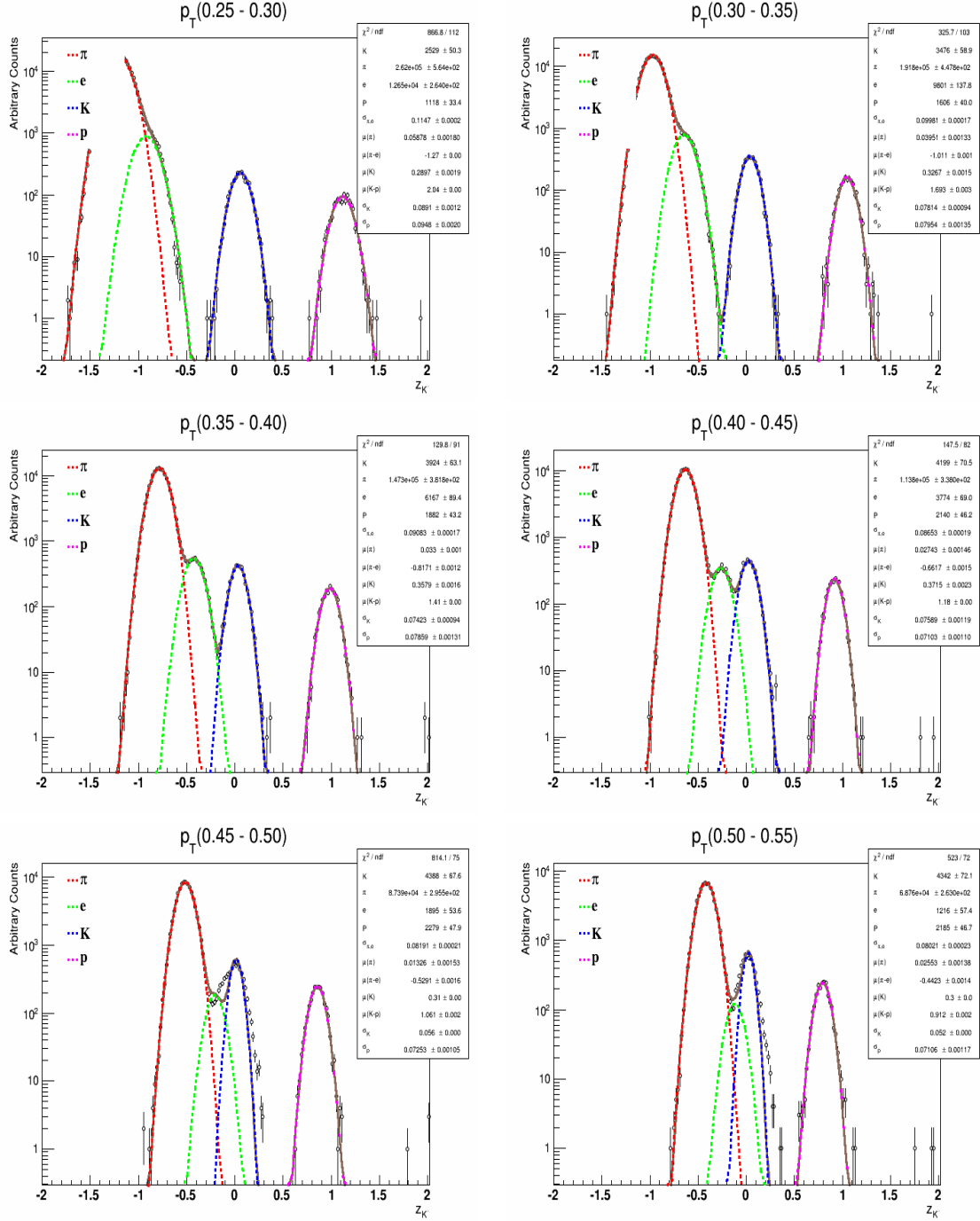


Figure 4.10: Multi-gaussian fits for Z_{K^-} for 6-different p_T bins.

to – uncertainty in *bin-counting* ($\sim 6\%$), uncertainty in V_z ($\sim 4\%$) and uncertainty in *DCA* ($\sim 3\%$). In case of kaons: the major contribution to the systematic uncertainties were due to – uncertainty in *bin-counting* ($\sim 5\%$), uncertainty in ϵ_{vtx} ($\sim 5\%$) and uncertainty in *DCA* ($\sim 3\%$). And, for protons and antiprotons: the major contribution to the systematic uncertainties were due to – uncertainty in *DCA* ($\sim 7\%$) and uncertainty in ϵ_{vtx} ($\sim 3\%$). To estimate the total systematic error for a given particle type, the various individual uncertainties are added in quadrature. The values obtained for the systematic uncertainties for the results presented in Chapter 6 are listed in the tables in the Appendix D along with the values of statistical uncertainties.

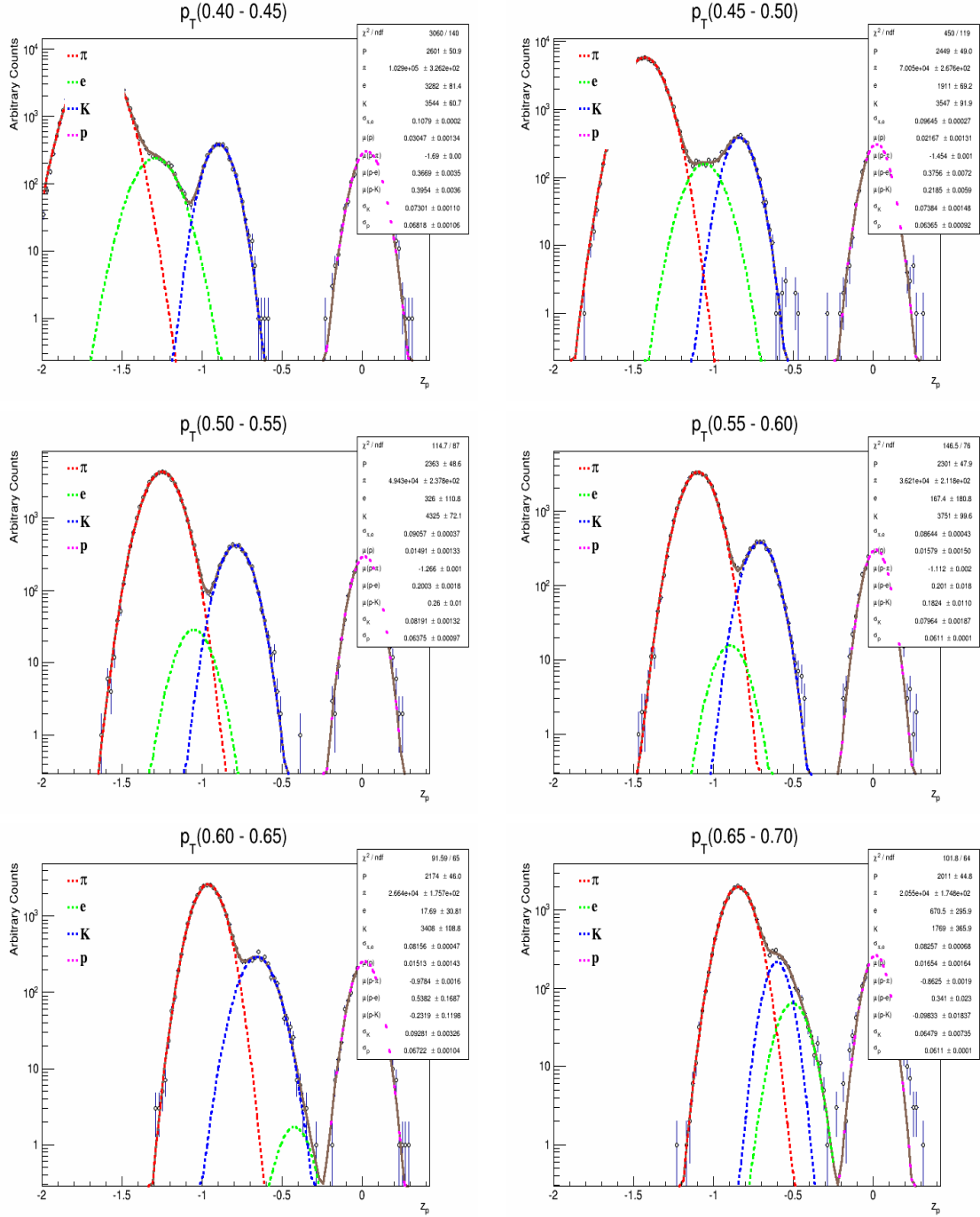


Figure 4.11: Multi-gaussian fits for Z_p for 6-different p_T bins.

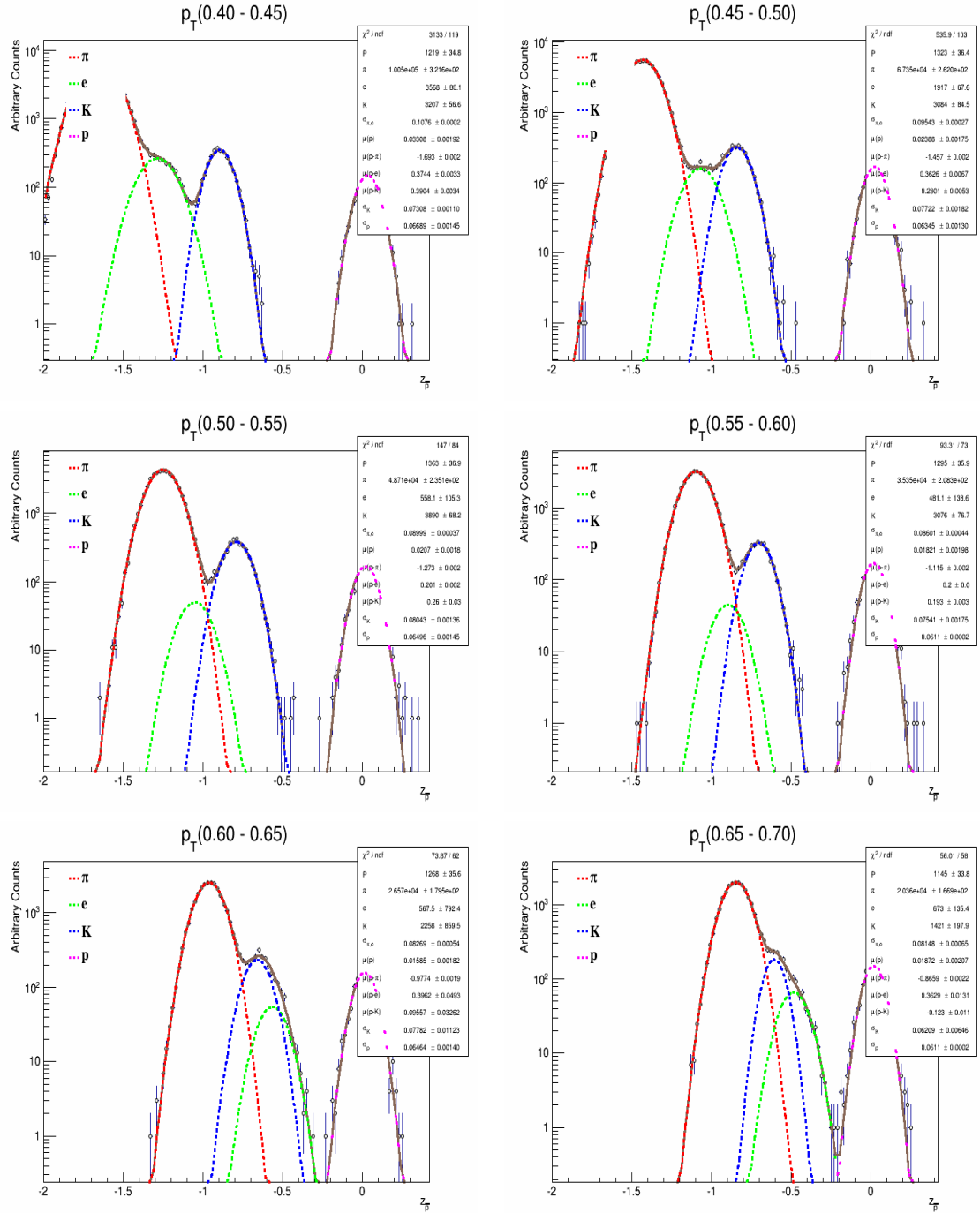


Figure 4.12: Multi-gaussian fits for $Z_{\bar{p}}$ for 6-different p_T bins.

Chapter 5

Corrections to the particle spectra

5.1 Introduction

Now that good events and tracks have been selected by applying some quality cuts as discussed in the chapter 4. In this chapter, all the corrections implemented in this analysis work will be discussed in detail to obtain the final corrected particle spectra and ratios. Prior to that, the simulation and the embedding softwares which served as an essential tools to study these corrections will be discussed.

5.2 Simulation and embedding

The simulation as well as embedding softwares provide an indispensable tool to derive the *physics results* in the detector experiments. Their significance lie in the fact that — they provide the unique way to learn about the shortcomings of the detectors, obtain the correction factors and use them to correct the experimental data, they help to understand the topology and background, so that the better sets of cuts could be found to improve the signal and they also help to evaluate the performance of reconstruction software, so as to optimize the reconstruction software. There are two

main categories of simulations:

(1) Event simulation (generator) – this simulates what happens in a real event. Different physics mechanisms are employed as per the requirement of the input conditions and the model is framed portraying the realistic environment as expected in case of real events. The most popular and commonly used models are PYTHIA, HIJING, AMPT, UrQMD etc.

(2) Detector simulation – this simulates how detectors respond to the particles which are generated from the event. The STAR experiment employs two kinds of simulators for the TPC - the TPC Response Simulator (TRS) and the TPC Fast Simulator (TFS). The TRS package simulates the response of the TPC detector gas volume and electronics to the passage of ionization energy through the TPC volume. The physical processes to be simulated by the TRS are the drift of the ionized electrons in the gas, amplification on the sense wires, induction of signal on the readout pads, and the response of the readout electronics which generate digitized data. The TFS is capable of handling the large Monte Carlo events in a very short time by directly generating the space points having the characteristics as close as possible to those hits reconstructed from the real pixel data, thus bypassing the slow TPC simulator and the cluster finder reconstruction analysis. A GEANT Monte Carlo program take the tracks from an event generator and propagates them through the TPC, generating hits corresponding to each pad-row crossing. The GEANT hits are fed into the TFS as input. The output of TFS then forms the input of the STAR TPC's tracking system.

The first step for evaluation is to relate the information from the Monte Carlo events to the information from the reconstructed events. In STAR, this functionality is realized by the StAssociationMaker package. The relationship is established through multi-maps which involve several levels of associations: (1) the first one is the hit

association which is done through proximity matching between Monte Carlo hits and reconstructed hits, where users define the distance criteria, (2) then there comes the track association. Users define the criteria for the required number of common hits. It checks how many hits on a MC track match to those with a reconstructed track. If it satisfies the criteria, it is assumed that the tracks are associated, (3) vertex association is based on the track association. Its criteria depend on particle decay topologies. For kinks, what happens in the StAssociationMaker is that it checks whether daughter tracks are associated, then whether the start vertex of the daughter track is not the primary vertex, and then whether the parent tracks are associated. In the kink analysis stage, we check whether the vertex is a weak decay vertex. Based on the three levels of association, we can proceed to do evaluation: for instance to see the hit position resolution, momentum resolution etc. Evaluation provides useful information to tune the reconstruction software.

GEANT based simulations of models are crucial to the understanding and optimization of the environment but not for the calculation of acceptance and efficiency corrections. This is because no matter how realistic the simulation is, it cannot account for effects which exist only in real data, e.g. dead channels, noise, collider background etc. So, the correction factors are obtained by the multistep embedding MC technique. First, simulated tracks are blended into real events at the raw data level. Real data events to be used in the embedding are sampled over the entire data taking period in order to have proper representation of the whole data set used in the analysis. MC tracks are simulated with the primary vertex position taken from the real events. The MC track kinematics are taken from the flat p_T distribution. The flat p_T distribution is used in order to have similar statistics in different p_T bins. The number of embedded MC tracks is of the order of 5% of the measured multiplicity in real events. The tracks are propagated through the full simulation of the STAR

detector and geometry using GEANT with a realistic simulation of the STAR-TPC response. The simulation starts with the initial ionization of the TPC gas by charged particles, followed by electron transport and multiplication in the drift field, and finally the induced signal on the TPC read-out pads and the response of the read-out electronics. All physical processes (hadronic interaction, decay, multiple scattering, etc.) are turned on in the GEANT simulation. The obtained raw data pixel information for the simulated particles are added to the existing information of the real data. Detector effects such as the saturation of ADC channels are taken into account. The format of the resulting combined events is identical to that of the real raw data events.

Secondly, the mixed events are treated just as real data and are processed through the full reconstruction chain. Clusters and hits are formed from the pixel information; tracks are reconstructed from the hits. Thirdly, an association map is created between the input MC tracks and the reconstructed tracks of the mixed event. The association is made by matching hits by proximity¹. For each MC hit from GEANT, a search for reconstructed hits from the embedded event is performed with a window of ± 6 mm in x-y, and z [90]. The window size is chosen based on the hit resolution and the typical occupancy of the TPC in central $Au + Au$ collisions. If a reconstructed hit is found in the search window, the MC hit is marked as matched. The MC track is considered to be reconstructed if more than ten of its hits are matched to a single reconstructed track in the embedded event. Multiple associations are allowed, but the probability is small of having a single MC track matched with two or more reconstructed tracks or vice versa. From the multiple associations, the effects of track splitting (two reconstructed tracks matched to one MC track) and track merging (two MC tracks matched to a single reconstructed track) can be studied. The reconstruction efficiency is obtained

¹Another possible matching algorithm is the identity (ID) truth method, where the track ID information is propagated to the reconstructed hits.

by the ratio of the number of matched MC tracks to the number of input MC tracks. The reconstruction efficiency contains the net effect of tracking efficiency, detector acceptance, decays, and interaction losses. The most critical quality assurance is to make sure that the MC simulation reproduces the characteristics of the real data. This is carried out by comparing various distributions from real data and from embedding MC as shown in Fig. 5.1. Good agreement is found between embedding MC and real data.

5.3 Corrections

Several corrections are required to be applied to the real data. The schematic flow chart of all the corrections done in the present analysis is shown in Fig. 5.2. The following subsections discuss all these corrections in detail.

5.3.1 Trigger and Vertex efficiency

As the minimum biased (MinBias) data are analysed for the present analysis work, wherein the MinBias trigger in $p + p$ collisions require the coincidence of signals from the two BBC detectors on the opposite sides of the interaction point. Due to the dual-arm configuration, this trigger was sensitive to the non-singly diffractive (NSD) cross section, which is a sum of the non-diffractive and double diffractive cross sections. The BBC trigger efficiency has been studied previously ($87.0 \pm 8\%$) [91] and taken care of in this study.

In $p + p$ and $d + Au$ collisions, the average number of tracks per event is small compared to $Au + Au$ collisions, and the event rate is high. In very low multiplicity events ppLMV algorithm can fail to find the vertex when the fits do not converge at a point and the vertex is not found at all - such events are called *lost events*. Also, the

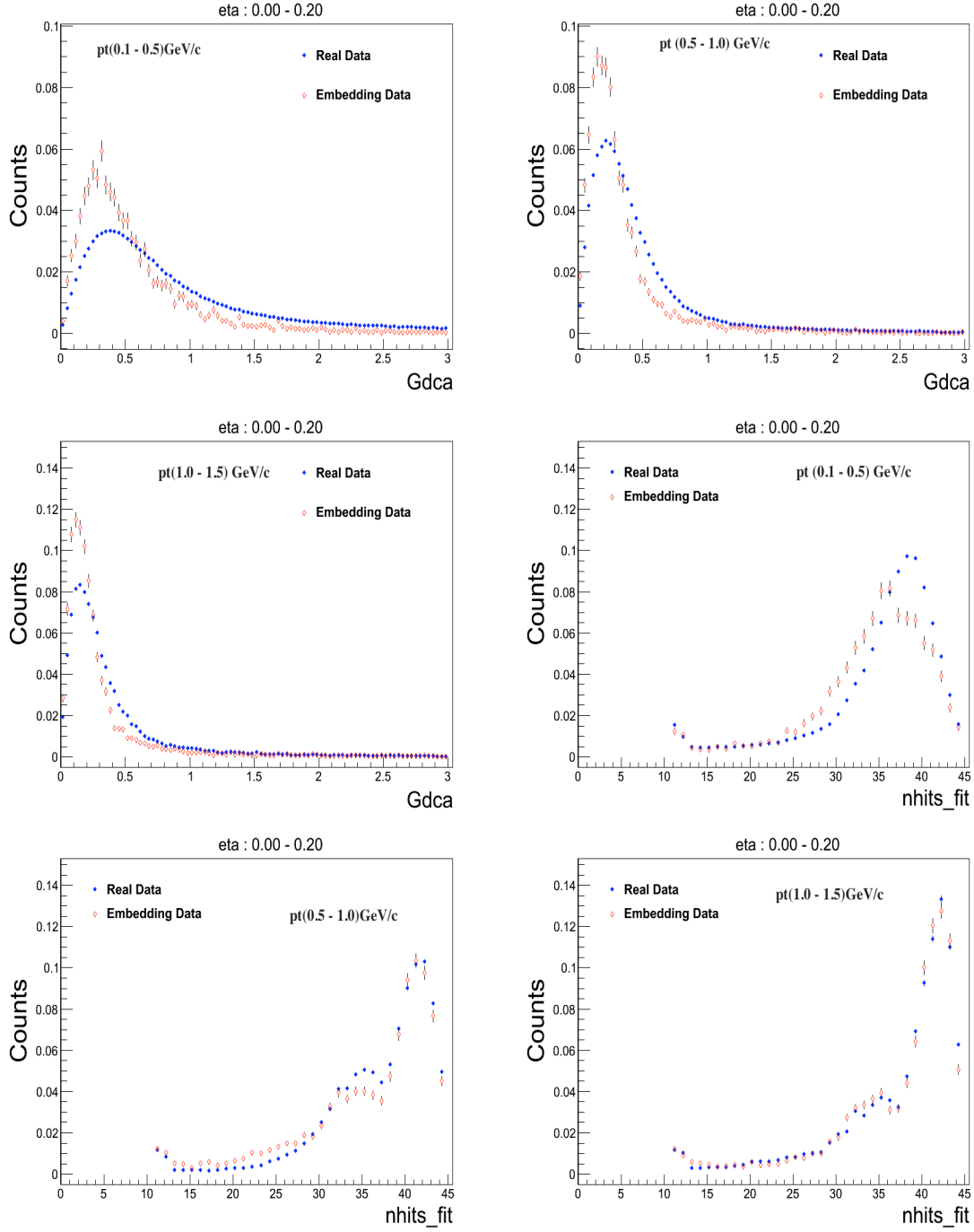


Figure 5.1: Comparison of DCA and Nhits distributions for different η and p_T bins of embedding and real data.

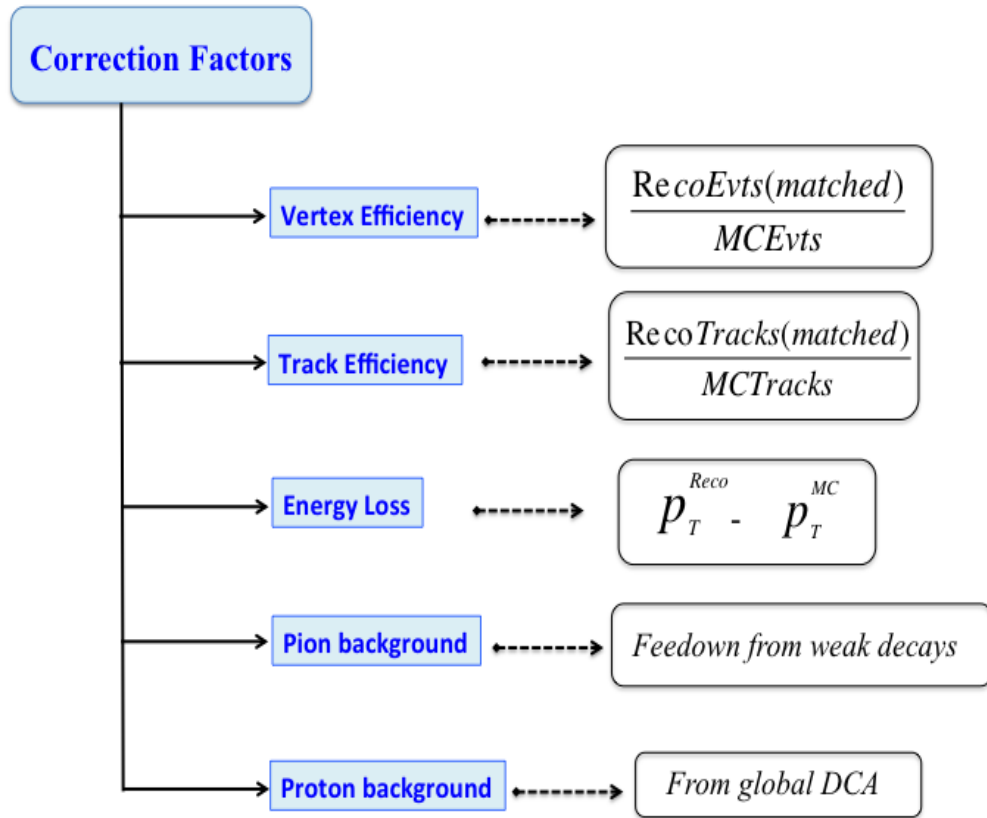


Figure 5.2: Flowchart showing different corrections done in this analysis.

Pile-up² can shift the position of the reconstructed primary vertex i.e. the ppLMV algorithm causes the vertex to be found in the wrong place - such events are called as *fake events*. One must therefore quantify the efficiency of the standard vertex finder to determine if a bias exist. In real data, it is impossible to know where the actual vertex is located, so one must use simulations. In order for the simulations to be valid, they must accurately reproduce the detector environment.

In high multiplicity $Au + Au$ collisions, the primary vertex can be determined accurately. The vertex-finding efficiencies in $p + p$ and $d + Au$ collisions are studied by HIJING-MC events embedded into *Abort - gap*³ or *Zero - bias* events. For this analysis, we have used the zero-bias events, which represents the background in the real collision environment. The embedded event is subsequently reconstructed by the full reconstruction chain. In every MC event, there is a well-defined primary vertex. With the embedded event reconstructed (after passing through GEANT) and the MC information in hand, the vertex-finding efficiency can be obtained.

The overall vertex-finding efficiency ϵ_{vtx} is determined as the ratio of the number of reconstructed events with the correct vertex position (matched reconstructed tracks to the input MC tracks) to the number of input MC events [89]:

$$\epsilon_{vtx} = \frac{\text{No. of good reconstructed events (matched)}}{\text{No. of good MC events}}, \quad (5.1)$$

The Vertex finding efficiency is obtained as a function of number of primary tracks and is shown in Fig. 5.3. After getting the vertex-finding efficiency, each event and each track is weighted by the inverse of the ϵ_{vtx} to obtain the correct number of events and primary tracks. From the Fig. 5.3, it is clear that the vertex-finding efficiency strongly increases with increasing multiplicity resulting in approximately 5% of events

²multiple bunch crossing within the same readout window.

³events triggered and reconstructed at empty bunch crossings.

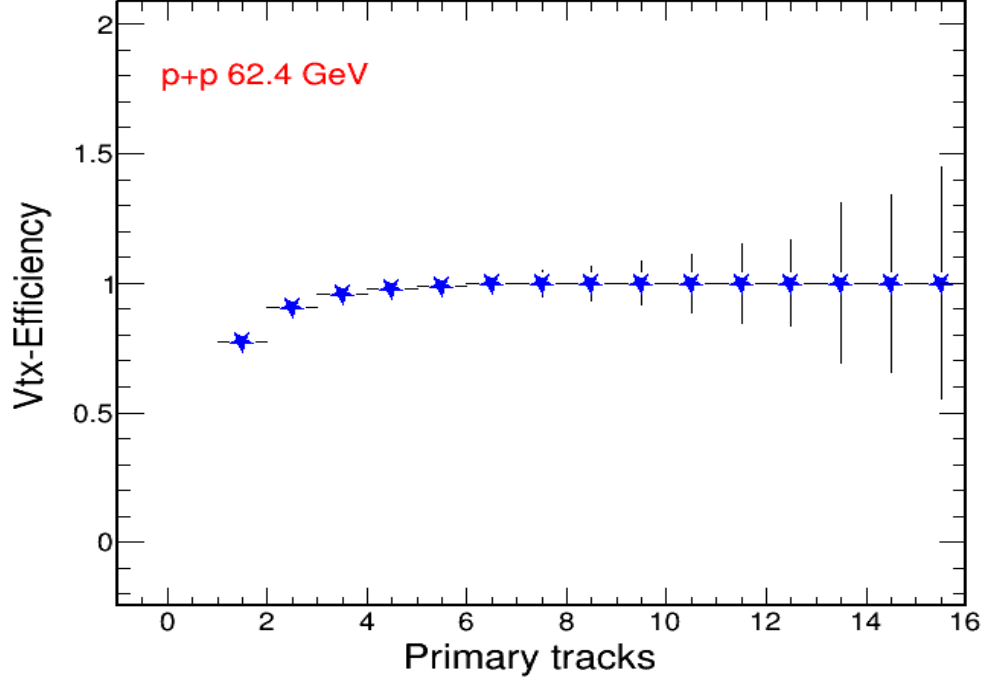


Figure 5.3: *Vertex Efficiency as a function of number of primary tracks.*

being missed, over 95% of which have fewer than three tracks in the TPC. Keeping this observation into account, the effect of this correction has been included into the systematic uncertainties for the spectra results presented in the Chapter 6.

5.3.2 Tracking efficiency

This correction is essential to all the spectra analysis irrespective of the particle species involved in collisions. Here the raw particle spectra are corrected for the detector acceptance and the tracking efficiency. These are obtained from the MC embedding technique as discussed in the section 5.2. The track reconstruction efficiency can be defined as the ratio of the matched reconstructed tracks to the MC tracks and is expressed as:

$$\epsilon_{trk} = \frac{\text{No. of good reconstructed tracks (matched)}}{\text{No. of good MC tracks}}, \quad (5.2)$$

The Fig. 5.4 shows the tracking efficiency for π^\pm , K^\pm , p and \bar{p} . The curves shown in all the plots of Fig. 5.4 are parameterizations to the efficiency data and are used for implementing the corrections in the analysis. It is also worth the while to mention here that in estimating the efficiency for all the particles, the similar cuts corresponding to the event and tracks are applied as used in the real data. From the efficiency plots one can observe the p_T dependence for different particles in $p + p$ collisions at 62.4 GeV. The pion efficiency is independent of p_T for $p_T > 0.3$ GeV/c, but falls steeply at lower p_T , because the particles with low p_T cannot traverse the entire TPC due to their large track curvature inside the solenoidal magnetic field. For kaons, the efficiency increases smoothly with p_T and already includes decay loss which decreases with the increasing p_T . The comparatively smaller kaon efficiency at lower p_T than pions is caused by the large loss of kaons due to decays. The efficiency for protons and antiprotons is also independent of p_T above 0.5 GeV/c. However, at lower p_T , the efficiency drops steeply because of the large multiple scattering effect due to the large (anti)proton mass.

5.3.3 Energy loss correction

This correction is also obtained from the embedding data by comparing the reconstructed p_T and the MC p_T for all the charged tracks. As the low momentum particles lose some energy while passing through the TPC's volume, thereby affecting the actual measurement of the momentum of each track. Figure 5.5 shows the energy loss correction for pions, which clearly indicates that the transverse momentum difference is flat through the measured p_T range. This is because the reconstruction algorithm takes into account the energy loss and multiple Coulomb scattering effects for pions. The blue line shown in Fig. 5.5 is an arbitrary linear fit to guide the eye. However, kaons and protons/antiprotons show larger discrepancy between the MC and the re-

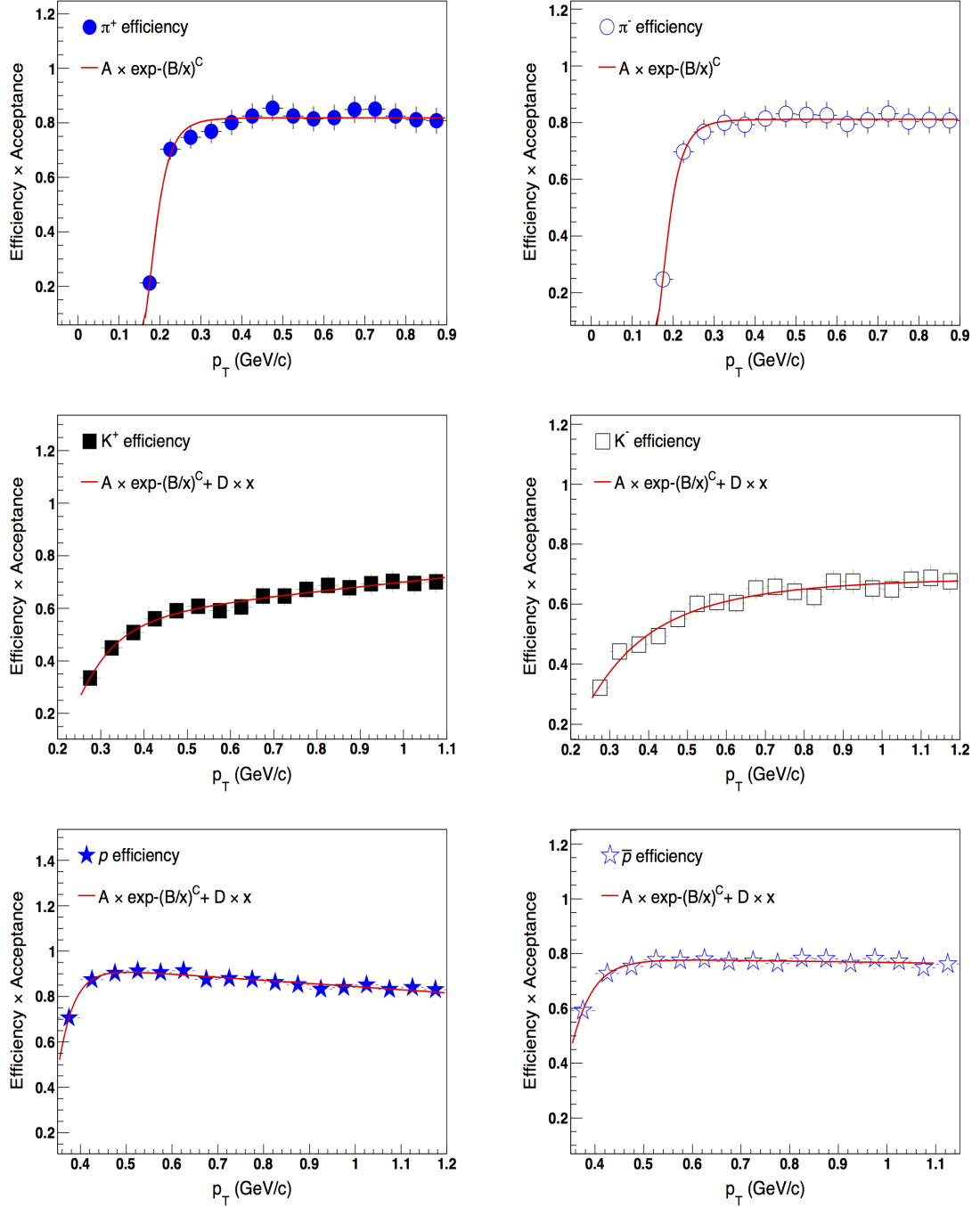


Figure 5.4: $Efficiency \times Acceptance$ for π^\pm , K^\pm , p and \bar{p} .

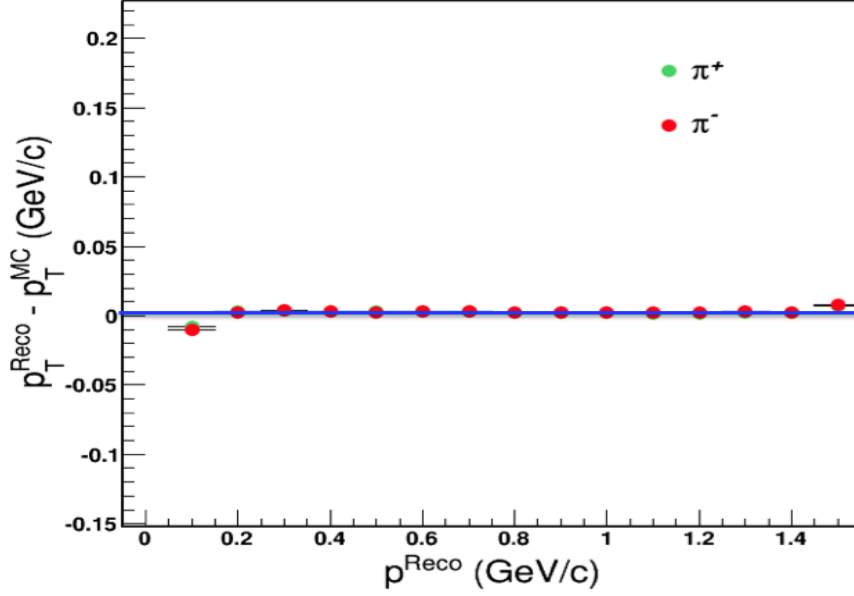


Figure 5.5: *Energy loss effect for π^\pm as a function of p_T in $p + p$ event.*

constructed transverse momentum at low momentum and the deviation from MC input is the same for particles and antiparticles as is clear from Fig. 5.6. Also, the data points shown in all the plots of Fig. 5.6 corresponds to energy loss measurements where as curves represents the parameterizations to the energy loss data and are used for implementing the corrections in the analysis independently for each particle type. The energy loss correction is applied offline to all the tracks using the parameterizations as depicted in the legends of each plot in Fig. 5.6 for each particle. Now, once this correction is done, the corrected p_T for all the tracks is obtained and is used in all the results for this analysis.

5.3.4 Pion background correction

Unlike the embedding data where real events are also embedded into the Monte Carlo events, here corrections are extracted from PYTHIA simulations propagated through the STAR geometry and reconstructed as real tracks. For each simulated particle, the information about its parent, daughter, origin, process, decay etc. is already known.

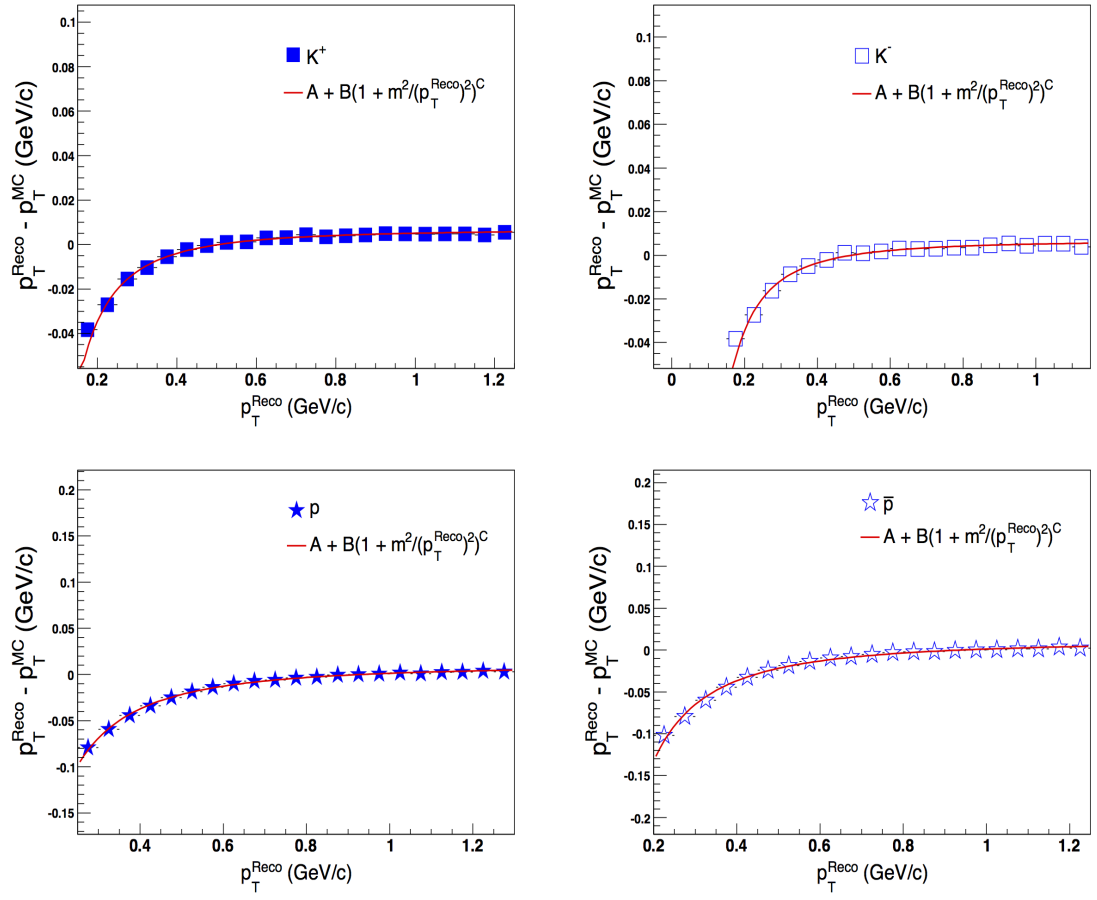


Figure 5.6: Energy loss effect for K^\pm , p and \bar{p} as a function of p_T in $p + p$ events.

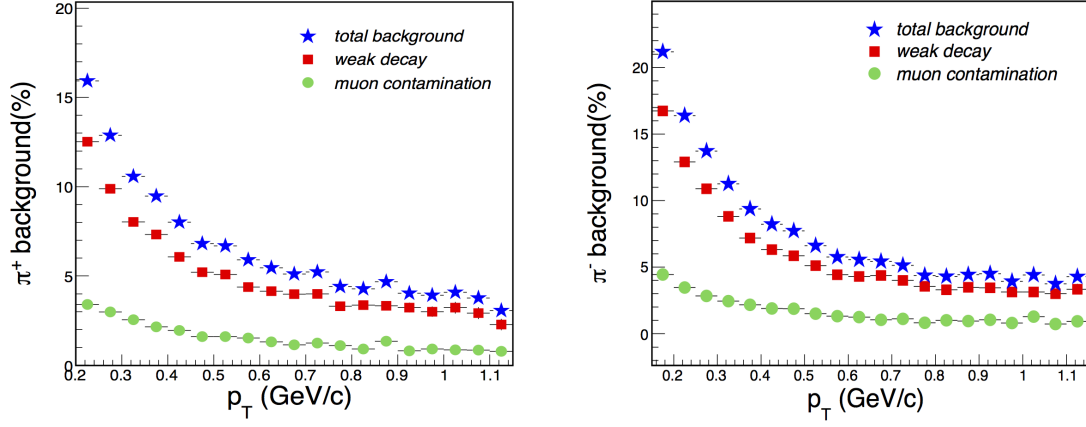


Figure 5.7: Pion background fraction from weak decays (K_s^0 & Λ), μ^\pm contamination and total background as a function of p_T in $p + p$ events.

With all this information in hand one can select the primary pions, pions from decay of other particles as well as those coming directly from the detector material. The main contribution to the background pions comes from the weak-decay of pions from K_s^0 and Λ . Also muons from the decay of pions can be misidentified as primordial pions because of the similar masses of muon and pion. These contaminations can be obtained from the parent particle information and by identifying the decays of the particles, which could be easily accessible from the MC simulation. Having these crucial informations in hand and applying all the quality cuts, one can estimate the total pion background for each p_T bin as shown in Fig. 5.7 for π^+ and π^- background.

5.3.5 Proton background correction

Apart from the primordial yields, there is a lot of background protons being detected alongwith the primary yields. The main sources of these background protons are: background protons from the detector material (main contributor of the secondary protons) and weak-decay protons from the hyperons (this study is beyond the scope

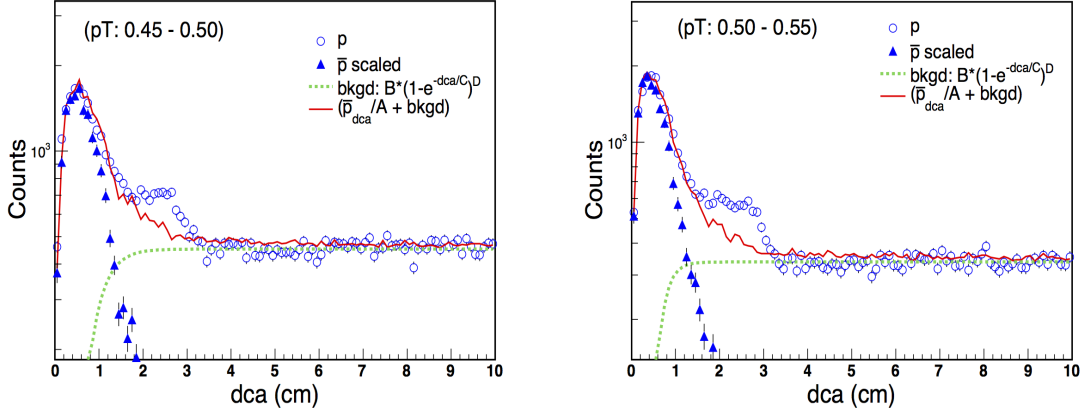


Figure 5.8: *Global DCA distributions of the protons and antiprotons alongwith the background contamination in the $p + p$ events for two different p_T bins.*

of this analysis). As per the previous studies on proton background estimation [92], the proton sample contains background protons knocked out from the beam pipe and the detector materials by interactions of produced hadrons in these materials. Most of these protons have large DCA and are not reconstructed as primary particles. However, some of these background protons have small DCA and are therefore included in the primary track sample and hence correction is needed.

In order to obtain the background protons, the global DCA distribution is studied from the real data and the percentage of background protons is estimated from the same distribution; though, the shape of the background protons is estimated from the MC simulation study. Figure 5.8 shows the DCA distribution of protons and antiprotons for two different p_T bins in $p + p$ at 62.4 GeV collisions. From both the plots in Fig. 5.8, one can observe the long, nearly flat DCA tail which mainly arises due to the knock-out background protons. This effect is large at low p_T bins and significantly reduces at high p_T . As antiprotons do not have knock-out background, so the flat tail is absent from their DCA distributions. Most of the knock-out protons are eliminated by applying the strict DCA cut (< 3 cm). However, it is observed in

Fig. 5.8, that there is a bump at DCA ~ 2.5 -3.0 cm range, so we have applied a DCA cut (< 2 cm) as a default cut specifically for proton and antiproton analysis for all the results.

Based on the MC simulation studies, the following functional form is used to describe the background protons:

$$bkgd = B(1 - e^{-DCA/C})^D, \quad (5.3)$$

Now, assuming that the shape of the background subtracted proton DCA distribution is identical to that for the antiproton DCA distribution, the proton DCA can be fit by the following functional form:

$$p_{dca} = \bar{p}/A + B(1 - e^{-DCA/C})^D, \quad (5.4)$$

where the magnitude of the background protons B , the parameter C , the exponent D and the antiproton to proton ratio A are the free parameters. The dashed curve in Fig. 5.8 represents the protons background, the solid triangle symbols represents the scaled antiproton DCA distribution. The red curve represents the functional form (as discussed in the eq. 5.4) used to fit the proton DCA shown with the open circles in Fig. 5.8.

Chapter 6

Transverse momentum spectra and particle ratios

6.1 Introduction

The raw particle yields obtained in the Chapter 4 for different charged particles are corrected for different corrections whichever necessary for a specific particle type (the correction factors are obtained in the Chapter 5). The corrected invariant yields for π^\pm , K^\pm , p and \bar{p} for STAR experiment in $p+p$ collisions at $\sqrt{s} = 62.4$ GeV are given in this Chapter. The antiparticle to particle ratios (π^-/π^+ , K^-/K^+ & \bar{p}/p) as well as unlike particle ratios (K^\pm/π^\pm , $p(\bar{p})/\pi^\pm$) for the identified particles are also obtained. The measurements are compared with expectations from pQCD inspired models like PYTHIA and PHOJET. The data are also compared with the measurements from the PHENIX experiment at the same center of mass energy. The results for invariant yield per unit rapidity (dN/dy) and the average transverse momentum ($\langle p_T \rangle$) are also presented in this Chapter.

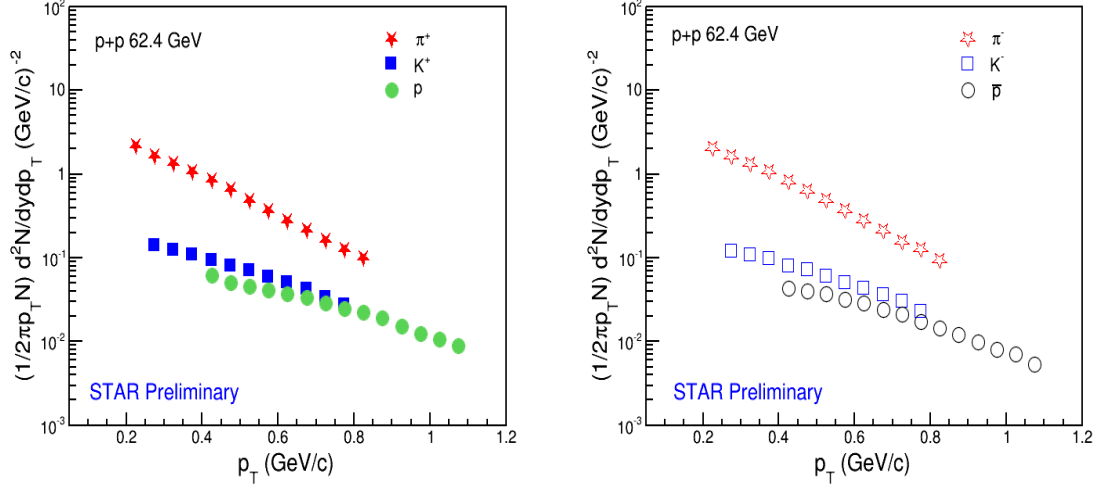


Figure 6.1: Identified transverse momentum spectra for π^\pm , K^\pm , p and \bar{p} (positive particles: filled symbols in left panel and negative particles: open symbols in right panel) measured at mid-rapidity ($|y| < 0.1$) for $\sqrt{s} = 62.4$ GeV in $p + p$ collisions. Errors are both statistical and systematic added in quadrature. The size of the error bars are smaller than the symbol size.

6.2 Transverse Momentum Spectra

The invariant differential yields ($\frac{1}{2\pi p_T N_{Evs}} \frac{d^2 N}{dy dp_T}$) are constructed for various charged particles in the minimum bias $p + p$ collisions at mid-rapidity ($|y| < 0.1$) for $\sqrt{s} = 62.4$ GeV. The results are presented for π^\pm , K^\pm , p and \bar{p} after being corrected for detector acceptance, tracking efficiency, feed-down from the weak decays, background contamination as well as vertex and trigger efficiency. The final spectra so obtained after implementing all the corrections is given by the eq 6.1 as:

$$E \frac{d^3 N}{dp^3} = \frac{1}{2\pi p_T N_{Evs}} \times C_{eff}^{trig} \times C_{eff}^{trk} \times C_{feed} \frac{d^2 N}{dy dp_T}, \quad (6.1)$$

where, C_{eff}^{trig} , C_{eff}^{trk} and C_{feed} are the correction factors for the trigger efficiency, tracking efficiency and the feed-down correction respectively. These correction factors have already been discussed in Chapter 5. The corrected p_T spectra (as per the eq. 6.1)

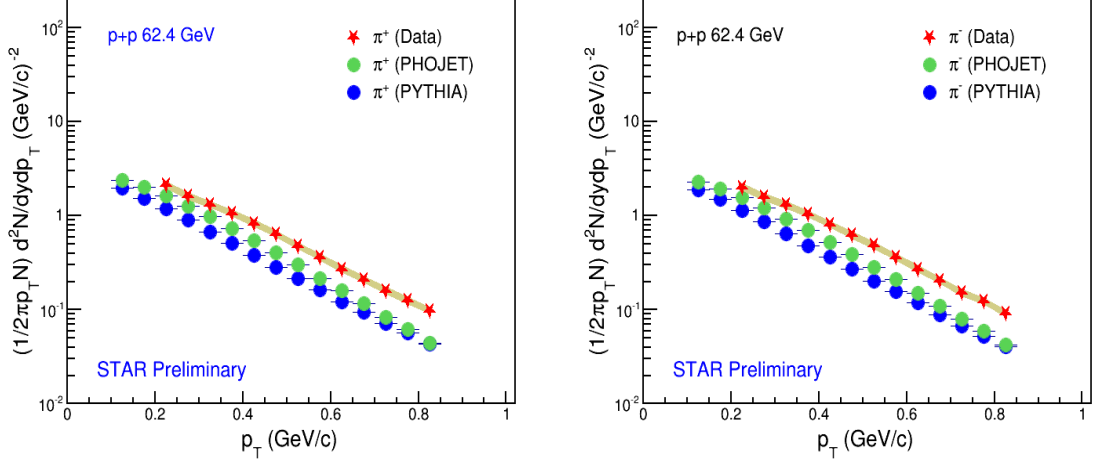


Figure 6.2: Identified transverse momentum spectra for π^\pm (positive particles: are shown in the left panel and negative particles: are shown in the right panel) measured at mid-rapidity ($|y| < 0.1$) for $\sqrt{s} = 62.4$ GeV in $p + p$ collisions. Statistical errors are shown with bars whereas the systematic errors are shown with the shaded band.

for particles and antiparticles are shown in Fig. 6.1.

In $p + p$ collisions, the particle production models describe a static, thermal source that leads to exponential behavior of the particle spectra at low momentum. The spectral shapes observed in Fig. 6.1 follow a nice exponential form for both particles and their antiparticles. The slopes of the spectra for the π^\pm are steeper than K^\pm , which in turn are steeper than protons and antiprotons. Such observations have also been reported in the low energy heavy ion collisions, wherein the pressure generated during the collision process boosts the produced particle away from the center of the collision. This mechanism leads to an expanding source, which might be thermalized. This pressure generated boost manifests itself in the change of the shapes of particle spectra, depending on the mass of the measured particle [97].

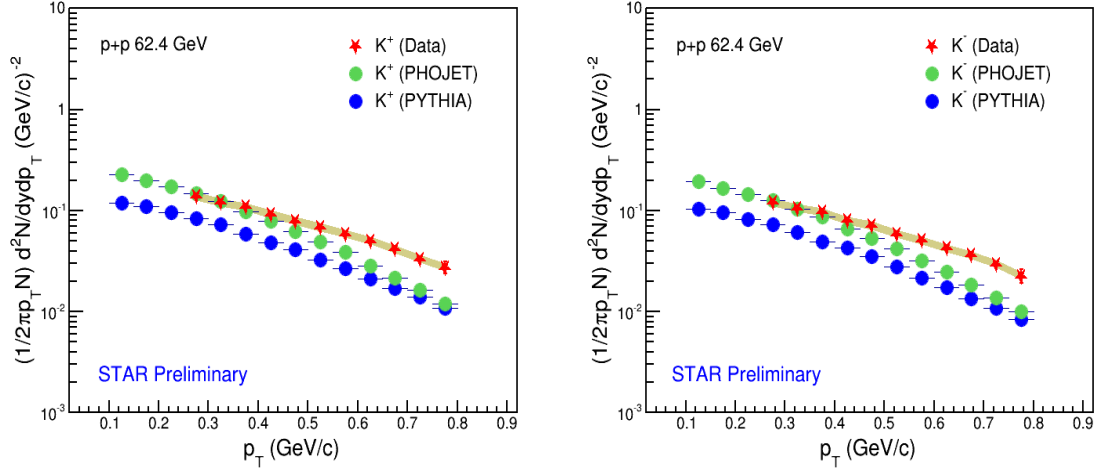


Figure 6.3: *Identified transverse momentum spectra for K^\pm (positive particles: are shown in the left panel and negative particles: are shown in the right panel) measured at mid-rapidity ($|y| < 0.1$) at $\sqrt{s} = 62.4$ GeV in $p + p$ collisions. Statistical errors are shown with bars whereas the systematic errors are shown with the shaded band.*

6.2.1 Comparison with the models

In this section, we compared the p_T spectra of various charged particles with the expectations from PYTHIA and PHOJET models. The stable version of the PYTHIA (6.4) and the PHOJET (1.12) are used for model calculations. The spectra results from the STAR measurements and the model calculations are further studied individually for different charged particles. Figure 6.2 shows the results for the pion spectra along with their comparison with the model calculations. The results for the p_T spectra for the K^\pm , p and \bar{p} are also presented in Figures 6.3 and 6.4 respectively. In all the plots as shown in Fig. 6.2 to 6.4, the star symbols represent the STAR data whereas the solid circle symbols represent the model calculations.

From Figures 6.2 to 6.4, it can be inferred that, the models reproduce the shape of the spectra, though the effect gets less significant with the increase in p_T , but they clearly underpredict the data. Hence, the data measurement presented in this thesis work can be very useful in constraining these QCD inspired models.

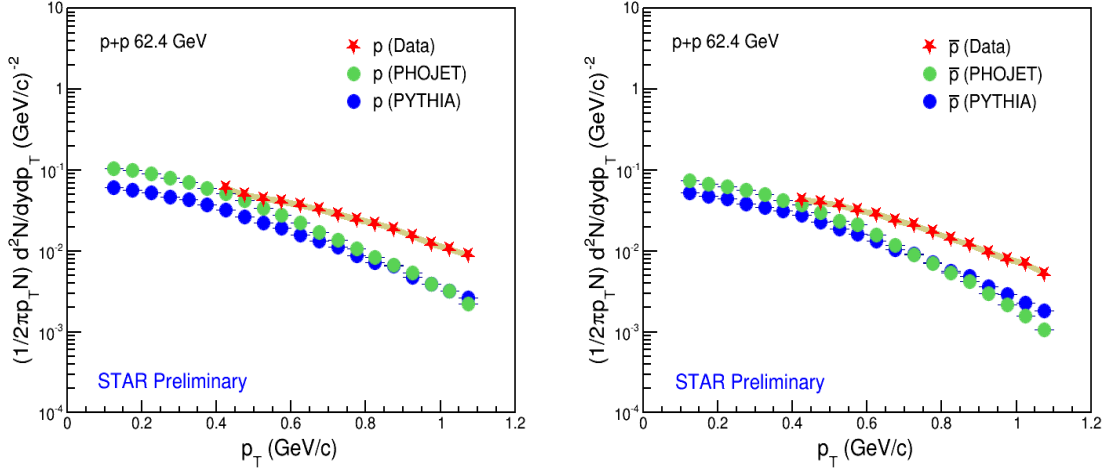


Figure 6.4: Identified transverse momentum spectra for p and \bar{p} (positive particles: are shown in the left panel and negative particles: are shown in the right panel) measured at mid-rapidity ($|y| < 0.1$) for $\sqrt{s} = 62.4$ GeV in $p + p$ collisions. Statistical errors are shown with bars whereas the systematic errors are shown with the shaded band.

6.2.2 Comparison with the PHENIX experiment

Here, we compared the p_T spectra of various charged particles with the similar measurements from the PHENIX experiment [98]. Figure 6.5 shows the comparison of the pion p_T spectra, whereas Fig. 6.6 compares the p_T spectra for K^\pm , p and \bar{p} . In all the plots as shown in Figures 6.5 and 6.6, the blue colored solid star symbols represent the STAR measurements whereas the red colored solid plus symbols represent the PHENIX measurements.

It is also noteworthy to mention here that, the PHENIX measured the inelastic multiplicity while the results presented in this thesis (STAR) quotes the non-single diffractive (NSD) multiplicity. So, the PHENIX results (invariant cross sections) have been properly scaled with σ_{BBC} (13.7 ± 1.5 mb) cross section factor in $p + p$ collisions at $\sqrt{s} = 62.4$ GeV [98] to match with the STAR's invariant yields. The STAR and PHENIX results are consistent with each other, as is evident from the results in Figures 6.5 and 6.6. The STAR data extends the measurements towards the low p_T ;

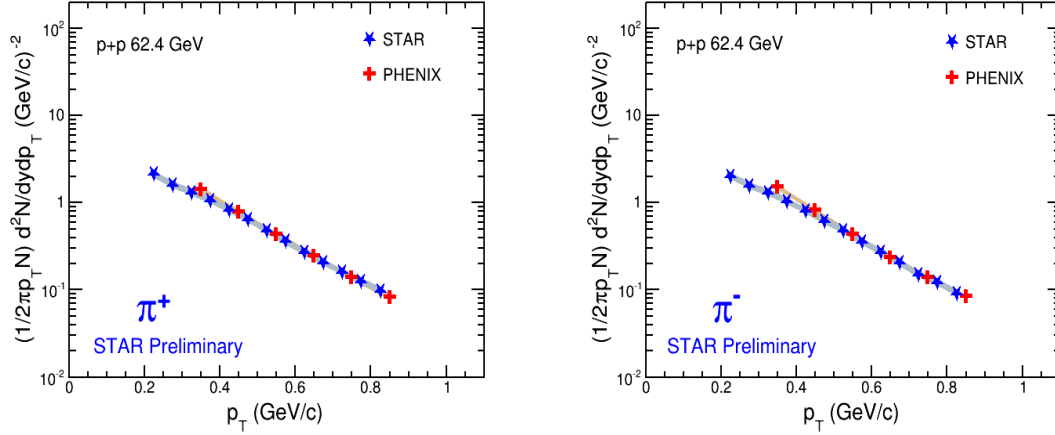


Figure 6.5: *Identified transverse momentum spectra for π^\pm (positive particles: are shown in the left panel and negative particles: are shown in the right panel) measured at mid-rapidity ($|y| < 0.1$) for $\sqrt{s} = 62.4$ GeV in $p + p$ collisions. Statistical errors are shown with bars whereas the systematic errors are shown with the shaded band.*

i.e. $p_T < 0.35$ GeV for pions, $p_T < 0.45$ GeV for kaons, $p_T < 0.65$ GeV for protons as well as antiprotons.

The pion spectra presented for the STAR data are feed-down corrected (as shown in Fig. 6.5), while it is not done for PHENIX measurements. The little discrepancy observed in pion spectra for STAR and PHENIX results, at the low p_T region could be due to the fact that, the PHENIX measurements are not feed-down corrected for weak decays which has a significant contribution at the low p_T region. The little discrepancy in case of proton and antiproton spectra is also observed in the STAR and the PHENIX comparison as is evident from Fig. 6.6, which is due to the fact that, the proton and the antiproton spectra are feed-down corrected in the PHENIX measurements, while for STAR data it is not done. Because weak decay protons (antiprotons) carry most of the parent momentum, their tracks behave as those originating from the primary vertex, resulting in the same reconstruction efficiency for the weak decay and the primary protons (antiprotons) over the measured p_T range. The inclusive protons (antiprotons) closely reflect the total baryon (antibaryon) production [99]. Therefore,

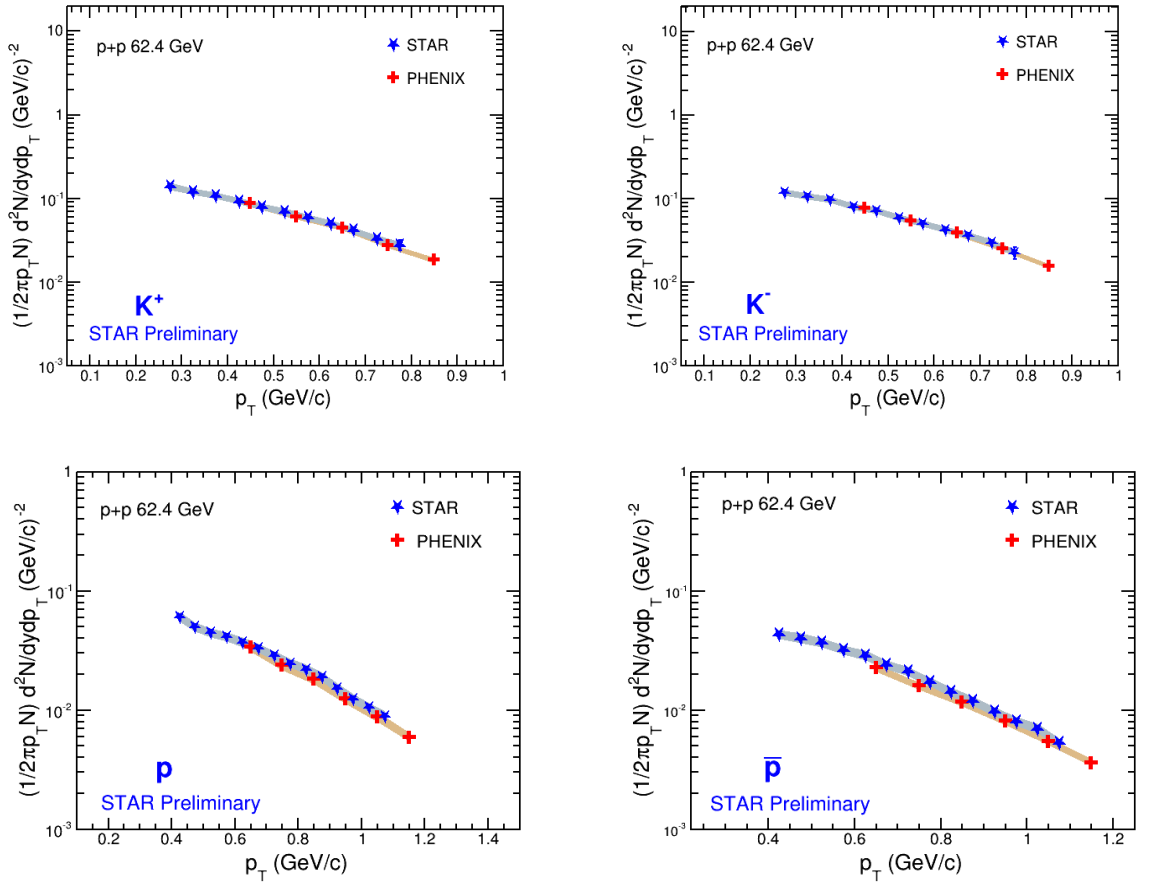


Figure 6.6: Identified transverse momentum spectra for K^\pm , p and \bar{p} (positive particles: are shown in the left panel and negative particles: are shown in the right panel) measured at mid-rapidity ($|y| < 0.1$) for $\sqrt{s} = 62.4$ GeV in $p + p$ collisions. Statistical errors are shown with bars whereas the systematic errors are shown with the shaded band.

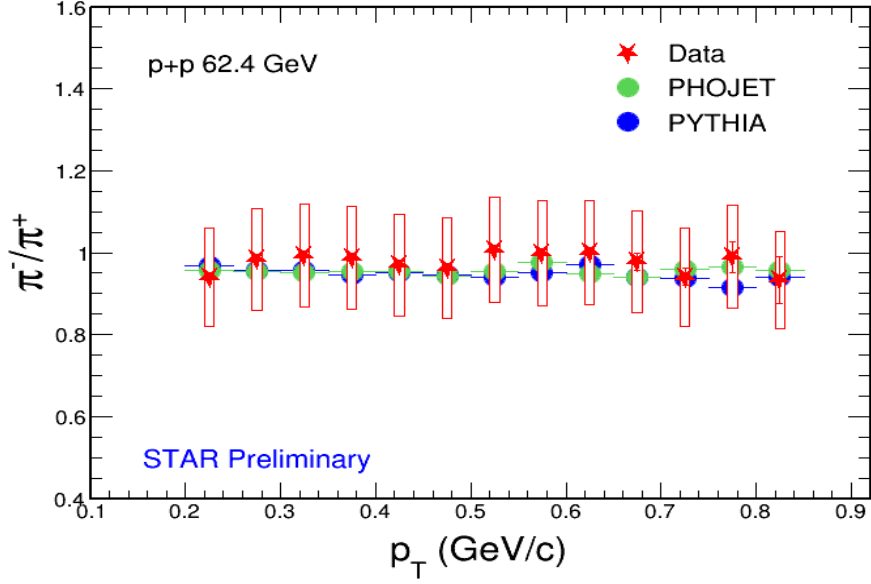


Figure 6.7: Mid-rapidity π^-/π^+ ratio in $p+p$ collision as a function of p_T . Statistical errors are shown with the bars whereas the systematic uncertainties are shown with the vertical boxes.

inclusive proton and antiproton invariant yields are presented in this thesis that are not corrected for weak decays.

6.3 Particle ratios and comparison with models

In this section, various antiparticle to particle as well as unlike particle ratios are presented, these are obtained from their invariant yields and are plotted as a function of their transverse momentum distributions. The comparative study is also presented with the similar results derived from the model calculations. Figure 6.7 shows the antiparticle to particle ratio for the pions along with its comparison with the PYTHIA and PHOJET calculations, whereas Fig. 6.8 shows the similar kind of comparison for antiparticle to particle ratios in case of kaons and protons. The π^-/π^+ and K^-/K^+ ratios show a flat p_T dependence, while the \bar{p}/p ratio shows a weak p_T dependence. The results from the model calculations also follow the similar trend for these like

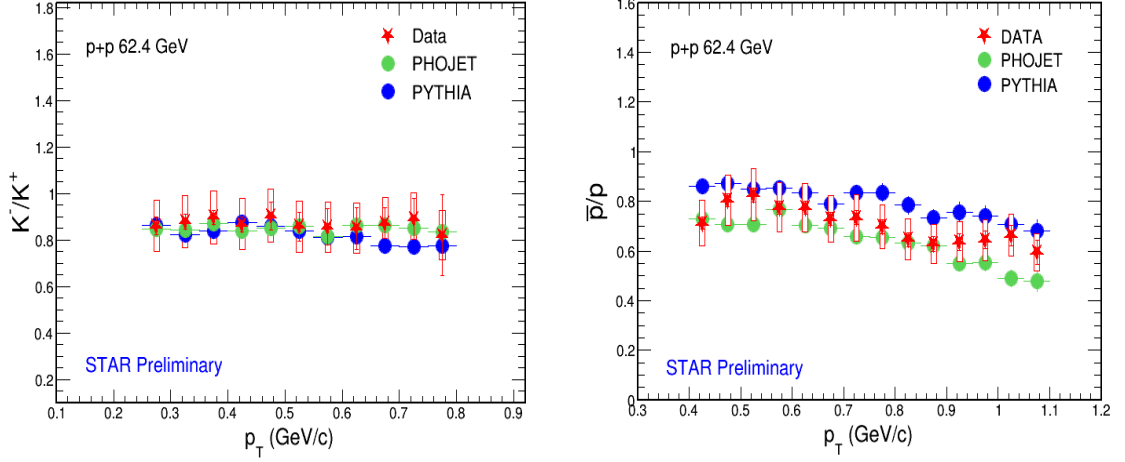


Figure 6.8: Mid-rapidity K^-/K^+ and \bar{p}/p ratios in $p + p$ collision as a function of p_T . Statistical errors are shown with the bars whereas the systematic uncertainties are shown with the vertical boxes. K^-/K^+ ratio is shown in the left panel and \bar{p}/p ratio is shown in the right panel.

particle ratios. The π^-/π^+ ratio is almost unity, the K^-/K^+ ratio is in the range $\sim 0.85 - 0.90$, and the \bar{p}/p ratio is in the range $\sim 0.65 - 0.80$, within the measured p_T range.

The strange to non-strange particle production is studied with the help of K/π ratios as a function of p_T . Figure 6.9 shows the unlike particle ratios for the K^+/π^+ and K^-/π^- along with their comparison with the model calculations for the similar results. Baryon to meson particle production is also studied with the $p(\bar{p})/\pi^+(\pi^-)$ ratios as function of p_T . The p/π^+ and \bar{p}/π^- ratios are presented as a function of p_T along with their comparison with the model calculations as shown in Fig. 6.10.

Within the limit of measurements in p_T for the present thesis work, all the results for the unlike particle ratios show an increase with the increasing p_T . The model calculations also seem to exhibit the similar behavior within the same range of p_T .

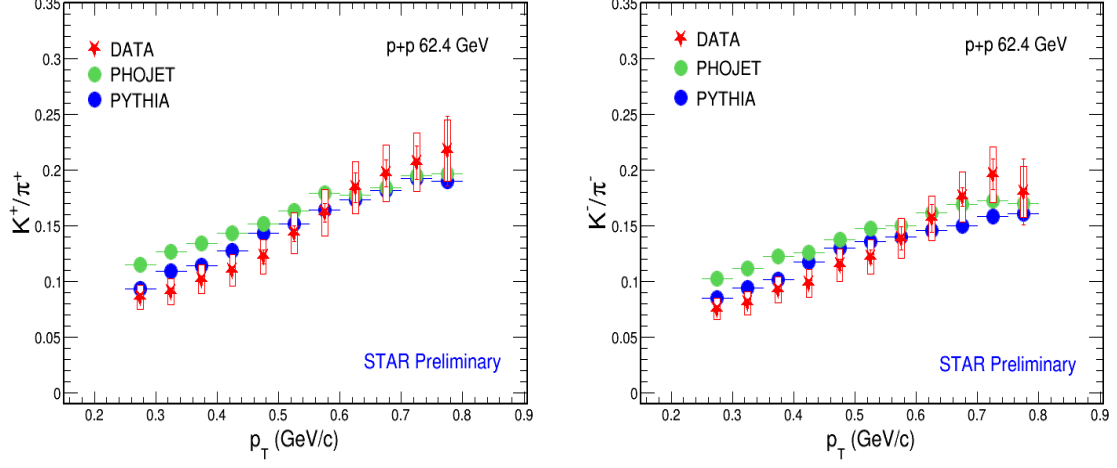


Figure 6.9: Mid-rapidity K^+/π^+ and K^-/π^- ratios in $p + p$ collision as a function of p_T . Statistical errors are shown with the bars whereas the systematic uncertainties are shown with the vertical boxes. K^+/π^+ ratio is shown in the left panel and K^-/π^- ratio is shown in the right panel.

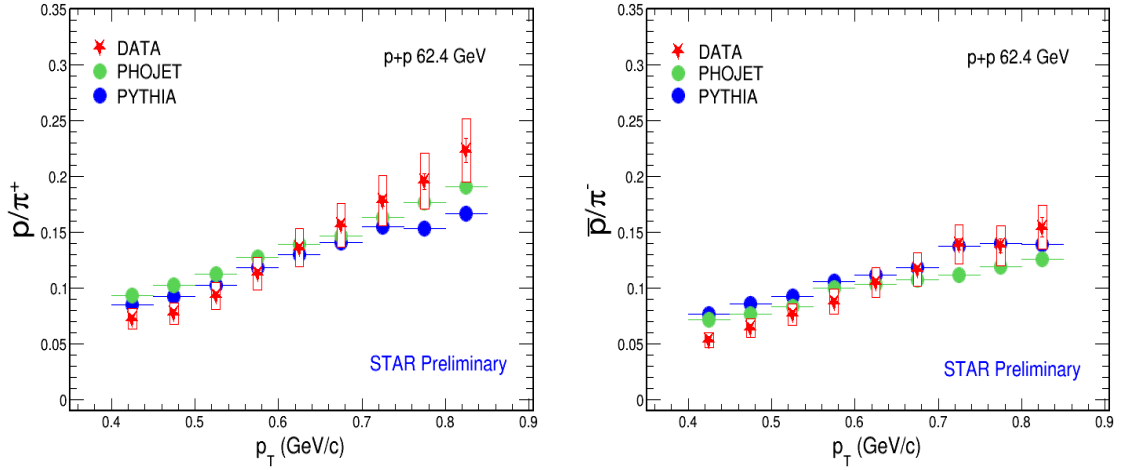


Figure 6.10: Mid-rapidity p/π^+ and \bar{p}/π^- ratios in $p + p$ collision as a function of p_T . Statistical errors are shown with the bars whereas the systematic uncertainties are shown with the vertical boxes. p/π^+ ratio is shown in the left panel and \bar{p}/π^- ratio is shown in the right panel.

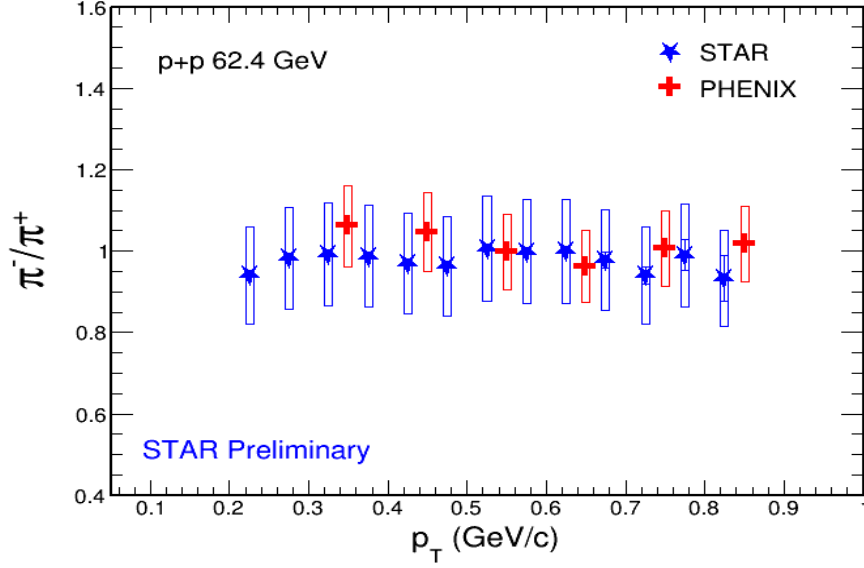


Figure 6.11: Mid-rapidity π^-/π^+ ratio in p+p collision as a function of p_T . Statistical errors are shown with the bars whereas the systematic uncertainties are shown with the vertical boxes.

6.4 Particle ratios and comparison with PHENIX

In this section, the comparative study for the antiparticle to particle as well as unlike particle ratios as a function of p_T is presented with the similar measurements from the PHENIX experiment. Figure 6.11 shows the antiparticle to particle ratio for the pions along with its comparison with the similar result from the PHENIX measurements, whereas Fig. 6.12 shows the similar kind of comparison for antiparticle to particle ratios in case of kaons and protons. The STAR data is represented by the solid star symbols whereas the PHENIX data points are shown with the solid plus symbols.

The π^-/π^+ and K^-/K^+ ratios show a flat p_T dependence, while the \bar{p}/p ratio shows a weak p_T dependence. Inside the limits of measured p_T region, the results are consistent with the PHENIX experiment. The comparative study focussing on the strange to non-strange as well as baryon to meson particle production is also carried out with the PHENIX data. Figure 6.13 shows the unlike particle ratios for the K^+/π^+ and K^-/π^- along with the PHENIX data for similar unlike ratios. The

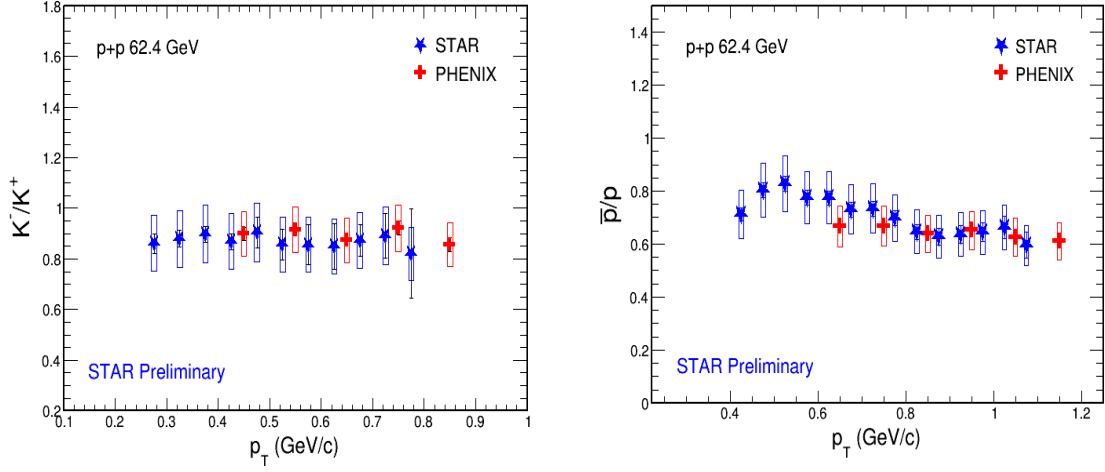


Figure 6.12: Mid-rapidity K^-/K^+ and \bar{p}/p ratios in $p + p$ collision as a function of p_T . Statistical errors are shown with the bars whereas the systematic uncertainties are shown with the vertical boxes. K^-/K^+ ratio is shown in the left panel and \bar{p}/p ratio is shown in the right panel.

p/π^+ and \bar{p}/π^- ratios are also presented as a function of p_T along with the PHENIX data as shown in Fig. 6.14. From these results, it is clear that, the different particle ratios as a function of p_T measured in STAR are in agreement with the previous measurements with PHENIX.

6.5 Particle yield per unit rapidity

The particle yield per unit rapidity (dN/dy) and the average transverse momentum ($\langle p_T \rangle$) are extracted from the measured spectra and also extrapolated outside the measured p_T region. The extrapolation is based on the different functional forms which are presented in detail in the Appendix C. The dN/dy is calculated for π^\pm , K^\pm , p and \bar{p} by integrating their corresponding spectra in the measured range and by taking the integral of the fit function in the extrapolated region. Different fit functions are used to obtain the dN/dy values which depends directly on the spectral shapes of individual particle. The low- p_T as well as high- p_T extrapolation region are different

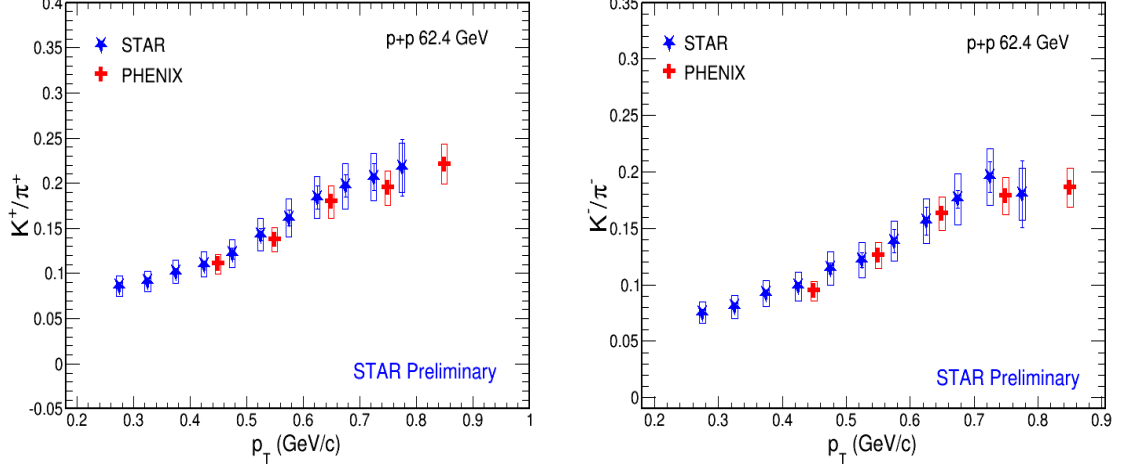


Figure 6.13: Mid-rapidity K^+/π^+ and K^-/π^- ratios in $p + p$ collision as a function of p_T . Statistical errors are shown with the bars whereas the systematic uncertainties are shown with the vertical boxes. K^+/π^+ ratio is shown in the left panel and K^-/π^- ratio is shown in the right panel.

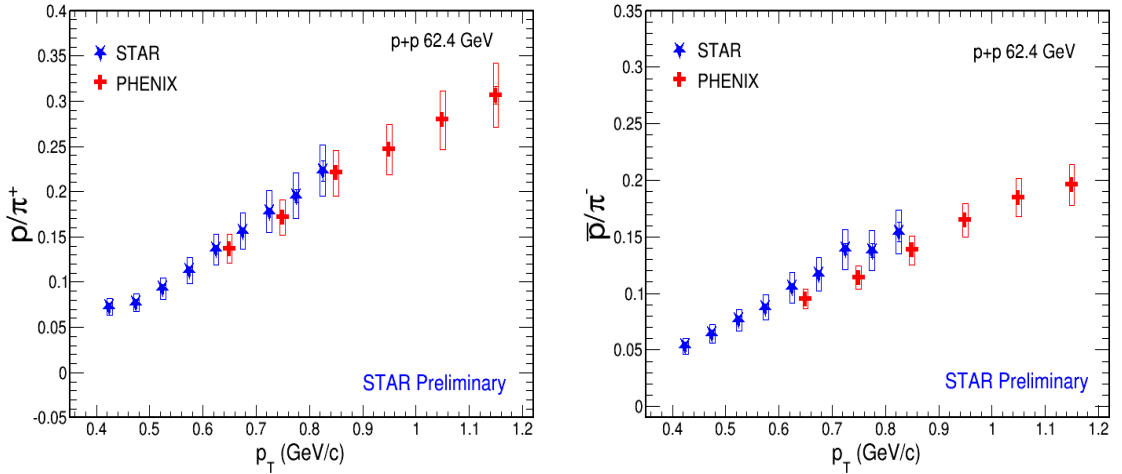


Figure 6.14: Mid-rapidity p/π^+ and \bar{p}/π^- ratios in $p + p$ collision as a function of p_T . Statistical errors are shown with the bars whereas the systematic uncertainties are shown with the vertical boxes. p/π^+ ratio is shown in the left panel and \bar{p}/π^- ratio is shown in the right panel.

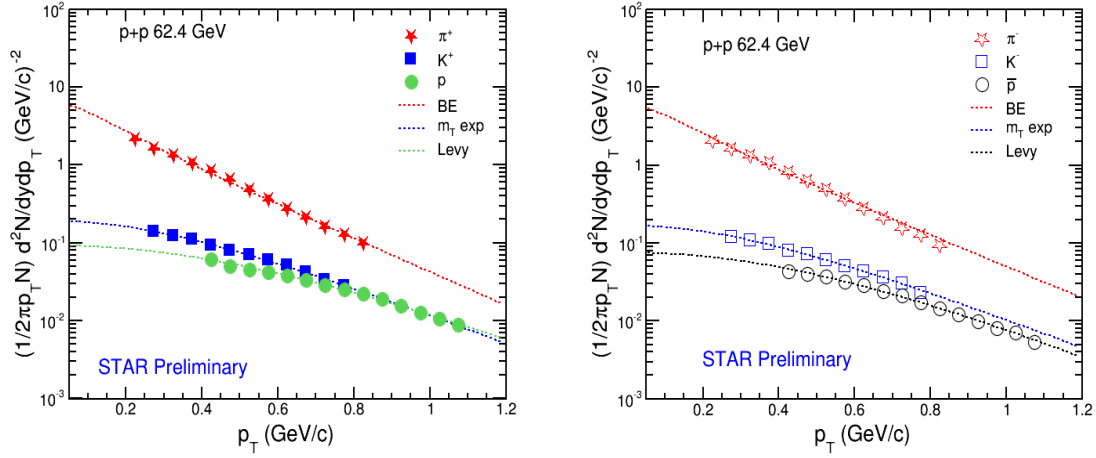


Figure 6.15: Identified transverse momentum spectra for π^\pm , K^\pm , p and \bar{p} (positive particles: filled symbols in left panel and negative particles: open symbols in right panel) measured at mid-rapidity ($|y| < 0.1$) $\sqrt{s} = 62.4$ GeV in $p + p$ collisions. Errors are both statistical and systematic added in quadrature. The size of the errors are smaller than the symbol size. Different fits functions used to obtain the dN/dy and the $\langle p_T \rangle$ are also shown.

for individual particles. The low- p_T extrapolation contribution to the dN/dy value is $\sim 25\text{-}40\%$, whereas the high- p_T contribution is low and is found to be $\sim 1\text{-}5\%$. The value obtained for the dN/dy for various particles is as per the following equation:

$$dN/dy = I_{low} + I_{hist} + I_{high}, \quad (6.2)$$

where,

- I_{hist} denotes the integral obtained from the histogram in the measured p_T region,
- For pions: $I_{low}(p_T) = \int_{0.0}^{0.20} f(p_T) dp_T$, and $I_{high}(p_T) = \int_{0.851}^{10.0} f(p_T) dp_T$,
- For kaons: $I_{low}(p_T) = \int_{0.0}^{0.249} f(p_T) dp_T$, and $I_{high}(p_T) = \int_{0.801}^{10.0} f(p_T) dp_T$,
- For protons: $I_{low}(p_T) = \int_{0.0}^{0.399} f(p_T) dp_T$, and $I_{high}(p_T) = \int_{1.101}^{10.0} f(p_T) dp_T$,
- the functional form $f(p_T)$ used is different for different particles. For π^\pm , the Bose-Einstein function is used, for K^\pm , the m_T exponential function is used,

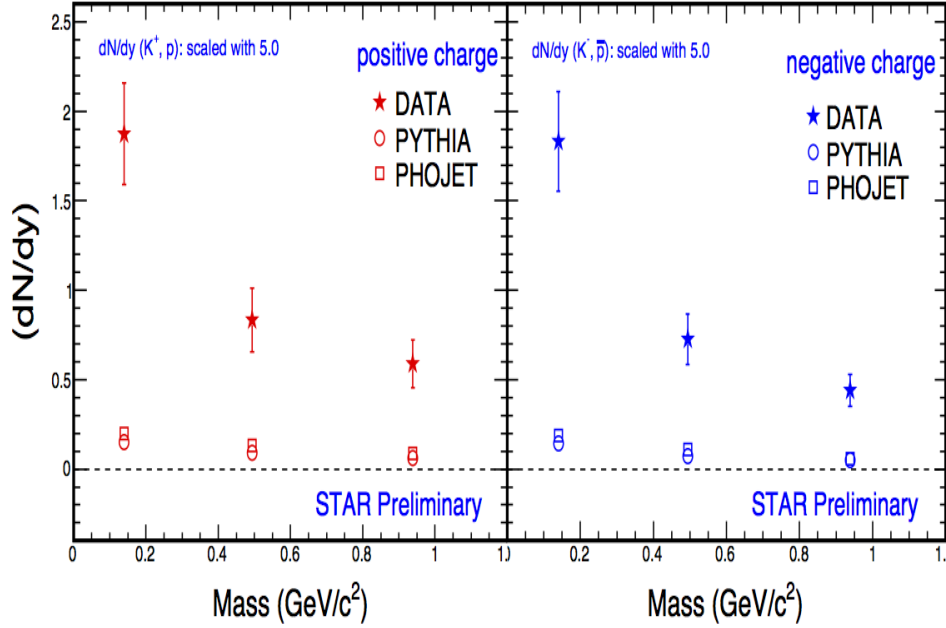


Figure 6.16: The dN/dy measurements from the STAR experiment at $\sqrt{s} = 62.4$ GeV in $p+p$ collisions. The results are also shown for dN/dy calculated in the model calculations.

and the Tsallis (Levy) function is used for p and \bar{p} . The various fit functions used to obtain dN/dy are given in the Appendix C and are shown in Fig. 6.15.

The statistical errors in the extrapolated regions are assumed to be fully correlated with the statistical error in the measured region and therefore, the total statistical error in the dN/dy are calculated using the equation given below:

$$\sigma_{dN/dy} = \sigma_{I_{low}} + \sigma_{I_{hist}} + \sigma_{I_{high}}, \quad (6.3)$$

where, $\sigma_{I_{low}}$, $\sigma_{I_{high}}$, are calculated by using mathematical function defined in the TMath class of ROOT package [100], whereas $\sigma_{I_{hist}}$ is the error associated with the histogram yield.

The dN/dy is also obtained by integrating their value using different fit functions for a given particle type. The default (best) fit functions are shown in Fig. 6.15.

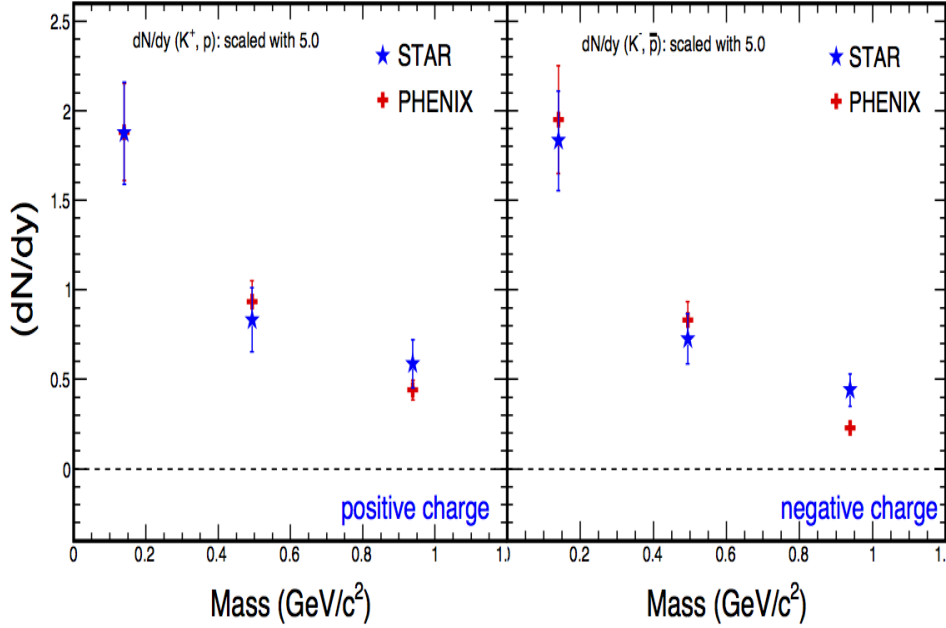


Figure 6.17: The dN/dy measurements from the STAR experiment at $\sqrt{s} = 62.4$ GeV in $p + p$ collisions. The results are also shown for dN/dy measurements in the PHENIX experiment.

The difference obtained in the value of the dN/dy obtained in comparison to the default value of dN/dy is included in the systematic uncertainties on the value of dN/dy . The dN/dy for particles and antiparticles as a function of particle's mass are shown in Fig. 6.16. From Fig. 6.16, it is evident that dN/dy decreases as a function of particle mass. The results are compared with the dN/dy obtained in the model calculations which clearly underpredict the data. The data points are shown by the solid markers whereas the model calculations are represented by the open markers as shown in Fig. 6.16. We have also compared our dN/dy measurements at STAR with those at PHENIX as shown in Fig. 6.17 and they are in good agreement. The PHENIX data obtained from their paper [98] are scaled with total inelastic cross section at $\sqrt{s} = 62.4$ GeV to compare with the STAR's NSD data.

6.6 Mean transverse momentum $\langle p_T \rangle$

The mean transverse momentum $\langle p_T \rangle$ is extracted from the different fit functions which were discussed in the previous section. The formula employed for evaluating the $\langle p_T \rangle$ is as given below:

$$\langle p_T \rangle = \frac{\int_0^\infty \frac{1}{2\pi p_T} \frac{dN}{dy dp_T} 2\pi p_T^2 dp_T}{\int_0^\infty \frac{1}{2\pi p_T} \frac{dN}{dy dp_T} 2\pi p_T dp_T} = \frac{\int_0^\infty p_T (2\pi p_T) f(p_T) dp_T}{\int_0^\infty (2\pi p_T) f(p_T) dp_T}, \quad (6.4)$$

where, $f(p_T)$ is the fit function used to fit the p_T distribution and is dependent on the type of the particle whose $\langle p_T \rangle$ is to be calculated. The $\langle p_T \rangle$ is also measured by using different fit functions and the difference emerging in their values is expressed as the systematic uncertainties. The $\langle p_T \rangle$ for both particles and antiparticles as a function of particle's mass are shown in Fig. 6.18. The results are also compared with the $\langle p_T \rangle$ obtained in the model calculations (as shown in Fig. 6.18) as well as with those obtained from the PHENIX experiment (as shown in Fig. 6.19). The data points are shown by the solid symbols whereas the model calculations are represented by the open symbols as shown in Fig. 6.18. It is observed from Figures 6.18 and 6.19 that, the $\langle p_T \rangle$ increases as a function of increasing particle mass. Our $\langle p_T \rangle$ measurements are found to be consistent with those of the PHENIX, whereas the model calculations underpredict the data. The error bars in each data points in both dN/dy and $\langle p_T \rangle$ calculations are the quadratic sum of the statistical and systematic errors.

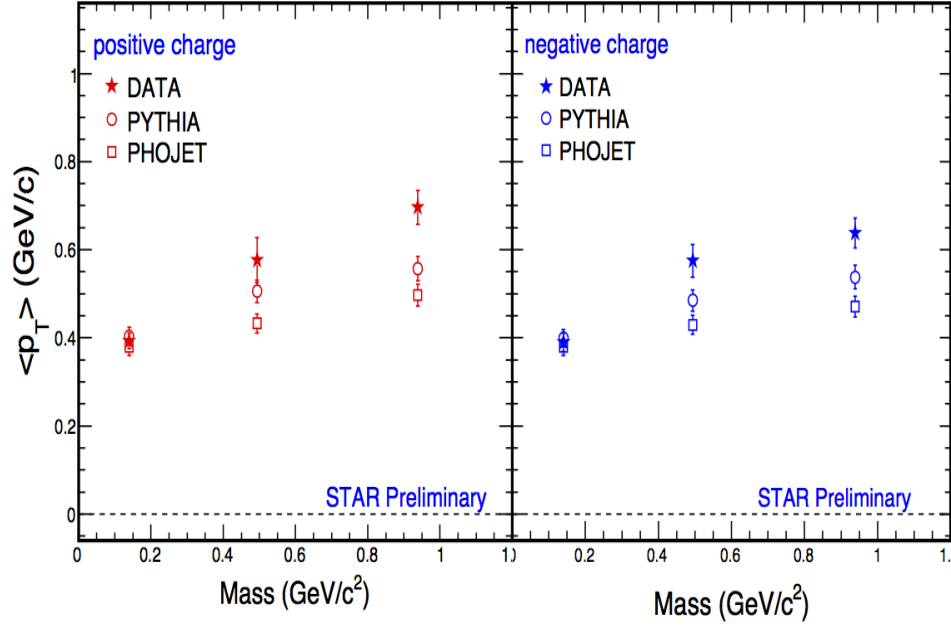


Figure 6.18: The $\langle p_T \rangle$ measurements from the STAR experiment at $\sqrt{s} = 62.4$ GeV in $p + p$ collisions. The results are also shown for $\langle p_T \rangle$ calculated in the model calculations.

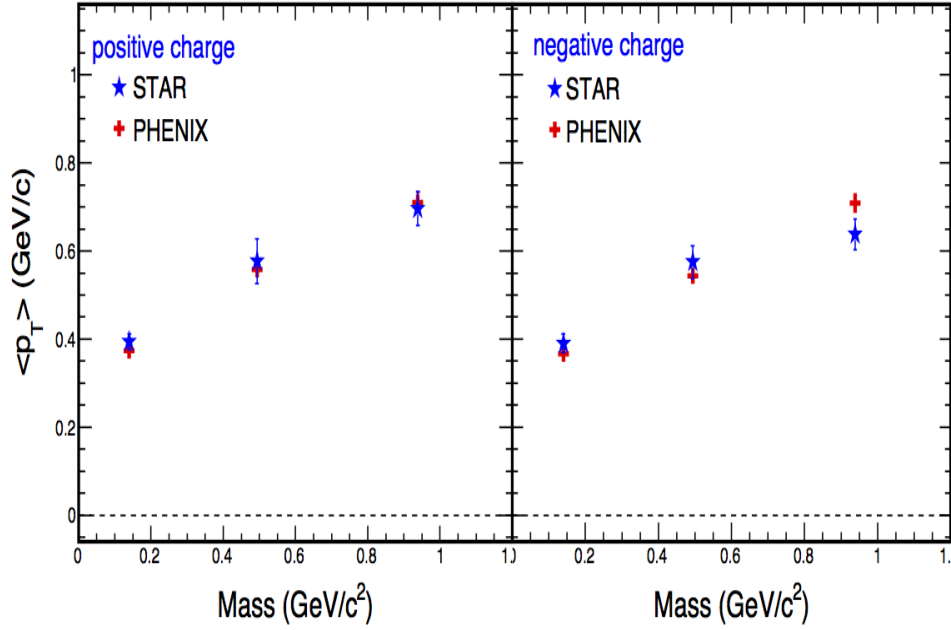


Figure 6.19: The $\langle p_T \rangle$ measurements from the STAR experiment at $\sqrt{s} = 62.4$ GeV in $p + p$ collisions. The results are also shown for $\langle p_T \rangle$ obtained in the PHENIX experiment.

Chapter 7

Summary and Conclusions

7.1 Summary

In this thesis work, identified particle production for π^\pm , K^\pm , p and \bar{p} are presented at mid-rapidity for $p + p$ collisions in $\sqrt{s} = 62.4$ GeV. The data analysed for present work is from the STAR experiment at RHIC. The main sub-detector used for the given measurements is the TPC. The charged particles are identified using the specific ionization energy loss (dE/dx) method in STAR's TPC detector. The raw particle yields are obtained for all the charged particles using this method. Different corrections are done to the raw yields to obtain the corrected invariant yields. The correction factors are obtained from the embedding and Monte Carlo simulation. The final corrected spectra at mid-rapidity ($|y| < 0.1$) are then presented for π^\pm , K^\pm , p and \bar{p} for minimum bias events.

The inclusive particle yield (dN/dy) and the mean p_T measured at mid-rapidity are also calculated for each identified particle spectrum using data in the measured p_T region and extrapolated in the unmeasured p_T region. For the extrapolation different parameterizations are used, Bose-Einstein function for pions, m_T exponential function for kaons and Levy function for protons/antiprotons. Various particle ratios are

calculated from the invariant yields of the identified particles. The various antiparticle to particle ratios (π^-/π^+ , K^-/K^+ & \bar{p}/p) and unlike particle ratios (K^\pm/π^\pm , $p(\bar{p})/\pi^\pm$) are presented as a function of transverse momentum of the identified charged particles. The similar results are obtained for transverse momentum spectra, particle ratios, dN/dy and mean p_T for the pions, kaons, protons/antiprotons from model calculations at same center of mass energy. The experimental data are compared with PYTHIA and PHOJET model calculations [29, 30]. The results are also compared with the published PHENIX measurements [98].

7.2 Conclusions

This thesis work presents the first measurement of identified charged hadrons (π^\pm , K^\pm , p and \bar{p}) at $\sqrt{s} = 62.4$ GeV in STAR experiment to investigate the p_T spectra and the particle ratios at mid-rapidity in $p + p$ collisions. Charged hadrons are identified by the ionization energy loss method and their raw yields are obtained from multi-gaussian fits to the $Z - distributions$. These raw yields are further corrected for tracking efficiency, detector acceptance, feed-down from the weak decays and background particles from the beam-pipe interactions. These corrections are obtained from embedding and simulation techniques involving GEANT software for reproducing the STAR detector response.

The corrected invariant differential yields are studied as a function of the transverse momentum spectra of the various identified charged particles at the low p_T region. The spectral shapes observed provides a nice exponential behavior for both particles and anti-particles. The slopes of the spectra for the π^\pm are steeper than K^\pm , which in turn are steeper than protons and antiprotons. The results for p_T spectra have been compared with the calculations from models. The models underestimate the data but they fairly reproduce the shapes of the spectra, though the effect gets

less significant with the increase in p_T . These results can be used for a better understanding of the hadron production mechanism in $p + p$ interactions at $\sqrt{s} = 62.4$ GeV and could further be useful in constraining the parameters of these models.

The similar measurements of p_T spectra for identified charged particles at $\sqrt{s} = 62.4$ GeV in $p + p$ collisions for STAR experiment are also compared with those for the PHENIX experiment and they are in good agreement. Thus, the results presented in this thesis extends the spectra measurement of π^\pm , K^\pm , p and \bar{p} towards the low p_T region.

The comparison is also presented for antiparticle to particle ratios and unlike particle ratios with the similar results derived from the model calculations and also with those from the PHENIX experiment. The π^-/π^+ and K^-/K^+ ratios show a flat p_T dependence, while the \bar{p}/p ratio shows a weak p_T dependence. Within the limits of measured p_T region, the results are consistent with the model calculations and with those of the PHENIX experiment. The π^-/π^+ ratio is almost unity, the K^-/K^+ ratio is in the range $\sim 0.85 - 0.90$, and the \bar{p}/p ratio is in the range $\sim 0.65 - 0.80$, within the measured p_T region. The strange to non-strange as well as the baryon to meson particle production is also investigated with the K^\pm/π^\pm and $p(\bar{p})/\pi^\pm$ respectively. These unlike particle ratios show an increasing trend with the increase in p_T . Within the errors, the results for these unlike particle ratios are again consistent with both model calculations and PHENIX measurements.

The particle yield per unit rapidity (dN/dy) and the average transverse momentum ($\langle p_T \rangle$) are also obtained. These observables are compared with the results from the similar calculations using models and also with the PHENIX measurements. The dN/dy shows a decreasing trend with the increasing mass of the particles whereas the mean p_T reveals the opposite trend. The similar trend is observed in the model calculations, though it underestimate the data. While the STAR data are in good

agreement with the results from PHENIX within the error bars. In $p + p$ and $d + Au$ collisions, the increase in $\langle p_T \rangle$ as a function of $dN_{ch}/d\eta$, is expected to reflect the contribution from the semi-hard scatterings and multi-parton interactions [101].

In gist, the measurements presented in this thesis work provide an important baseline for the heavy ion collisions measurement at RHIC. The measurements of the transverse momentum spectra of the identified particles would be very crucial in investigating the partonic energy loss in the medium by constructing the Nuclear Modification Factor (R_{AA}) [52]. With the results presented at low p_T for the various particle ratios together with the dN/dy measurements, when extended towards high p_T could give insight into the important production mechanism at mid-rapidity. The high-precision measurements of identified charged hadron p_T spectra and particle ratios reported here, covering the low p_T measurements in the mid-rapidity region, give useful information for the fine tuning of the QCD inspired models and better understanding of the soft particle production mechanisms at $\sqrt{s} = 62.4$ GeV. The STAR data are consistent with the PHENIX measurements and furthermore it extends towards low p_T . Finally, the results presented for the various particle ratios when investigated from the perspective of thermal models [102, 103] could provide important parameters like kinetic and chemical freeze-out temperatures, which could further help in understanding the process of hadronization.

Appendix A

Relativistic Kinematics

In relativistic heavy-ion collisions and many other high energy reaction processes, it is convenient to use kinematic variables which are Lorentz invariant under Lorentz boost. Throughout this thesis, the standard high energy physics notations and natural units are used.

A.1 Mandelstam Variables

A particle with energy (E), the rest mass (m_0), and the momentum (p), is described by its four-momentum (P) which is given by,

$$P = (E, p) = (E, p_x, p_y, p_z), \quad (\text{A.1})$$

The Mandelstam variables which are relativistic invariants are used to describe the reactions:

$$1 + 2 \rightarrow 3 + 4, \quad (\text{A.2})$$

Such reactions of the highly energetic particles can be defined by different Mandelstam variables signifying the kind of interaction they belong to. They are given as follows:

$$s = (P_1 + P_2)^2 = (P_3 + P_4)^2, \quad (\text{A.3})$$

$$t = (P_1 - P_3)^2 = (P_2 - P_4)^2, \quad (\text{A.4})$$

$$u = (P_1 - P_4)^2 = (P_2 - P_3)^2, \quad (\text{A.5})$$

here P_1, P_2 are the four-momenta of the incoming particles, whereas P_3, P_4 are those of the outgoing particles. While high energy $p + p$ collisions are not simple two-particle process such as this, the Mandelstam variable (s) is generalised to refer to the momenta of the incoming protons. Thus, \sqrt{s} is equal to the collision energy in the $p + p$ center of mass frame. When describing the heavy ion collisions, the energy is typically quantified by the nucleon-nucleon center of mass energy $\sqrt{s_{NN}}$. Thus, in the above equations, the variable s represents the square of the total energy in the center of mass frame. The variable t is the square of the momentum transfer in its reaction between 1 to 3 and 2 to 4, whereas the u is the square of the momentum transfer in its reaction between 1 to 4 and 2 to 3.

A.2 Rapidity

The momentum of a particle is divided into its longitudinal part (p_z) and the transverse part (p_T). In terms of energy (E) and longitudinal momentum (p_z), we can also define another kinematic variable commonly used to characterize the motion of a particle and is known as *rapidity*, which is given as :

$$y = \frac{1}{2} \ln \left(\frac{E + p_z}{E - p_z} \right), \quad (\text{A.6})$$

However, at ultra-relativistic limits, the rapidity variable is replaced by the pseudo-rapidity which does not depend on the particle's mass rather it depends on its total momentum (p) and also on its emission angle θ with the beam axis. It is represented by the letter η and is given as:

$$\eta = \frac{1}{2} \ln \left(\frac{p + p_z}{p - p_z} \right), \quad (\text{A.7})$$

and, in terms of θ , it is given by:

$$\eta = -\ln \left(\tan \frac{\theta}{2} \right), \quad (\text{A.8})$$

Appendix B

Lund string fragmentation model

The Lund string fragmentation model (which forms a base of PYTHIA) is briefly discussed here. The main idea of this model is, the creation of a color field between a quark and an antiquark when particles move in opposite directions. This field can be approximated by a field with a linear potential (color string). Three different aspects of this model are discussed below:

B.1 Meson production

Quarks from the vacuum state can tunnel via the linear potential creating quark-antiquark pairs ($q_i\bar{q}_i$) at vertices as shown in Fig. B.1. The tunneling probability is given by $\exp(-\pi m_T^2/\kappa)$ where $\kappa \approx 1$ GeV/fm and m_T ($\sqrt{p_T^2 + m^2}$) is the transverse mass of the quarks. The generation of p_T (here momentum perpendicular to the axis of the initial pair) of the produced partons is done using a Gaussian distribution. The tunnelling mechanism suppresses the production of heavy quarks due to dependence of the probability on the mass (ratio of the probabilities to produce quarks is $u:d:s:c \approx 1 : 1 : 0.3 : 10^{-11}$). The pair masses are not precisely known, so that the suppression of the strange quark production is a model parameter (set to 0.3 by default in PYTHIA).

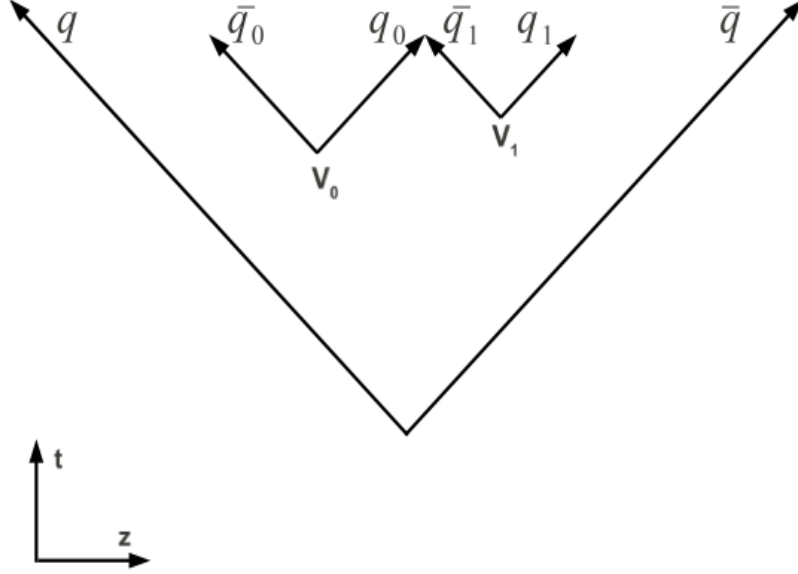


Figure B.1: *Quark and antiquark space-time trajectories in the Lund string fragmentation model. The two vertices (V_0 and V_1), where new quark-antiquark pairs are produced are also shown.*

A quark can join with an antiquark from the neighbouring vertex and form a meson. The created meson will pick up fraction z of the available $E + p_z$. The distribution of z is given by the Lund symmetrical fragmentation function [104]:

$$f(z) \propto \frac{1}{z} z^{a_\alpha} \left(\frac{1-z}{z} \right)^{a_\beta} \exp \left(\frac{-bm_T^2}{z} \right), \quad (\text{B.1})$$

where a_α , a_β and b are the free parameters. This function is a consequence of the assumption that there is no time ordering of the vertices. The produced mesons have one out of six combinations of spin and internal orbital angular momentum. The probabilities to obtain each of these are model parameters.

B.2 Baryon production

To produce baryons in the Lund string fragmentation model, two mechanisms are used: a diquark production model and the popcorn model. The main assumption

of the diquark production model is that instead of a quark (antiquark) a pair of antiquarks (quarks) in a color triplet state is produced. This pair can connect with the neighbouring parton and form a baryon. This mechanism is based on the observation that the color triplet states of two antiquarks (quarks) in the color field can be considered as a quark (antiquark). The probabilities, to create a diquark pair rather than an antiquark, the extra suppression factor for production of pairs with a strange quark and the relative contributions of the spin states of the pairs are input parameters of the diquark production model.

The popcorn model uses fluctuations of the color field to produce quark-antiquark pairs with a different colour than the initial pair. For example if the initial pair is red-antired the standard fragmentation produces red-antired pairs, but the fluctuations can produce a green-antigreen pair. In this case both quarks (antiquarks) move towards each other (they are in a color triplet state), producing a color field with a blue-antiblue configuration. This string fragments as for a blue-antiblue initial pair, producing a baryon-meson to meson-antibaryon system. In most cases baryon-antibaryon and baryon-meson-antibaryon systems are produced (the relative contribution is a model parameter), since including the production of an additional meson introduces an extra suppression due to the increase of the transverse mass of the system. The strangeness production is also a model parameter [95, 96].

B.3 Multiparton interactions

In a full simulation of $p + p$ collisions the situation is more complex because a multiparton system is produced. Strings are created by quark-gluon-antiquark systems. The breakup of the string is done by a breakup of each quark-gluon piece according to the standard procedure but additional kinematic conditions are introduced to ensure that the produced hadrons are on mass shell. In general the whole event is divided

into groups of partons which are in a color singlet state.

Appendix C

Fitting Spectra

As the p_T distributions are not measured over the full range $(0 - \infty)$, the spectra cannot be directly integrated in p_T in order to obtain the total invariant yield in unit rapidity. Rather, a fit must be made from a theoretically motivated function as per the relation:

$$\frac{1}{2\pi p_T} \frac{d^2 N}{dy dp_T} = f(p_T), \quad (\text{C.1})$$

Here, left side of the eq. [C.1](#) represents the invariant yield evaluated for a given rapidity interval and is considered equivalent to a theoretical function best describing the invariant yield of a given particle type. This function can then be integrated in order to deduce the actual yield in that rapidity interval as per the equation:

$$\frac{dN}{dy} = \int \frac{d^2 N}{dy dp_T} dp_T = \int 2\pi p_T dp_T f(p_T), \quad (\text{C.2})$$

Different particle species will fit better with different functions. An optimum fit should be found by taking into account the χ^2 of the fit, the nature of the particle type, the p_T coverage and the errors of the fit parameters. If the fit parameters themselves are completely out of meaningful ranges, the fit should not be used. The work presented in this thesis involve the use of different functions for different particle

species. In addition, different fit functions are used for a single particle type to evaluate the systematic error involved due to different functions used for the measurements.

C.1 Bose-Einstein function

The Bose-Einstein distribution is found to describe the pion spectra to a good approximation and is therefore used in the present thesis work to fit the pion spectra to extrapolate the yield in the unmeasured region of the p_T spectra. The functional form used for this parametrization is:

$$\frac{1}{2\pi p_T} \frac{d^2 N}{dy dp_T} = A \frac{1}{e^{\frac{m_T}{T}} - 1}, \quad (\text{C.3})$$

where, m_T ($\sqrt{p_T^2 + m^2}$) is the transverse mass of the pion and T is the inverse slope parameter which gives the effective temperature of the system formed when elastic scattering among the particles cease.

C.2 Exponential in p_T

A p_T exponential is a simplest fit function derived from a thermal source. Exponential spectra are seen even in the e^+e^- collisions, which is believed to be “non-thermal” in an ordinary sense. A possible explanation is that the exponential behavior is related to the statistical nature of fragmentation. The proton spectra are fitted with this exponential function in this thesis in order to obtain the systematic in case of dN/dy and mean p_T and the functional form used for this purpose is given as:

$$\frac{1}{2\pi p_T} \frac{d^2 N}{dy dp_T} = A e^{\frac{-p_T}{T}}, \quad (\text{C.4})$$

C.3 Exponential in m_T

An exponential in m_T usually gives better fits than an exponential in p_T , as it takes into account different masses of charged hadrons into account and therefore behaves more realistically at low p_T . It will consistently fit the low p_T region of most identified particle distributions with a low χ^2 . In this thesis work, kaons are fit with an exponential in m_T and the functional form used is as follows:

$$\frac{1}{2\pi p_T} \frac{d^2 N}{dy dp_T} = A e^{\frac{-m_T}{T}}, \quad (\text{C.5})$$

C.4 Boltzmann function

The Boltzmann distribution is a classical thermal distribution that fits the proton spectra to a fairly good approximation. The functional form used to obtain the systematic in this thesis is given as:

$$\frac{1}{2\pi p_T} \frac{d^2 N}{dy dp_T} = A m_T e^{\frac{-m_T}{T}}, \quad (\text{C.6})$$

C.5 Power law

The high p_T region of the spectrum is dominated by the semi-hard and hard scattering processes, which is believed to cause a power law tail. So, the high p_T spectrum is well explained by this statistical function. Though, this function is not exclusively used in this thesis work for fitting any particle species, yet it plays an important role being a part of the Tsallis function. The functional form of this fit function is:

$$\frac{1}{2\pi p_T} \frac{d^2 N}{dy dp_T} = A \left(1 + \frac{p_T}{qT} \right)^{-q}, \quad (\text{C.7})$$

C.6 Tsallis (Levy) function

This distribution function has been used in this thesis work to explain the proton, antiproton spectra to obtain their integrated yields as well as for other particle species to obtain the systematic for the dN/dy and mean p_T . It nicely explain the low p_T part by including the exponential function and high p_T part by including the power law in its complete definition. The functional form for the Tsallis function used in this thesis work is given as [98]:

$$\frac{1}{2\pi p_T} \frac{d^2 N}{dy dp_T} = \frac{dN}{dy} \times \frac{(q-1)(q-2)}{2\pi q T [qT + m(q-2)]} \times \left(1 + \frac{m_T - m}{qT}\right)^{-q}, \quad (\text{C.8})$$

where, unlike other distribution functions it has three free parameters, dN/dy , inverse slope parameter (T) and the exponent (q).

Appendix D

Tables

$p_T(\text{GeV}/c)$	π^+	π^-
0.225	$2.169 \pm 0.015 \pm 0.195$	$2.040 \pm 0.014 \pm 0.183$
0.275	$1.626 \pm 0.008 \pm 0.146$	$1.599 \pm 0.008 \pm 0.143$
0.325	$1.331 \pm 0.007 \pm 0.119$	$1.322 \pm 0.007 \pm 0.118$
0.375	$1.072 \pm 0.005 \pm 0.096$	$1.059 \pm 0.005 \pm 0.095$
0.425	$0.841 \pm 0.004 \pm 0.075$	$0.815 \pm 0.004 \pm 0.073$
0.475	$0.650 \pm 0.004 \pm 0.058$	$0.626 \pm 0.004 \pm 0.056$
0.525	$0.483 \pm 0.003 \pm 0.043$	$0.486 \pm 0.003 \pm 0.043$
0.575	$0.366 \pm 0.002 \pm 0.032$	$0.365 \pm 0.002 \pm 0.032$
0.625	$0.274 \pm 0.002 \pm 0.024$	$0.274 \pm 0.002 \pm 0.024$
0.675	$0.211 \pm 0.001 \pm 0.019$	$0.207 \pm 0.003 \pm 0.018$
0.725	$0.161 \pm 0.001 \pm 0.014$	$0.152 \pm 0.002 \pm 0.013$
0.775	$0.126 \pm 0.003 \pm 0.011$	$0.125 \pm 0.003 \pm 0.011$
0.825	$0.098 \pm 0.004 \pm 0.008$	$0.092 \pm 0.004 \pm 0.008$

Table D.1: *Invariant yields of π^\pm at mid-rapidity ($|y| < 0.1$) in $p + p$ collisions at $\sqrt{s} = 62.4$ GeV. The errors given are both statistical and systematic.*

$p_T(\text{GeV}/c)$	K^+	K^-
0.275	$0.139 \pm 0.004 \pm 0.012$	$0.120 \pm 0.003 \pm 0.010$
0.325	$0.121 \pm 0.003 \pm 0.010$	$0.106 \pm 0.002 \pm 0.009$
0.375	$0.109 \pm 0.002 \pm 0.009$	$0.097 \pm 0.002 \pm 0.008$
0.425	$0.092 \pm 0.002 \pm 0.008$	$0.080 \pm 0.002 \pm 0.007$
0.475	$0.079 \pm 0.003 \pm 0.007$	$0.071 \pm 0.003 \pm 0.006$
0.525	$0.069 \pm 0.003 \pm 0.006$	$0.059 \pm 0.003 \pm 0.005$
0.575	$0.059 \pm 0.003 \pm 0.005$	$0.050 \pm 0.003 \pm 0.004$
0.625	$0.050 \pm 0.003 \pm 0.004$	$0.042 \pm 0.003 \pm 0.003$
0.675	$0.041 \pm 0.002 \pm 0.003$	$0.036 \pm 0.001 \pm 0.003$
0.725	$0.033 \pm 0.002 \pm 0.003$	$0.029 \pm 0.002 \pm 0.002$
0.775	$0.027 \pm 0.003 \pm 0.002$	$0.022 \pm 0.003 \pm 0.002$

Table D.2: *Invariant yields of K^\pm at mid-rapidity ($|y| < 0.1$) in $p + p$ collisions at $\sqrt{s} = 62.4$ GeV. The errors given are both statistical and systematic.*

$p_T(\text{GeV}/c)$	p	\bar{p}
0.425	$0.061 \pm 0.0011 \pm 0.0054$	$0.043 \pm 0.0012 \pm 0.0039$
0.475	$0.050 \pm 0.0010 \pm 0.0045$	$0.040 \pm 0.0010 \pm 0.0036$
0.525	$0.044 \pm 0.0009 \pm 0.0040$	$0.037 \pm 0.0010 \pm 0.0033$
0.575	$0.041 \pm 0.0008 \pm 0.0037$	$0.032 \pm 0.0008 \pm 0.0028$
0.625	$0.037 \pm 0.0007 \pm 0.0033$	$0.028 \pm 0.0008 \pm 0.0026$
0.675	$0.033 \pm 0.0007 \pm 0.0029$	$0.024 \pm 0.0007 \pm 0.0021$
0.725	$0.028 \pm 0.0006 \pm 0.0025$	$0.021 \pm 0.0006 \pm 0.0019$
0.775	$0.024 \pm 0.0006 \pm 0.0022$	$0.017 \pm 0.0005 \pm 0.0015$
0.825	$0.022 \pm 0.0005 \pm 0.0019$	$0.014 \pm 0.0005 \pm 0.0012$
0.875	$0.019 \pm 0.0005 \pm 0.0017$	$0.011 \pm 0.0004 \pm 0.0010$
0.925	$0.015 \pm 0.0004 \pm 0.0013$	$0.009 \pm 0.0004 \pm 0.0008$
0.975	$0.012 \pm 0.0004 \pm 0.0011$	$0.008 \pm 0.0003 \pm 0.0007$
1.025	$0.010 \pm 0.0004 \pm 0.0009$	$0.007 \pm 0.0003 \pm 0.0006$
1.075	$0.008 \pm 0.0003 \pm 0.0008$	$0.005 \pm 0.0003 \pm 0.0004$

Table D.3: *Invariant yields of p and \bar{p} at mid-rapidity ($|y| < 0.1$) in $p+p$ collisions at $\sqrt{s} = 62.4$ GeV. The errors given are both statistical and systematic.*

$p_T(\text{GeV}/c)$	π^-/π^+
0.225	$0.940 \pm 0.0093 \pm 0.1197$
0.275	$0.983 \pm 0.0073 \pm 0.1251$
0.325	$0.992 \pm 0.0074 \pm 0.1263$
0.375	$0.987 \pm 0.0077 \pm 0.1257$
0.425	$0.969 \pm 0.0081 \pm 0.1234$
0.475	$0.962 \pm 0.0087 \pm 0.1225$
0.525	$1.006 \pm 0.0100 \pm 0.1280$
0.575	$0.998 \pm 0.0110 \pm 0.1271$
0.625	$1.000 \pm 0.0139 \pm 0.1272$
0.675	$0.978 \pm 0.0202 \pm 0.1245$
0.725	$0.940 \pm 0.0204 \pm 0.1197$
0.775	$0.989 \pm 0.0380 \pm 0.1259$
0.825	$0.933 \pm 0.0574 \pm 0.1187$

Table D.4: *Antiparticle to particle ratio of π^-/π^+ at mid-rapidity ($|y| < 0.1$) in $p+p$ collisions at $\sqrt{s} = 62.4$ GeV. The errors given are both statistical and systematic.*

$p_T(\text{GeV}/c)$	K^-/K^+
0.275	$0.860 \pm 0.037 \pm 0.1095$
0.325	$0.879 \pm 0.033 \pm 0.1119$
0.375	$0.897 \pm 0.031 \pm 0.1142$
0.425	$0.868 \pm 0.031 \pm 0.1105$
0.475	$0.904 \pm 0.060 \pm 0.1151$
0.525	$0.857 \pm 0.061 \pm 0.1091$
0.575	$0.856 \pm 0.078 \pm 0.1089$
0.625	$0.849 \pm 0.090 \pm 0.1081$
0.675	$0.873 \pm 0.064 \pm 0.1111$
0.725	$0.890 \pm 0.087 \pm 0.1133$
0.775	$0.821 \pm 0.175 \pm 0.1045$

Table D.5: Antiparticle to particle ratio of K^-/K^+ at mid-rapidity ($|y| < 0.1$) in $p+p$ collisions at $\sqrt{s} = 62.4$ GeV. The errors given are both statistical and systematic.

$p_T(\text{GeV}/c)$	\bar{p}/p
0.425	$0.712 \pm 0.024 \pm 0.0907$
0.475	$0.803 \pm 0.027 \pm 0.1023$
0.525	$0.826 \pm 0.028 \pm 0.1052$
0.575	$0.775 \pm 0.026 \pm 0.0987$
0.625	$0.774 \pm 0.027 \pm 0.0985$
0.675	$0.730 \pm 0.027 \pm 0.0929$
0.725	$0.734 \pm 0.028 \pm 0.0934$
0.775	$0.698 \pm 0.028 \pm 0.0888$
0.825	$0.645 \pm 0.028 \pm 0.0821$
0.875	$0.628 \pm 0.030 \pm 0.0799$
0.925	$0.636 \pm 0.033 \pm 0.0810$
0.975	$0.644 \pm 0.035 \pm 0.0820$
1.025	$0.662 \pm 0.041 \pm 0.0843$
1.075	$0.595 \pm 0.049 \pm 0.0757$

Table D.6: Antiparticle to particle ratio of \bar{p}/p at mid-rapidity ($|y| < 0.1$) in $p + p$ collisions at $\sqrt{s} = 62.4$ GeV. The errors given are both statistical and systematic.

$p_T(\text{GeV}/c)$	K^+/π^+
0.275	$0.086 \pm 0.0026 \pm 0.0109$
0.325	$0.091 \pm 0.0024 \pm 0.0115$
0.375	$0.101 \pm 0.0024 \pm 0.0129$
0.425	$0.110 \pm 0.0027 \pm 0.0140$
0.475	$0.122 \pm 0.0061 \pm 0.0155$
0.525	$0.143 \pm 0.0070 \pm 0.0182$
0.575	$0.161 \pm 0.0186 \pm 0.0205$
0.625	$0.184 \pm 0.0130 \pm 0.0234$
0.675	$0.196 \pm 0.0120 \pm 0.0250$
0.725	$0.206 \pm 0.0149 \pm 0.0263$
0.775	$0.217 \pm 0.0311 \pm 0.0276$

Table D.7: *Unlike particle ratio of K^+/π^+ at mid-rapidity ($|y| < 0.1$) in $p + p$ collisions at $\sqrt{s} = 62.4$ GeV. The errors given are both statistical and systematic.*

$p_T(\text{GeV}/c)$	K^-/π^-
0.275	$0.0753 \pm 0.0024 \pm 0.0095$
0.325	$0.0806 \pm 0.0022 \pm 0.0102$
0.375	$0.0924 \pm 0.0023 \pm 0.0117$
0.425	$0.0984 \pm 0.0026 \pm 0.0125$
0.475	$0.1146 \pm 0.0050 \pm 0.0145$
0.525	$0.1218 \pm 0.0064 \pm 0.0155$
0.575	$0.1386 \pm 0.0104 \pm 0.0176$
0.625	$0.1564 \pm 0.0126 \pm 0.0199$
0.675	$0.1758 \pm 0.0080 \pm 0.0223$
0.725	$0.1957 \pm 0.0136 \pm 0.0249$
0.775	$0.1802 \pm 0.0293 \pm 0.0229$

Table D.8: *Unlike particle ratio of K^-/π^- at mid-rapidity ($|y| < 0.1$) in $p + p$ collisions at $\sqrt{s} = 62.4$ GeV. The errors given are both statistical and systematic.*

$p_T(\text{GeV}/c)$	p/π^+
0.425	$0.0725 \pm 0.0014 \pm 0.0092$
0.475	$0.0771 \pm 0.0016 \pm 0.0098$
0.525	$0.0929 \pm 0.0020 \pm 0.0118$
0.575	$0.1129 \pm 0.0025 \pm 0.0143$
0.625	$0.1360 \pm 0.0031 \pm 0.0173$
0.675	$0.1562 \pm 0.0037 \pm 0.0198$
0.725	$0.1780 \pm 0.0046 \pm 0.0226$
0.775	$0.1954 \pm 0.0070 \pm 0.0248$
0.825	$0.2230 \pm 0.0111 \pm 0.0283$

Table D.9: *Unlike particle ratio of p/π^+ at mid-rapidity ($|y| < 0.1$) in $p + p$ collisions at $\sqrt{s} = 62.4$ GeV. The errors given are both statistical and systematic.*

$p_T(\text{GeV}/c)$	\bar{p}/π^-
0.425	$0.0533 \pm 0.0015 \pm 0.0067$
0.475	$0.0643 \pm 0.0017 \pm 0.0081$
0.525	$0.0763 \pm 0.0021 \pm 0.0097$
0.575	$0.0877 \pm 0.0025 \pm 0.0111$
0.625	$0.1052 \pm 0.0031 \pm 0.0134$
0.675	$0.1162 \pm 0.0040 \pm 0.0148$
0.725	$0.1390 \pm 0.0049 \pm 0.0176$
0.775	$0.1378 \pm 0.0059 \pm 0.0175$
0.825	$0.1543 \pm 0.0088 \pm 0.0196$

Table D.10: *Unlike particle ratio of p/π^- at mid-rapidity ($|y| < 0.1$) in $p + p$ collisions at $\sqrt{s} = 62.4$ GeV. The errors given are both statistical and systematic.*

<i>Hadron</i>	dN/dy	$\langle p_T \rangle$
π^+	1.874 ± 0.285	0.393 ± 0.017
π^-	1.832 ± 0.277	0.390 ± 0.021
K^+	0.166 ± 0.035	0.576 ± 0.050
K^-	0.145 ± 0.028	0.575 ± 0.037
p	0.117 ± 0.026	0.696 ± 0.038
\bar{p}	0.088 ± 0.018	0.638 ± 0.035

Table D.11: *Particle yield per unit rapidity (dN/dy) and average transverse momentum ($\langle p_T \rangle$) for π^\pm , K^\pm , p and \bar{p} at mid-rapidity ($|y| < 0.1$) in $p + p$ collisions at $\sqrt{s} = 62.4$ GeV. The errors given are both statistical and systematic added in quadrature.*

Bibliography

- [1] S. S. M. Wong, “Introductory Nuclear Physics”, Second Edition, Wiley-VCH (2004).
- [2] CERN web page <http://home.web.cern.ch/about/physics/standard-model>.
- [3] D. J. Griffiths, “Introduction To Elementary Particles”, ISBN 0-471-60386-4 (1987).
- [4] A. Das and T. Ferbel, “Introduction to Nuclear and Particle Physics”, World Scientific Publishing (2005).
- [5] N. Ishii, S. Aoki, and T. Hatsuda, “The nuclear force from lattice QCD”, arXiv.org (2006).
- [6] G. S. Bali, “QCD forces and heavy quark bound states”, Phys. Rept. **343**, 1-36 (2001).
- [7] B. R. Martin, G. Shaw, “Particle Physics”, Third Edition (2008).
- [8] E. V. Shuryak, “Quantum Chromodynamics and the theory of superdense matter”, Phys. Rept. **61**, 71 (1980).
- [9] From the National Academies Press, National Academy of Sciences, (1999).
- [10] J. Adams et al., Nucl. Phys. A **757**, 102-183 (2005).

- [11] J. M. Lattimer and M. Prakash, “Neutron Star Observations: Prognosis for Equation of State Constraints”, Phys. Rept. **442**, 109 (2007).
- [12] M. G. Alford et al., “Color superconductivity in dense quark matter”, Rev. Mod. Phys. **80**, 1455 (2008).
- [13] M. A. Stephanov, “QCD phase diagram and the critical point”, Prog. Theor. Phys. Suppl. **153**, 139 (2004).
- [14] R. J. Glauber and G. Mathiae, “High-energy scattering of protons by nuclei”, Nucl. Phys. B **21**, 135 (1970).
- [15] H. Satz, Rep. Prog. Phys. **63**, 1511-1574 (2000).
- [16] C. Y. Wong, “Introduction to High-Energy Heavy-Ion Collisions”, World Scientific, Singapore (1994).
- [17] F. M. Liu, K. Werner, Phys. Rev. Lett. **106**, 242301 (2011).
- [18] J. F. Grobe-Oetringhaus, “Measurement of the Charged-Particle Multiplicity in Proton-Proton Collisions with the ALICE detector”, Ph.D thesis, University of Münster (2009).
- [19] M. Deile, “Open issue in diffractive physics: What answers do we expect from the LHC?”, Talk at ‘Physics at the LHC’, 2nd Oct (2008).
- [20] J. R. Forshaw, D. A. Ross, “Quantum Chromodynamics and Pomeron”, CUP p17 (1997).
- [21] P. D. Collins, “An Introduction to Regge Theory and High Energy Physics”, CUP (1977).
- [22] V. Barone, E. Predazzi, “High-Energy Particle Diffraction”, Springer-Verlag Berlin Heidelberg, New York, **47**, 1-6 (2002).

- [23] S. Albino, Rev. Mod. Phys. **82**, 2489-2556, (2010).
- [24] N. Metropolis, “The Begining of the Monte Carlo Method”, Los Alamos Science, Special Issue (1987).
- [25] J. H. Halton, SIAM Rev. **12**, 1-63 (1970).
- [26] B. Anderson et al., Phys. Rept. **97**, 31 (1983).
- [27] P. Eden, G. Gustafson, Z. Phys. C **75** (1997).
- [28] J. Guillaud, A. Sobol, “Simulation of diffractive and non-diffractive processes at the LHC energy with the PYTHIA and PHOJET MC event generators”, IAPP-EXP (2004).
- [29] Webpage link: <http://home.thep.lu.se/~torbjorn/Pythia.html>, PYTHIA Manual, sec. 11.5.
- [30] A. Capella, U. Sukhatme et al., Phys. Rept. **236**, 225-329 (1994).
- [31] F. Becattini and U. Heinz, Z. Phys. C **76**, 269-286 (1997).
- [32] R. Hagedorn and J. Ranft, Nuovo Cim, Suppl. **6**, 169 (1968).
- [33] C. Tsallis, J. Stat. Phys. **52**, 479 (1988).
- [34] R. Campanini and G. Ferri, Phys. Lett. B **703**, 237-245 (2011).
- [35] F. Cooper and G. Frye, Phys. Rev. D **10**, 186 (1974).
- [36] Z. Tang et al., Phys. Rev. C **79**, 051901 (2009).
- [37] G. E. Brown and M. Rho, Phys. Rev. Lett. **66**, 2720 (1991).
- [38] M. kaku, “Quantum Field Theory, A Modern Introduction”, Oxford University Press, New York (1993).

- [39] W. Yang, “Baryogenesis and Asymmetric Dark Matter from the the Left-Right Mirror Symmetric Model”, arXiv:1405.0389 (2014).
- [40] N. M. Borstnik, “Can the matter-antimatter asymmetry be easier to understand within the spin charge family theory”, arXiv:1011.5764 (2010).
- [41] E. Schnedermann and U. W. Heinz, Phys. Rev. C **50** 1675 (1994).
- [42] S. Jeon and V. Koch, Phys. Rev. Lett. **83**, 5435 (1999).
- [43] M. Stephanov, K. Rajagopal and E. Shuryak, Phys. Rev. D **60**, 114028 (1999).
- [44] Q. H. Zhang, S. Jeon, V. Topor and C. Gale, Phys. Rev. C **66**, 014909 (2002).
- [45] K. Geiger et al., Phys. Rev. D **46**, 4986 (1992).
- [46] J. Letessier and J. Rafelski, “Hadrons and Quark-Gluon Plasma”, Cambridge University Press (2004).
- [47] U. Heinz, P. R. Subramaniam and W. Griener, Z. Phys. A **318**, 247 (1984).
- [48] J. Ellis, U. Heinz and H. Kowalski, Phys. Lett. B **233**, 223 (1989).
- [49] S. Gavin, M. Gyulassy, M. Plummer and R. Venugopalan, Phys. Lett. B **234**, 175 (1990).
- [50] A. Capella et al., Phys. Rep. **236**, 225 (1994).
- [51] K. Aamodt et al., Eur. Phys. J. **C71**, 1655 (2011).
- [52] B. Mohanty et al., Phys. Lett. B **655**, 104-113 (2007).
- [53] D. d’Enterria, J. Phys. G **31**, S491 (2005).
- [54] J. Rafelski and B. Muller, Phys. Rev. Lett. **48** 1066 (1982).

- [55] B. I. Abelev et al., Phys. Rev. C **79**, 034909 (2009).
- [56] T. Ludlam “Overview of experiments and detectors at RHIC”, Nucl. Instrum. and Meth. A **499**, 428-432 (2003).
- [57] M. Harrison, T. Lundlam, and S. Ozaki “RHIC project overview”, Nucl. Instrum. and Meth. A **499**, 235-244 (2003).
- [58] Webpage link RHIC: <http://www.agsrhichome.bnl.gov/RHIC/Runs/>.
- [59] J. Ashman et al., Phys. Lett. B **206**, 364 (1988).
- [60] K. H. Ackermann et al., “STAR detector overview” Nucl. Instrum. Meth. A **499**, 624-632 (2003).
- [61] A. Schmah and Maria, 3D picture of the STAR detector, (2014).
- [62] C. A. Whitten Jr et al., AIP Conf. Proc. **980**, 390 (2008).
- [63] L. Adamczyk et al., Phys. Rev. C **86**, 054908 (2012).
- [64] W. R. Leo, “Techniques for Nuclear and Particle Physics Experiments”, Springer Verlag, P. No. 26 (1994).
- [65] G. V. Buren et al., “Correcting for distortions due to ionization in the STAR TPC”, Nucl. Instrum. and Meth. A **566**, 22-25 (2006).
- [66] J. Abele et al., “The laser system for the STAR time projection chamber”, Nucl. Instrum. and Meth. A **499**, 692-702 (2003).
- [67] H. Wieman et al., IEEE Trans. Nucl. Sci. **44**, 671 (1997).
- [68] M. Anderson et al., Nucl. Instrum. and Meth. A **499**, 659 (2003).
- [69] S. Klein et al., IEEE Trans. Nucl. Sci. **43**, 1768 (1996).

- [70] W. Blum and L. Rolandi, “Particle Detection with Drift Chambers”, Springer Verlag, (1993).
- [71] H. Bichsel, “Comparison of Bethe-Bloch and Bichsel Functions”, STAR Note 439.
- [72] E. V. Shuryak, Phys. Lett. B **78**, 150 (1978).
- [73] J. D. Bjorken, Phys. Rev. D **27**, 140 (1983).
- [74] E. C. Zeballos et al., “A new type of resistive plate chamber: The multigap RPC”, Nucl. and Meth. A **374**, 132-135 (1996).
- [75] W. Llope, “The large-area time-of-flight upgrade for STAR”, Nucl. Instrum. and Meth. B **241**, 306 (2005).
- [76] M. Shao et al., Nucl. Instrum. and Meth. A **558**, 419 (2006).
- [77] S. Margetis, Conference Proceeding: ICNFP, Crete, Greece (2014).
- [78] M. Beddo et al., Nucl. Instrum. and Meth. A **499**, 725 (2003).
- [79] J. M. Landgraf et al., Nucl. Instrum. and Meth. A **499**, 762 (2003).
- [80] M. Beddo et al., Nucl. Instrum. and Meth. A **499**, 740 (2003).
- [81] STAR Collaboration, Technical Design Report, <http://drupal.star.bnl.gov/STAR/starnotes/public/sn0600>.
- [82] M. A. Lisa et al., “The STAR TPC Cluster Finder/Hit Finder” - STAR Note, SNO238, (1996).
- [83] R. Bossingham et al., “STAR Offline Simulations and Analysis Software Design” - STAR Note, SNO281, (1997).

- [84] C. Adler et al., “The STAR Level-3 Trigger”, Doktorarbeit, Institut für Kernphysik der Johann-Wolfgang-Goethe Universität, Frankfurt am Main (2002).
- [85] W. Blum and L. Rolandi, “Particle Detection with Drift Chambers”, Springer Verlag, (1993).
- [86] J. E. Gans, Ph.D. Thesis “Inclusive Charged Hadron Transverse Momentum Spectra at Center of Mass Energy of 200 GeV for $p + p$ and $d + Au$ Collisions at the Relativistic Heavy Ion Collider”, Yale University (2004).
- [87] W. M. Yao et al., J. Phys. G **33**, 1 (2006).
- [88] H. Bichsel, Nucl. Instrum. and Meth. A **562**, 154 (2006).
- [89] B. I. Abelev et al., Phys. Rev. C **79**, 34909 (2009).
- [90] M. Calderon de la Barca Sanchez, Ph.D. thesis, Yale University (2001).
- [91] J. Adams et al., Phys. Rev. Lett. **91**, 172302 (2003).
- [92] D. Ashery and J. P. Schiffer, Annu. Rev. Nucl. Part. Sci. **36**, 207 (1986).
- [93] J. T. Mitchell and I. M. Sakrezda, Tracking for the STAR TPC: STAR Note, SNO190, (1994).
- [94] D. Cebra and S. Margetis, Main Vertex Reconstruction the STAR: STAR Note, SNO089, (1992).
- [95] T. Sjostrand, S. Mrenna, and P. Z. Skands, JHEP **5**, 026959 (2006).
- [96] B. Anderson, The Lund Model, Cambridge University Press (2005).
- [97] E. Schnedermann and U. W. Heinz, Phys. Rev. C **50**, 1675 (1994).
- [98] A. Adare et al., Phys. Rev. C **83**, 064903 (2011).

- [99] J. Adams et al., Phys. Rev. Lett. **92**, 112301 (2004).
- [100] R. Brun and F. Rademacher, “ROOT: An object oriented data analysis framework”, Nucl. Instrum. Meth. A **389**, 81 (1997).
- [101] A. Leonidov, M. Nardi and H. Satz, Z. Phys. C **74**, 535 (1997).
- [102] N. Xu and M. Kaneta, Nucl. Phys. A **698**, 306 (2002).
- [103] E. Schnedermann et al., Phys. Rev. C **48**, 2462 (1993).
- [104] B. Andersson et al., Z. Phys. C **20**, 317 (1983).